

1. The first step in the process is to identify the problem or issue that needs to be addressed. This involves gathering information and understanding the context of the problem.

2. Once the problem is identified, the next step is to define the objectives and goals of the project. This helps to clarify what needs to be achieved and provides a clear direction for the team.

3. The third step is to develop a plan or strategy to address the problem. This involves breaking down the problem into smaller, manageable tasks and determining the resources needed to complete each task.

4. The fourth step is to implement the plan. This involves putting the strategy into action and monitoring progress to ensure that the project is on track.

5. The final step is to evaluate the results of the project. This involves assessing the outcomes against the objectives and goals and identifying any areas for improvement.

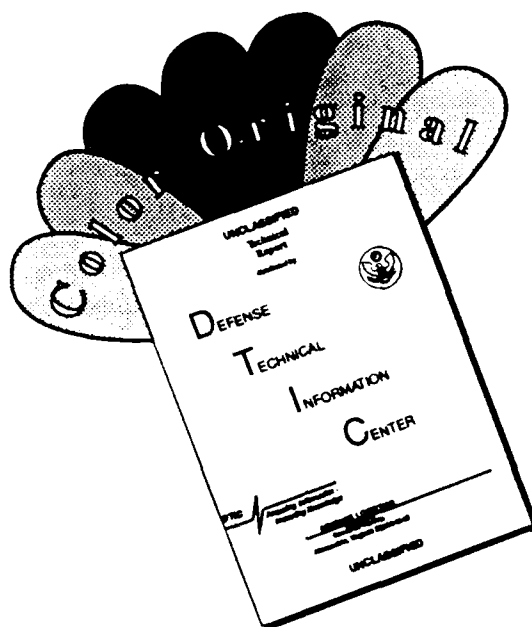
Form Approved  
CASE NO. 9704-0182

Send to: **Director, FBI**, Washington, D.C. 20535. For information only, send to: **Director, FBI**, Washington, D.C. 20535. For information only, send to: **Director, FBI**, Washington, D.C. 20535.

45N 7540-01-280-5500

Standard Form 298 (Rev. 2-89)  
Prescribed by ANSI Std. Z39-18

# DISCLAIMER NOTICE



THIS DOCUMENT IS BEST QUALITY AVAILABLE. THE COPY FURNISHED TO DTIC CONTAINED A SIGNIFICANT NUMBER OF COLOR PAGES WHICH DO NOT REPRODUCE LEGIBLY ON BLACK AND WHITE MICROFICHE.

Research Progress and Forecast Report

**REAL-TIME ADAPTIVE CONTROL OF  
MIXING IN A PLANE SHEAR LAYER**

Grant No. AFOSR-89-0465

Submitted to  
Air Force Office of Scientific Research  
Bolling Air Force Base, Building 410  
Washington, D.C. 20332

Submitted by  
A. Glezer  
Department of Aerospace and Mechanical Engineering  
University of Arizona  
Tucson, Arizona 85721

Accession For	
NTIS CRA&I	<input checked="" type="checkbox"/>
DTIC TAB	<input type="checkbox"/>
Unannounced	<input type="checkbox"/>
Justification	
By	
Distribution /	
Availability Code	
Dist	Avail and/or Special
A-1	

**92-05643**



**92 3 03 129**

## TABLE OF CONTENTS

INTRODUCTION.....	1
Part I	
REAL-TIME FEEDBACK CONTROL OF MIXING IN A PLANE	
SHEAR LAYER.....	2
I.1. Introduction.....	2
I.2. The experimental apparatus.....	5
I.2.1 The water shear layer facility.....	5
I.2.2 Instrumentation.....	9
I.2.3 Control system hardware.....	9
I.3. The control system.....	11
I.4. Closed-loop results.....	14
I.4.1 The feedback gains.....	14
I.4.2 Controller effect in the frequency domain.....	14
I.4.3 Mixing in the unforced shear layer.....	18
I.4.4 Mixing with feedback.....	22
I.4.5 Variation of mixing with downstream distance.....	27
I.4.6 Effect of small scale motions.....	29
I.4.7 Time-invariant spanwise-periodic excitation with feedback.....	31
I.4.8 Detailed comparison of feedback configurations C3D <sub>3</sub> and C <sub>3</sub> .....	35
I.5. Open-loop results.....	40
I.5.1 Instantaneous and time-averaged data.....	40
I.5.2 Phase averaged mixing.....	46
I.6 Variation of <b>PM</b> with $k$ .....	49
I.7. Summary and outline of future research.....	53
Part II	
MANIPULATION OF FREE SHEAR FLOWS USING PIEZOELECTRIC	
ACTUATORS.....	55
II.1. Introduction.....	55
II.2. Experimental apparatus and procedure.....	56
II.2.1. The air jet facility.....	56
II.2.2. Experimental conditions.....	58
II.2.3. Piezoelectric Actuators.....	60
II.3. Amplitude-modulated excitation.....	63
II.4. Modification of the square jet.....	68
II.4.1. Distortion of the mean flow.....	68
II.4.2. Phase-averaged flow structure.....	72
II.5. Summary and outline of future research.....	79
References.....	81

## INTRODUCTION

The study of the mechanisms which lead to mixing in shear flows is *crucial* to technological applications in combustion processes. These processes involve chemical reaction between two or more species within a free turbulent shear flow, and depend on mixing of the flow streams. Thus, the development of methods for enhancement and control of mixing through manipulation of the flow will have a direct impact on the performance of propulsion systems from the standpoint of efficient combustion and controllable thrust. Previous investigations have demonstrated that mixing can be effectively manipulated by excitation of flow instabilities through the introduction of controlled disturbances at the flow boundary. The flow is typically extremely receptive to excitation within a limited frequency band and, as a result, the controlled disturbances are rapidly amplified. This means that a large effect on mixing can be achieved with relatively small power input. For combustion processes such excitation may influence the overall reaction rate, as well as the spatial and temporal distribution of heat release and reaction products.

The primary objective of the title research program has been the development of a real-time feedback control system of a thermal analog of mixing in a nonreactive plane shear layer between two streams maintained at different constant temperatures. The temperature distribution is a thermal analog to the concentration measurements normally performed in conventional blow-down chemically reacting shear layer facilities. The study of mixing in water by exploiting temperature as a passive scalar is of particular interest because the relevant diffusion parameter, the Prandtl number, is approximately 7. Hence, a reasonable comparison can be made with mixing and combustion processes in gases where the relevant diffusion parameter, the Schmidt number, is approximately 1 (the Schmidt number in water is approximately 1000). The actuators and sensors utilized for the control scheme are surface film heaters and cold wire temperature sensors, respectively. This work is described in Part I of the present progress report.

A secondary objective of the title investigation, which is described in Part II of the present progress report, has been the implementation of new piezoelectric actuator technology for flow control *via* micro-manipulation of vorticity. Because mixing in free shear flows is dominated by the dynamics of a hierarchy of vortical structures, it is desirable to utilize actuators having fast dynamic response which can directly modify the vorticity distribution at the flow boundary. Piezoelectric actuators are attractive for mixing and combustion control because of their small dimensions, low power consumption, and their capability to withstand high temperatures and corrosive environments. The utility of these actuators for the modification of free shear flows has been convincingly demonstrated in noncircular air jets which are effectively forced through their upstream shear layers.

## Part I: REAL-TIME FEEDBACK CONTROL OF MIXING IN A PLANE SHEAR LAYER

### I.1. Introduction

The study of the mechanisms leading to mixing transition in plane and axisymmetric mixing layers owes much of its importance to its technological applications in combustion processes. These processes involve chemical reaction between two or more species in a free turbulent shear flow and depend *crucially* on mixing between the streams, which is induced by a hierarchy of large coherent vortical structures. Thus, development of methods for the control of mixing by manipulation of the instability modes which lead to the formation of these vortical structures will have a direct impact on the performance of propulsion systems from the standpoint of efficient combustion and controllable thrust.

In the plane mixing layer, mixing is accomplished by nominally two-dimensional entrainment of irrotational fluid from both streams by the spanwise vortices, and three-dimensional motion induced by packet of streamwise counter-rotating vortex pairs which form in the region of maximum strain between adjacent spanwise vortices (the "braids"). Previous investigations have demonstrated that harmonic spanwise-uniform excitation may significantly enhance or reduce the natural mixing in a plane shear layer and that mixing transition is associated with the appearance of a spanwise instability.

The development of open loop forcing schemes has progressed to the point where the large coherent structures which govern mixing in the plane shear layer can be manipulated with great versatility. In particular, our work on spanwise nonuniform excitation of the plane shear layer (Nygaard and Glezer 1991) under the auspices of AFOSR, has demonstrated the utility of surface film heating actuators mounted on the flow partition for flow manipulation and mixing enhancement. The objective of the present investigation is to build on this capability and develop a real-time feedback control system for optimizing various measures of mixing in a nonreactive plane shear layer.

The present experiments are conducted in a closed return water shear layer facility using a thermal analog to the concentration measurements normally performed in conventional blowdown chemically reacting shear layer facilities. The thermal analog is based on maintaining the two streams at slightly different constant temperatures. The performance measures infer the degree of mixing from the history of the temperature distribution. Because temperature is being mixed, the Prandtl number ( $Pr$ , the ratio of kinematic viscosity to thermal diffusivity) determines the ratio of the smallest velocity scales to the smallest temperature scales. In experiments dealing with the mixing of

chemical species, the corresponding relevant parameter is the Schmidt number ( $Sc$ , the ratio of kinematic viscosity to chemical diffusivity). Mixing at the smallest scales varies considerably depending upon the value of  $Sc$  or  $Pr$ . The Schmidt and Prandtl numbers are typically  $O(1)$  in air; whereas in water,  $Sc = O(1000)$  and  $Pr \approx 7$ . Hence, the present experiments may be more comparable with mixing in air than with mixing of species in water.

The mixing process in plane shear layers consists of three distinct stages (Dimotakis 1989): (a) entrainment into the mixing zone, (b) straining of the entrained fluid particles until their spatial scales are comparable with scales at which the kinetic energy diffusive processes take place, and (c) scalar diffusive processes at the molecular level. The amount of mixed fluid which can be produced at any streamwise station is clearly limited by the transverse (cross-stream) extent of the shear layer  $\delta$ . The composition or volume fraction of fluid from each stream is measured by the volume entrainment ratio  $E_v$ , which is the ratio of high-speed fluid to low-speed fluid entrained into the layer. The volume entrainment ratio is especially important in chemically reacting mixing layers where proper stoichiometry for the reaction is required. Dimotakis (1986, 1989) proposed a model to predict the volume entrainment ratio

$$E_v = s^{1/2} \left( 1 + 0.68 \cdot \frac{1-r}{1+r} \right)$$

where  $s = \rho_2/\rho_1$  is the density ratio, and  $r = U_2/U_1$  is the velocity ratio. Unfortunately, this model does not take into account the effect of external excitation, nor does it predict the total entrainment.

The amount of reaction product in a reacting mixing layer increases by an order of magnitude downstream of the mixing transition (Roshko 1981). In an experimental investigation of mixing transition in a nonreacting shear layer, Koochesfahani and Dimotakis (1986) used laser induced fluorescence to show a substantial increase in the small scale motions within the layer. The appearance of the small-scale flow structures marks an important stage in the mixing process because of the increase in the interfacial area between the entrained fluids where efficient mixing at the molecular level can take place. By examining the probability density function *pdf*( $\xi, y$ ) of species concentration  $\xi$  at a number of cross-stream elevations they found a substantial increase in concentrations of mixed fluid downstream of mixing transition. The peak of *pdf*( $\xi, y$ ) was found to occur at the same  $\xi$  at each  $y$  elevation. The probability of finding mixed fluid increased with downstream distance. Furthermore, the expected value of mixed fluid concentration  $E(\xi)$

$\xi_1 < \xi < \xi_2$ ) was found to migrate towards the low-speed concentration, suggesting that the initial rollup of the vortices entrained an excess of high-speed fluid.

A number of experimental investigations have demonstrated that open loop time harmonic excitation provides can lead to substantial global flow modifications. For example, Oster and Wygnanski (1982) discovered that forcing a two-dimensional turbulent shear layer produces a "frequency-locked" region in which growth is inhibited, the primary vortices are equally spaced, and their passage frequency is equal to the forcing frequency. Roberts and Roshko (1985) reported that in frequency-locked regions downstream of the mixing transition, mixing is reduced or even completely inhibited, however, forced pairing of the primary vortices resulted in substantial mixing enhancement. In a similar study, Koochesfahani and MacKinnon (1991) found that forcing well below the natural frequency could lead to a small increase in mixing which they attributed to an increase in the layer width due to entrainment.

As noted above, entrainment of irrotational fluid into the shear layer and the evolution of small-scale motions necessary for mixing transition are effected by a hierarchy of large coherent vortical structures, and thus depend weakly, if at all, on  $Sc$  and  $Pr$ . However, mixing of temperature and species at the molecular level clearly depends on the values of the  $Pr$  and  $Sc$  numbers, respectively. The smallest scale of motion in a turbulent flow is the Kolmogorov microscale,  $\eta$ ,

$$\eta = (\nu^3/\epsilon)^{1/4}$$

whereas the smallest temperature scale is the temperature microscale  $\eta_\theta$

$$\eta_\theta = (\gamma^3/\epsilon)^{1/4}.$$

(Tennekes and Lumley 1972) where  $\nu$  is the kinematic viscosity,  $\epsilon$  is the energy dissipation rate per unit mass, and  $\gamma$  is the thermal diffusivity. The ratio of these two scales  $\eta/\eta_\theta \sim Pr^{3/4}$  and gives the approximate ratio of the smallest velocity scales to the smallest temperature scales. For mixing of temperature in water where  $Pr = 7$ , the smallest velocity scales are approximately 4.3 times as large as the smallest temperature scales. In contrast, mixing of dye in water (where  $Sc$  may be as high as 2000, and  $\eta/\eta_B \sim Sc^{3/4}$ ), the smallest velocity scales are two orders of magnitude *larger* than the smallest concentration scales. Dahm, Southerland, and Buch (1991) used a three-dimensional imaging technique to study molecular mixing for this case. They found that most of the mixing occurs in thin sheet-



like structures. In addition, relatively small regions of the flow account for a substantial percentage of the mixing, implying that even at the smallest scales, turbulent mixing is not completely homogeneous.

In addition to previous investigations involving manipulation of free and wall bounded shear flows (e.g., Schubauer and Skramstad 1947, Crow and Champagne 1971), there have been a number of previous attempts to control these flows using various forms of feedback. Wehrman investigated the effect of feedback on a cylinder wake (1965, 1967a) and a flat plate boundary layer (1967b). In the boundary layer experiments he utilized successfully an active flexible wall driven by piezoelectric actuators and located immediately downstream of a hot wire sensor to suppress naturally occurring Tollmein-Schlichting (T-S) waves. In a similar experiment, Nosenchuck (1982) used surface-mounted strip heaters and hot film probes for the suppression of T-S waves and reported a significant delay in transition to turbulence.

In the present experiment, the actuators are located *upstream* of the sensors as described in §I.2. Hence, the controller affects states which are not yet measured by the sensors. This is similar to the concept employed by Reisenthel (1988), who studied the effect of pressure feedback on the global instability of an axisymmetric jet. Reisenthel measured velocity fluctuations with a single hot wire sensor placed downstream of the jet nozzle. The hot wire signal was fed back (with various gains and delays) using a loudspeaker placed downstream of the jet exit plane. Hence, in a manner similar to the present experiment the sensor was placed downstream of the actuator. Reisenthel found that the signal of a separate hot wire sensor placed downstream of the nozzle contained a series of spectral peaks (dubbed "eigenfrequencies"). The period associated with each spectral peak was an integer submultiple of a delay time (the loop delay) which included the effect of flow and electronic delays. This eigenfrequency structure can be expected in any feedback system with delays, as will be shown in §I.3 below.

## **I.2. The experimental apparatus**

### *I.2.1 The water shear layer facility*

The facility (figure I.1) and some of the auxiliary equipment used in the present experiments are described in detail in Nygaard and Glezer (1991). Excitation of streamwise and spanwise instability modes is accomplished via an array of surface film heating elements mounted on the flow partition. The array is comprised of four spanwise-uniform elements upstream of a single 32-element spanwise row. Each heating element is

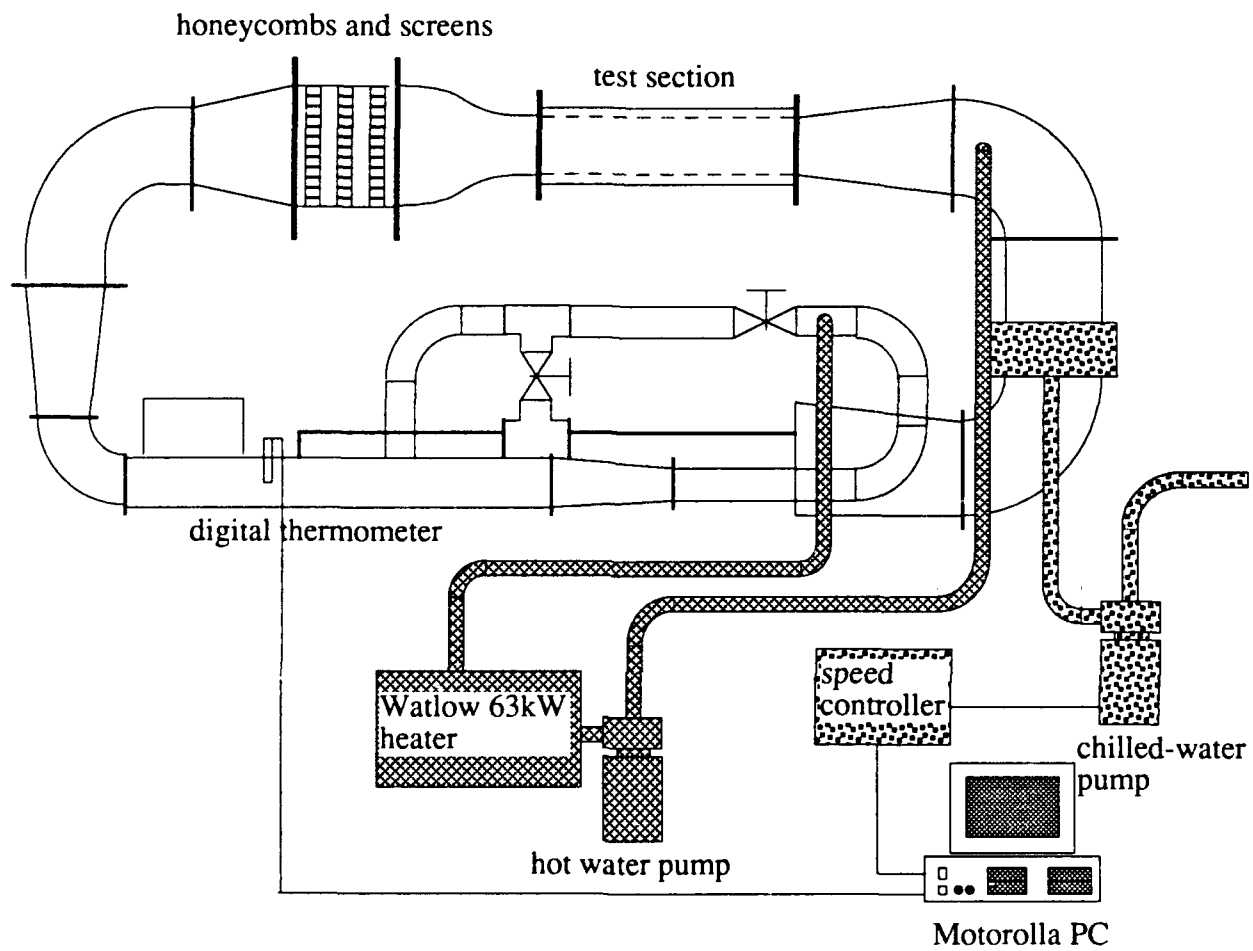


Figure I.1. The two-stream mixing layer facility.

wired to an individual DC power amplifier. The effect of heating the surface is essentially to introduce three-dimensional vorticity perturbations into the flow-partition boundary layer by exploiting the dependence of the viscosity on temperature (Liepmann, Brown, & Nosenchuck 1982).

The facility is substantially modified to provide a constant temperature difference between the two streams. Water from the diffuser downstream of the test section is pumped (at 20 gal/min in the present experiments) through a 63kW circulation heater where the temperature is raised by approximately 10° C. The water is then injected (using multiple jets to promote mixing) into the low-speed stream well upstream of the turbulence management devices. The temperature of each streams at the entrance of the test section is uniform, and the temperature difference is 3° C. A chilled-water heat exchanger (operating at nominally 60 gpm at 8° C in the present experiments) which is built into the facility downstream of the diffuser continuously removes the heat added by the heater. A dedicated PC controls a pump on the chilled water line to maintain the overall temperature of the facility time-invariant to within .05° C. The sensor input to the PC is a platinum thermometer placed in the low-temperature stream. Other platinum thermometers are mounted in various sections of the facility and are continuously scanned using a dedicated digital thermometer.

The closed-loop feedback control scheme used in the present experiments is described in detail in §I.2.3. It is predicated on measurements of the position and velocity of the interface between the two streams (upstream of the first rollup of the primary vortices) as inputs to the controller. To this end, an optical Schlieren system is used to determine the instantaneous position of the interface in the cross-stream direction. As shown in figure I.2, this system differs from conventional Schlieren systems in that all light rays which are not deflected by index of refraction gradients (resulting from temperature gradients) are removed by the knife edge. The large temperature gradient across the interface between the two streams downstream of the flow partition and before the rollup of the primary vortices, appears as a bright spot in the Schlieren image (when the flow field is isothermal the Schlieren image is completely dark). A segment of the interface within this streamwise domain is imaged onto a linear optical position sensor which is aligned in the cross stream direction. The output voltage of the sensor is proportional to the position of the interface and is recorded by the laboratory computer.

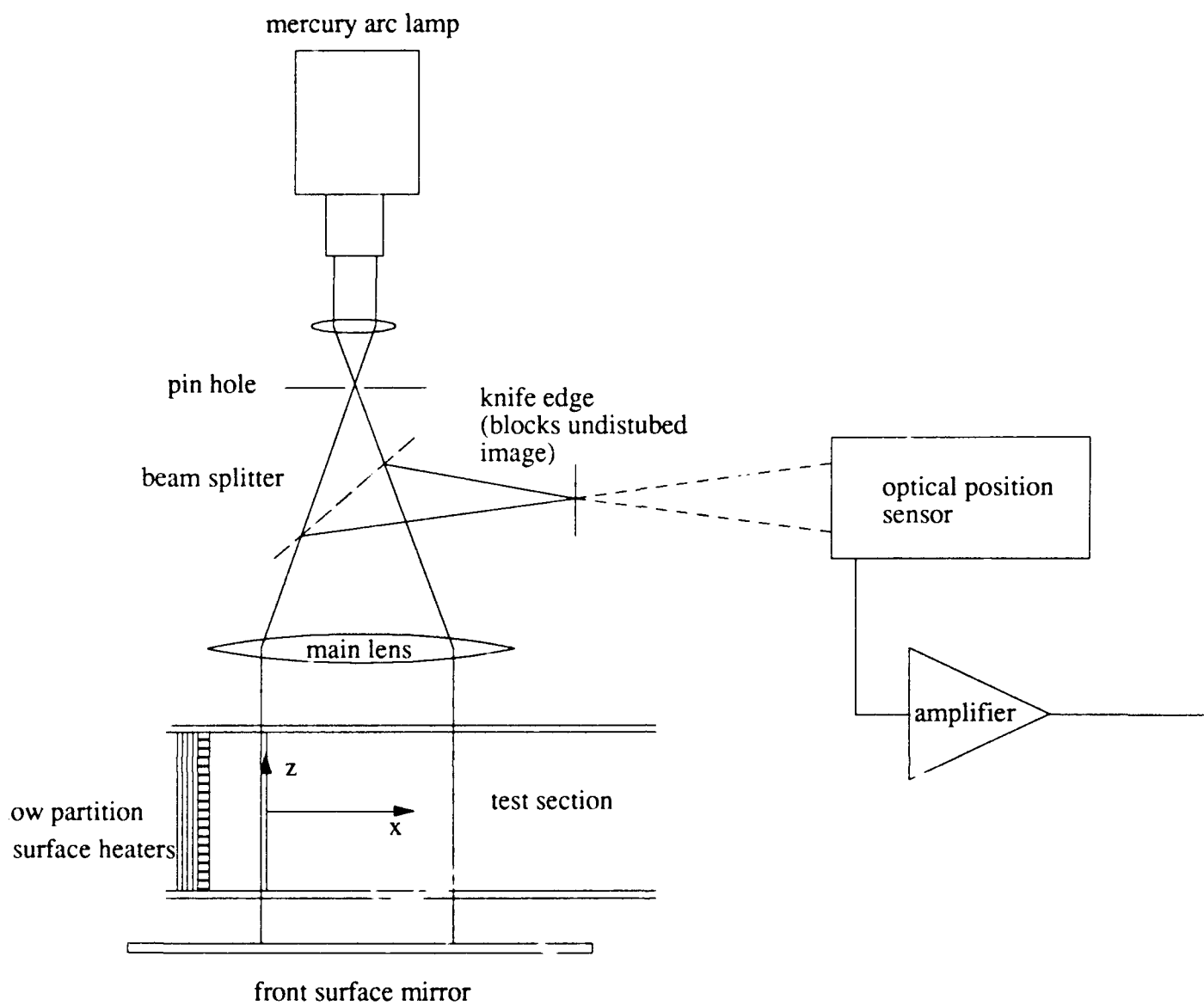


Figure I.2. The cross-stream Schlieren system.

### *1.2.2 Instrumentation*

A Macintosh IIx programmed in MPW C is used for data acquisition and controller implementation. The temperature distribution between the two streams is measured using a rake of 31 cold wire sensors spaced 2 mm apart. A 32 channel cold wire thermometer (CWT) was designed and built for the purposes of the present experiments. Each CWT channel has an rms noise fluctuation of approximately  $.025^{\circ}\text{C}$ , and the overall temperature resolution is  $0.03^{\circ}\text{C}$ . High-speed internal analog switching allows for scanning of all 31 CWT channels at a maximum frequency of 100kHz. The CWT is connected to a single A/D channel at the computer which is capable of a maximum sampling frequency of 1 MHz. A separate slave switching box allows for scanning of up to 32 additional analog channels. This switch is used to sample the interface position and the control input to the surface heaters.

A 36 channel, high speed, 12-bit, Dual-Mode D/A converter (DAC) was designed and built for the present experiments. The DAC can be operated in an update mode for control applications, and in a signal generator mode for open-loop excitation. In both modes, the DAC is accessed via a parallel interface port. In the update mode, any channel can be randomly addressed and updated at a rate of  $2\text{ }\mu\text{s}$  (limited by the present computer). In the signal generator mode, an arbitrary time-periodic waveform can be independently programmed into each of the channels. Each channel contains a 1024 12-bit word dynamic RAM which is loaded from the laboratory computer. Each 12 bit word can be loaded to the output of the respective channel at a maximum rate of 8 MHz. It is important to note that in this mode all frequencies of the DAC channels can be independently programmed.

### *1.2.3 Control system hardware*

The complete control system is shown in figure I.3. The output of the system is the interface position  $y(t)$  which is sampled by the laboratory computer along with the instantaneous temperatures  $T(y,t)$  measured at given streamwise and spanwise positions. As described in §I.2.1, the actuators are an array of surface film heaters flush mounted on the high speed side of the flow partition and driven by DC power amplifiers. The control input  $u(t)$  is proportional to  $y(t-\Delta)$  and  $\dot{y}(t-\Delta)$  where  $\Delta$  is a time delay which is added in software. The reason for the delay is discussed in §I.3. The present controller is characterized by three parameters:  $k_1$  and  $k_2$  (the gains for  $y(t-\Delta)$  and  $\dot{y}(t-\Delta)$ , respectively), and the delay time  $\Delta$ .

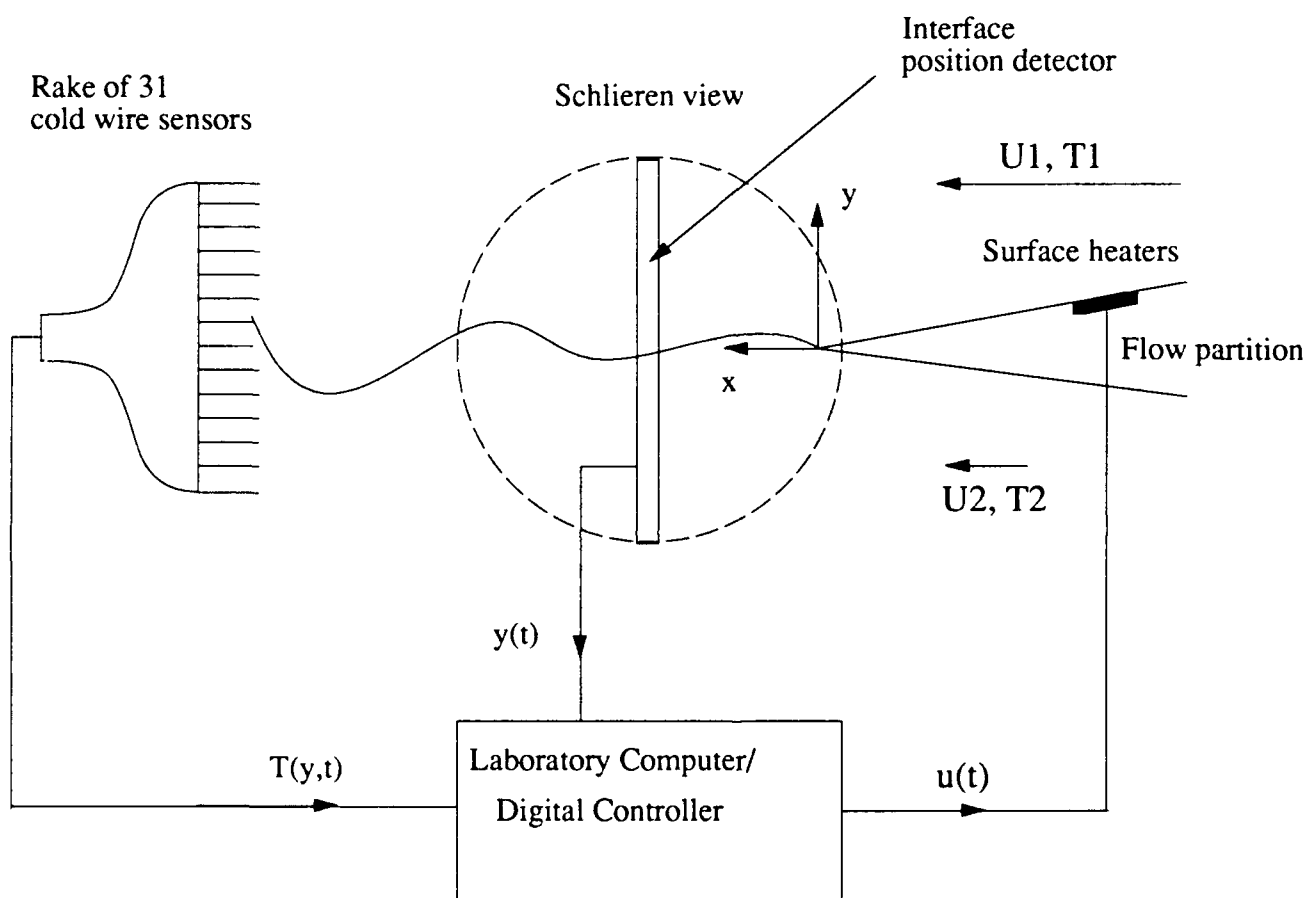


Figure I.3. The control system hardware.

### I.3. The control system

A linear feedback control system which is based on a simple model of the interface cross-stream position  $y(t)$  and its time derivative  $\dot{y}(t)$  has been developed. This model applies in the streamwise domain immediately downstream of the flow partition and before the rolls up of the primary vortices (in the experiments reported here at  $x = 3.81$  cm). Within this streamwise domain,  $y(t)$  is approximately time-harmonic which suggests modelling the interface motion as a second order system described by the second order oscillator equation

$$\ddot{y} + \omega_N^2 y = Cu$$

where  $\omega_N$  is the natural frequency and  $C$  is a constant. This equation can be written in dimensionless form

$$\ddot{Y} + Y = CU$$

where  $Y = y/y_r$ ,  $U = u/(\omega_N^2 y_r)$ ,  $y_r$  is the rms displacement of the interface, and the dimensionless time is  $\tau = \omega_N t$ . Defining the state variables  $x_1 = Y$  and  $x_2 = \dot{Y}$ , the following state equations can be written

$$\begin{aligned}\dot{x}_1 &= x_2 \\ \dot{x}_2 &= -x_1 + CU\end{aligned}$$

which allows for the problem to be approached as a pole-placement problem. If the input  $U$  is the negative feedback of the states, it is possible to move the open loop complex poles of the second order system  $\lambda = \pm i$  to

$$\lambda = \frac{-Ck_2 \pm \sqrt{(Ck_2)^2 - 4(1 + Ck_1)}}{2}$$

The constant  $C$  is determined by measuring the effect of open-loop forcing on the interface. The actual model, of course, predicts that when the system is subjected to open-loop forcing at its natural frequency, resonance occurs and the oscillations become infinitely

large. Resonance can be eliminated if  $|CU| \gg |Y|$  (where the input  $U$  is the open-loop forcing signal) and the system equation is reduced to

$$\ddot{Y} = C U.$$

If the harmonic forcing signal is  $U = \sin \tau$ , then  $Y = -C \sin \tau$  and the ratio of the output to the input is given directly by  $Y/U = -C$ .

A nontrivial problem in the implementation of this controller is that the state which is fed back into the controller is actually the state at  $t - \Delta_T$ , where  $\Delta_T$  is the total system delay between the actuators and the sensors.  $\Delta_T = \Delta_N + \Delta$ , where  $\Delta_N$  is the convection delay of a disturbance between the actuators and the sensors, and  $\Delta$  is a delay which is prescribed in software. It is clear that as  $\Delta_T$  increases, the effect of the feedback is diminished. However, to maximize the effectiveness of the model, the value of  $\Delta$  is chosen so that  $\Delta_T$  corresponds to an integer number of cycles of the flow, i.e.

$$\Delta_T = \frac{n}{\omega_N}$$

As a first approach, we choose  $\Delta$  so that  $Y(t)$  and  $Y(t - \Delta_T)$  have the same phase (at the natural frequency of the interface,  $\omega_N$ ).

In what follows, the procedure for calculating the desired  $\Delta$  is outlined. The averaged power spectrum of the interface position  $S_Y(f) = |F(Y(t))|^2$  is measured when the flow is unforced (figure I.4a). The natural frequency is found to be  $f_N = 5.66$  Hz. Next, the flow is forced open-loop at  $f_N$  and both the forcing signal and the interface position are recorded. In a second-order system which is forced at its resonance frequency, the response of the system  $Y$  is  $180^\circ$  out of phase with the forcing  $U$ , as is also the case for the modified system equation shown above. Thus, the desired  $\Delta$  is that which minimizes the correlation of  $Y$  and  $U$  (figure I.4b) and for the present experiments is  $\Delta = 12$  s. Although the present state model is clearly based on ad-hoc observations of the interface motion, the next section shows its usefulness in qualitative predictions of feedback effects.



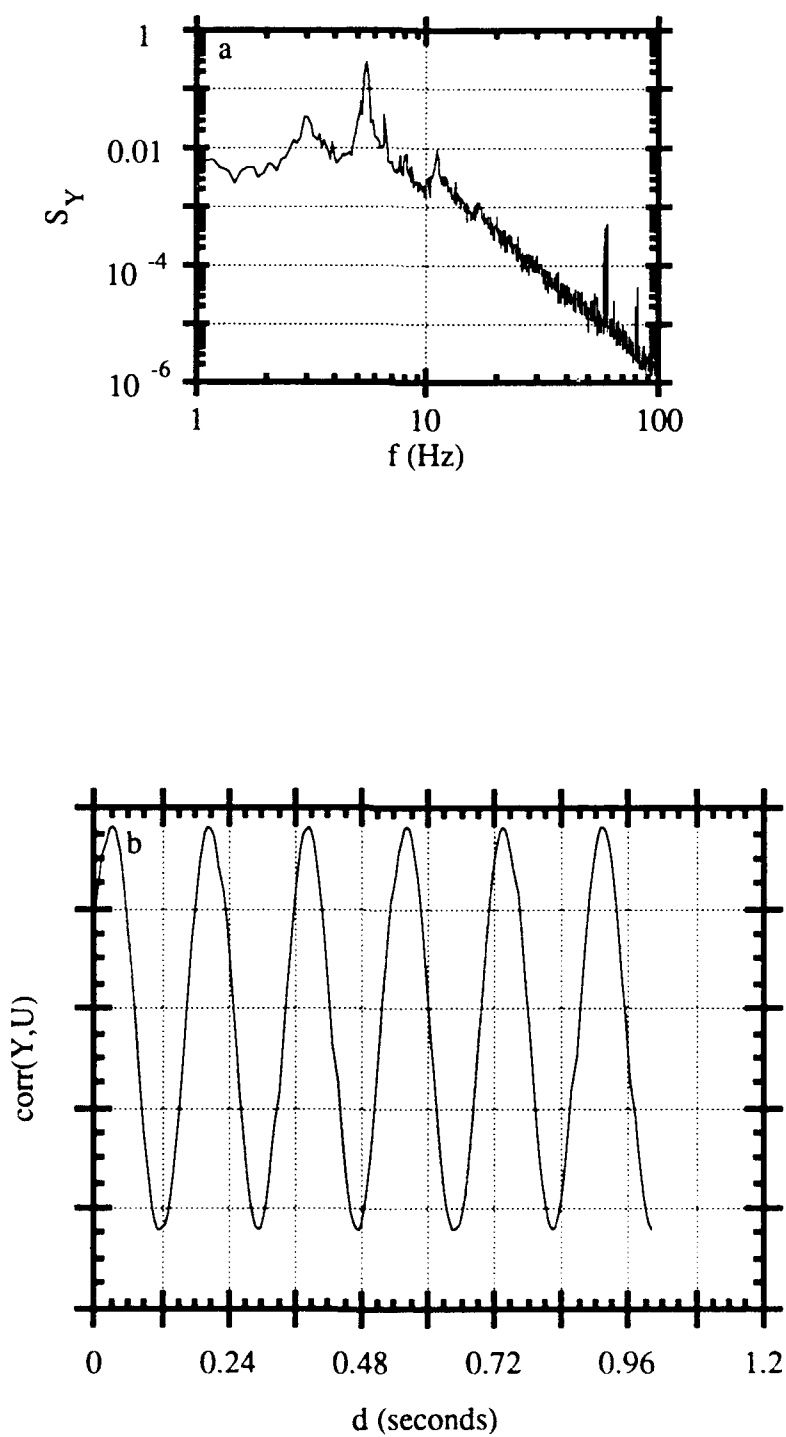


Figure I.4. Determining the proper delay time  $d$ : (a)  $S_Y$  for unforced interface; and (b), input-output correlation.

## I.4. Closed-loop results

### I.4.1 The feedback gains

Three sets of the feedback gains  $\underline{k} = (k_1, k_2)$  are selected:  $\underline{k}^1 = (0, 1)$ ,  $\underline{k}^2 = (0, -1)$ , and  $\underline{k}^3 = (-.333, -.889)$  (hereafter be referred to as configurations  $C_1$ ,  $C_2$ ,  $C_3$ , respectively) for which the respective poles of the second order system are  $-.7 \pm .71i$ ,  $+.7 \pm .71i$ , and  $+.44 \pm .38i$ . We note that in the case of an oscillator modelled by the present second order system,  $C_1$  corresponds to a damped mode at  $f=0.71f_n$ ,  $C_2$  corresponds to amplification of a mode at  $f=0.71f_n$ , and  $C_3$  introduces an amplified mode characterized by a low-frequency pole.

### I.4.2 Controller effect in the frequency domain

The effect of the controller is studied by comparing the power spectrum of the interface motion  $S_y(f)$  when the flow is unforced (UF), and with feedback (F). One common feature of all the F spectra is the presence of sidebands around  $f_N$ . This is to be expected for a system with delays because the input  $U$  to the system is a function of  $y(t - \Delta_T)$  as was noted in §I.3. Therefore, since  $\Delta$  is chosen such that

$$\Delta = \frac{n}{\omega_N} - \Delta_N$$

where  $n$  is the smallest integer such that  $n \geq \Delta_N \omega_N$ , it stands to reason that frequencies other than  $f_N$  will also be eigenfrequencies of the closed-loop system if

$$\omega_i = \frac{i}{\Delta_N + \Delta}$$

where  $i$  is any integer. As the delay time increases, more frequencies should appear in the spectrum corresponding to the eigenfrequencies observed by Reisenthel. Figure I.5 illustrates this point. For a given  $\underline{k} = (-1, 0)$   $\Delta$  is increased from 0 to 10 s. The power spectra support the conjecture that sidebands of  $f_N$  include discrete spectral peaks the separation of which is inversely proportional to  $\Delta_T$ .

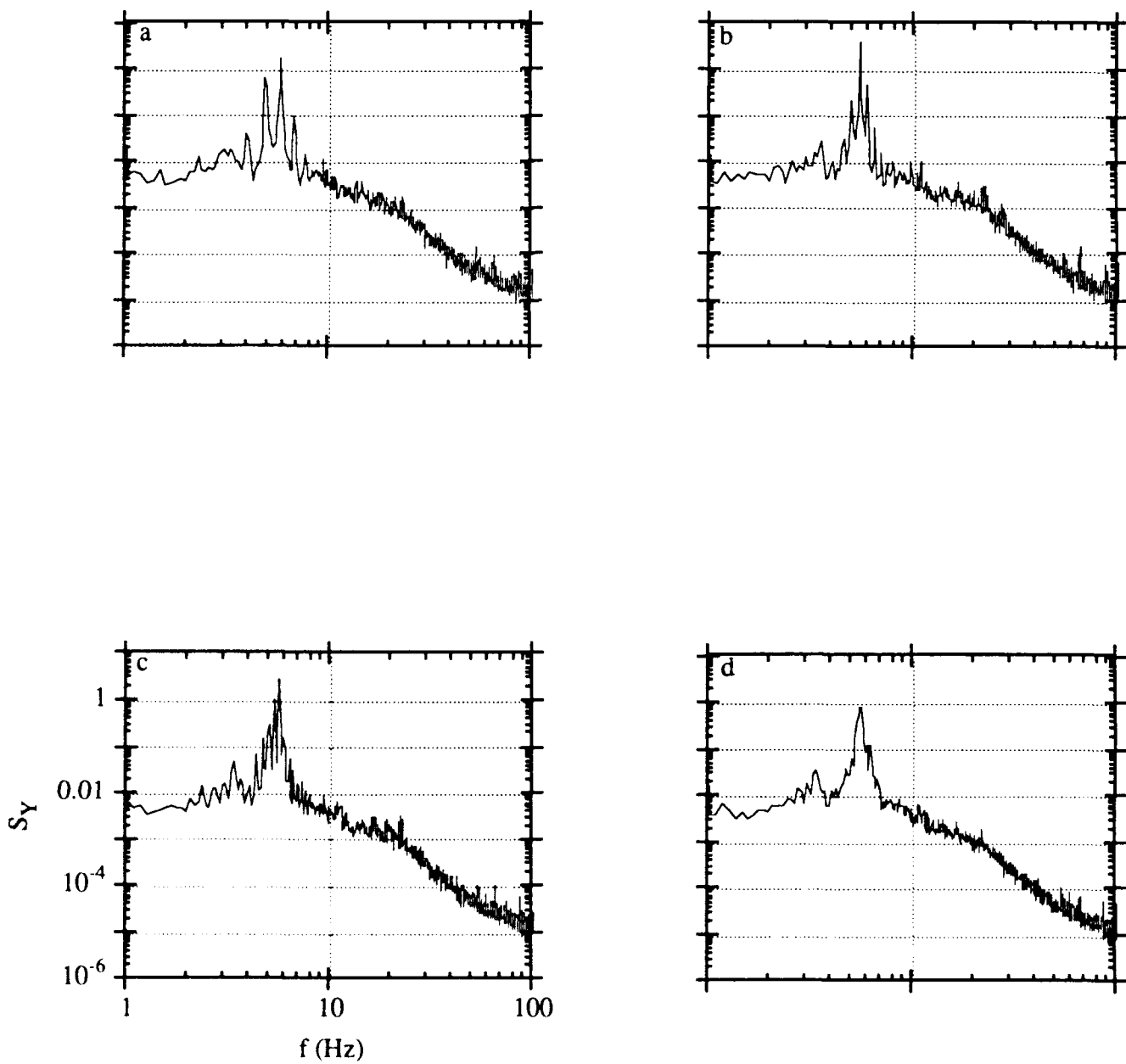


Figure I.5.  $S_Y$  for  $\underline{k} = (-1, 0)$  and  $\Delta =$  : (a) 0 s; (b) 1 s; (c) 2 s; and (d) 10 s.

Figure I.6 shows the effect of different values of  $\underline{k}$  on the power spectrum of the interface motion. The spectrum of the unforced interface shown in figure 1.6a is the same as in figure I.4a, and is shown again for reference. Figure 1.6b is the response of the interface to  $\underline{k}^1 = (0,1)$ . This is the case which should attenuate  $0.71f_N$ . Note that compared to the unforced case, there are a number of spectral peaks around the natural frequency. The magnitude of these peaks is almost equal in magnitude to the peak at the natural frequency. Although the natural frequency itself is not attenuated at this downstream location, the broadening of the spectrum in this region allows for its eventual attenuation farther downstream. This effect will be noted in the next paragraph. Figure 1.6c shows the case of  $\underline{k}^2 = (0,-1)$  which is chosen to amplify the  $.71f_N$ . In comparison with figure 1.6b, the spectral peaks at  $f_N$  is larger while the spectral peaks within the side bands are considerably smaller in figure 1.6c. In fact, in figure 1.6c, the spectral peak at  $f_N$  is almost two orders of magnitude larger than the spectral peaks at its sidebands. Figure 1.6d shows the case which is chosen to amplify a lower frequency,  $\underline{k}^3 = (-.333,-.889)$ . The effect of this feedback on the spectrum of the interface is marginal at best. This spectrum is, in fact, almost indistinguishable from the spectrum in figure 1.6c. Perhaps the only noticeable difference is a slight sharpening of some of the lower-frequency peaks in the spectrum.

The effects of feedback programs  $C_1$ ,  $C_2$ , and  $C_3$  on the flow farther downstream are substantial. These effects are assessed using an instantaneous mixing performance measure  $\mathbf{pm}(x,y,t)$

$$\mathbf{pm}(x,y,t) = \frac{(T_2 - T(x,y,t))(T(x,y,t) - T_1)}{(\Delta T)^2}$$

which is zero when the measured temperature  $T(x,y)$  is either  $T_1$  or  $T_2$ , and nonzero if  $T_1 < T(x,y,t) < T_2$ , indicating mixing. This performance measure can then be integrated in the cross-stream direction to give an integral measure of the amount of mixed fluid in the layer:

$$\mathbf{PM}(x,t) = \int_{-\infty}^{\infty} \mathbf{pm}(x,y,t) dy$$

The power spectrum  $S_{PM}(x,f) = |F(\mathbf{PM}(x,t))|^2$  gives a good measure of the spectral components of the temperature (and possibly the velocity) field, and more specifically the frequencies associated with mixing. The power spectrum  $S_{PM}(x = 15.24 \text{ cm}, f)$  is shown

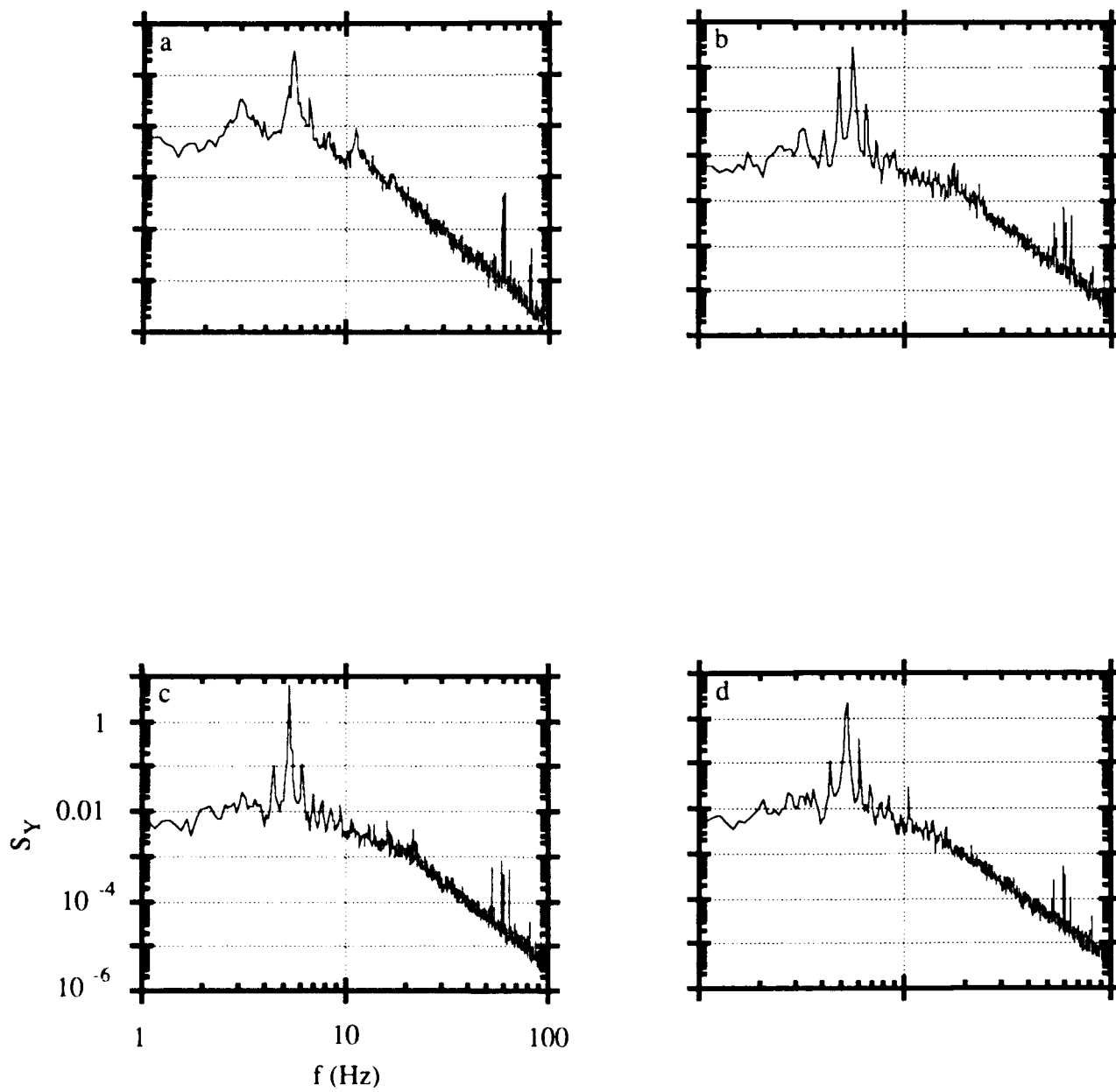


Figure I.6.  $S_Y$  for: (a) unforced; (b) configuration  $C_1$ ; (c) configuration  $C_2$ ; and (d) configuration  $C_3$

in figure I.7 for the unforced case and for feedback programs  $C_1$ ,  $C_2$ , and  $C_3$ . The unforced case (figure I.7a) shows not only a strong peak at the  $f_N$ , but also a strong spectral peak at  $f_N/2$ . This is consistent with the idea that the mixing layer grows with downstream distance by pairing interactions between the primary vortical structures. At this downstream location, the flow has already begun pairing and hence the amplitude of the subharmonic is almost as strong as that of the fundamental.

Plots of  $S_{PM}$  show the effect of the feedback much more strongly than the plots of  $S_Y$ . For example, figure I.7b corresponds to  $C_1$  (i.e.,  $\underline{k}^1 = (0,1)$ ). Notice that the features of  $S_Y$  for this case are essentially accentuated. The spectrum is filled with a number of spectral peaks, none of which can be classified as dominant. In addition, the subharmonic frequency band (i.e., around  $f_N/2$ ) shows a similar sharpening of discrete frequencies. In contrast, figure I.7c shows a very strong fundamental frequency. This suggests that  $\underline{k}^1 = (0,-1)$  does indeed amplify the natural frequency. This peak is roughly three times that of peak at  $f_N/2$ , which is a substantial increase over the unforced case, where the peak at  $f_N/2$  has approximately the same amplitude as the peak at  $f_N$ .

Perhaps the most striking effect of the feedback, however, is shown in figure I.7d, corresponding to program  $C_3$  (i.e.,  $\underline{k}^3 = (-.333, -.889)$ ). In this case, the fundamental frequency  $f_N$  is almost completely attenuated. The band of frequencies around the subharmonic frequency  $f_N$ , however, is quite broad peak. This indicates that the primary vortices are almost completely coalesced at  $x = 15.24$  cm and that the corresponding increase in the width of the shear layer is manifested by an increase in mixing.

#### *1.4.3 Mixing in the unforced shear layer*

Since it is apparent that feedback has a substantial effect on the flow, the cross-stream temperature measurements are used to quantify mixing through the instantaneous performance measure,  $\mathbf{pm}$ , the integral performance measure  $\mathbf{PM}$ , and the probability density function of temperature

$$P(T_1 \leq T \leq T_2) = \int_{T_1}^{T_2} pdf(T,y) dT .$$

The function  $pdf(T,y)$  is the probability density of finding fluid at a temperature  $T$  at a location  $y$  within the shear layer.

Figure I.8 is comprised of three composites taken at three streamwise stations  $x = 10.16$ ,  $15.24$ , and  $20.32$  cm for the unforced shear layer. Each composite includes the

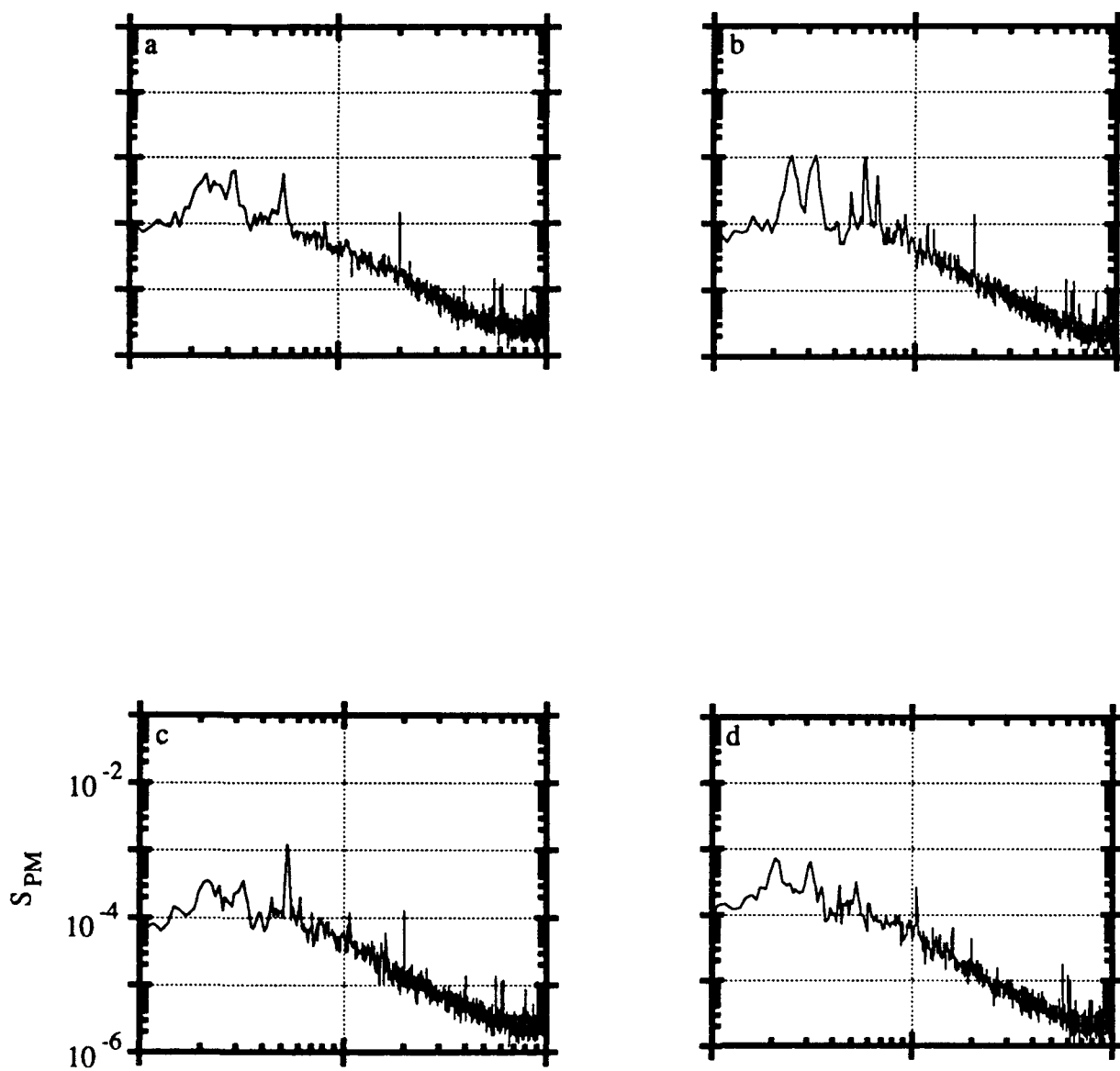


Figure I.7.  $S_{PM}$  at  $x = 15.24$  cm for: (a) unforced; (b) configuration  $C_1$ ; (c) configuration  $C_2$ ; and (d) configuration  $C_3$ .

time-averaged temperature  $T(y)$ , a false color raster image of the instantaneous temperature distribution  $T(y,t)$  over a period of 1.28 seconds, and a contour plot of *pdf* ( $T,y$ ). The color bar for  $T(y,t)$  is shown. For *pdf* ( $T,y$ ), the minimum and maximum contour levels are  $1\text{ }^{\circ}\text{C}^{-1}$  and  $3.1\text{ }^{\circ}\text{C}^{-1}$ , respectively, and the contour increment is  $.1\text{ }^{\circ}\text{C}^{-1}$ .

Other researchers, (Dimotakis 1989), have found that mixing transition in an unforced two-stream shear layer occurs at a  $Re_m = \Delta U \delta / \nu \approx 10^4$  where  $\Delta U = U_1 - U_2$  and  $\delta = \delta(x)$  is the local transverse extent of the shear layer. Profiles of  $T(y)$  yield  $\delta = 2.4, 3.8, \text{ and } 5\text{ cm}$  at  $x = 10.16, 15.24, \text{ and } 20.32\text{ cm}$ , respectively. The corresponding local Reynolds numbers are  $0.69 \times 10^4, 1.1 \times 10^4, \text{ and } 1.40 \times 10^4$  ( $\nu = .0084\text{ cm}^2/\text{s}$  and  $\Delta U = 24\text{ cm/s}$ ). Note that the kinematic viscosity of water decreases by 6.7% between  $25^{\circ}\text{C}$  and  $28^{\circ}\text{C}$ . The kinematic viscosity used here is the average of the kinematic viscosities of the two streams.

Figure I.8 depicts the natural mixing process. At  $x = 10.16\text{ cm}$  (figure I.8a) the temperature map is almost time-periodic having a period corresponding to that of the interface motion. The plot of *pdf* ( $T,y$ ) shows a negligibly small amount of mixed fluid. This is to be expected, since the local Reynolds number is below  $Re_m$ . Also of interest is  $T(y)$  which shows a distinct concave bend (i.e., towards  $T_2$ ) near the high speed stream, below which the temperature profile increases almost linearly to  $T_2$ . This is contrasted with the cross-stream the velocity profile which is similar to a hyperbolic tangent profile. The bend begins above the geometric center of the test section,  $y = 0\text{ cm}$ . We also note that the temperature distribution  $T(y,t)$  shows that instantaneous temperature profiles  $T(y;t)$  can be either single-valued or double-valued in  $y$  corresponding to the rollup of the primary vortices. These profiles become multiple-valued farther downstream with the progression of the rollup of the primary vortices

It is clear that in the absence of mixing, the shape of the mean temperature profile within the shear layer, depends on the time fraction that each of sensors measures either  $T_1$  or  $T_2$  (for a given sampling period). The concave bend at the present streamwise station is a result of the rollup of the interface between the two streams. The profile appears to be (almost) linear below the cross-stream domain where the instantaneous temperature profiles become multivalued.

The temperature distribution  $T(y,t)$  at  $x = 15.24\text{ cm}$  (figure I.8b) shows that at this streamwise station the primary vortices begin to pair as is evidenced by the variations in the spacings between the vortices. Note that the cross-stream displacement of the primary vortices results in cross-stream elevations where the passage frequency of the coherent structures is lower than  $f_N$ . We also note that there is a small increase in mixing at this station as shown by contours of the temperature probability density function *pdf* ( $T,y$ ).



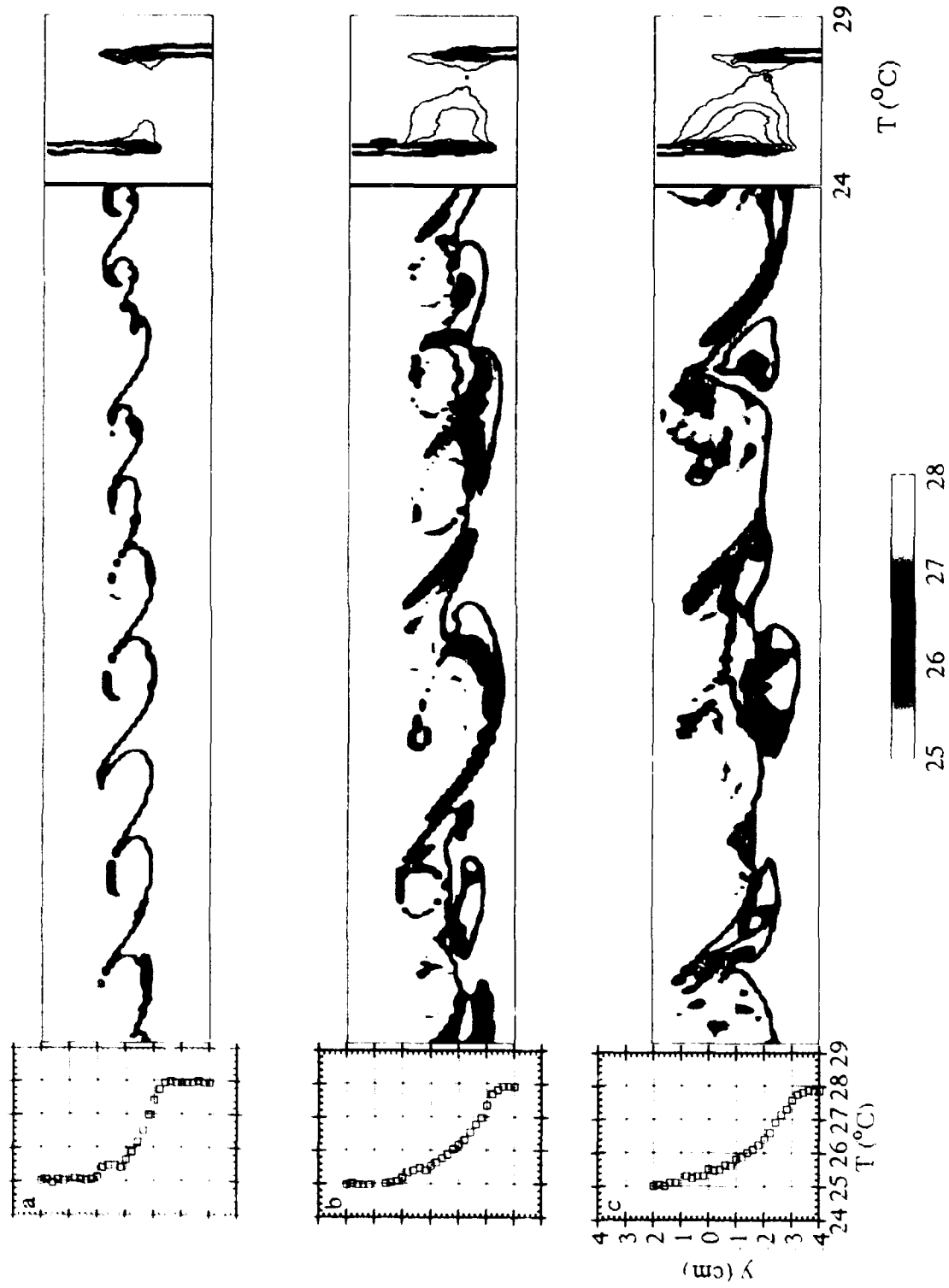


Figure 1.8.  $T(y)$ ,  $T(y, t)$ , and  $pdf(T, t)$  for the unforced flow at  $x =$  : (a) 10.16 cm; (b) 15.24 cm; and (c) 20.32 cm.

Similar to the mean temperature profile in figure I.8a,  $T(y)$  at  $x = 15.24$  cm also has a concave bend which corresponds to flow regions where the instantaneous temperature profile  $T(y;t)$  is multivalued. The presence of the multivalued temperature profiles suggests that the fluid within the primary vortices is rolled into stretched layers which retain their identity. As will be shown below these stretched regions give rise to an increase in mixing.

At  $x = 20.32$  cm the shear layer appears to undergo mixing transition (figure I.8c). The temperature distribution  $T(y,t)$  indicates that in contrast to  $x = 15.24$ , the fluid within the primary vortices is better mixed. This is also confirmed by contours of  $pdf(T,y)$  which has a higher peak near  $T_1$ , suggesting that the volumetric mixing ratio of high- to low-speed fluids is greater than 1. Nevertheless, the cross-stream width of  $pdf(T,y)$  suggests that some mixing occurs over the entire width of the shear layer. The concave bend which is in the upstream profiles is almost (although not completely) imperceptible owing to the diminution in the occurrence of multivalued instantaneous temperature profiles and as a result, the mean temperature profile  $T(y)$  is smooth. We note, however, that  $|dT/dy|$  is largest at the low-speed edge of the shear layer. This suggests that the instantaneous temperature gradients are larger there, and that the fluid temperature is more uniform (and better mixed) near the high-speed side.

#### *1.4.4 Mixing with feedback*

In what follows, the shear layer is subjected to feedback configurations  $C_1$  (figure I.9),  $C_2$  (figure I.10), and  $C_3$  (figure I.11). While there are a number of substantial differences between the unforced flow and the forced flows, the forced flows have a number of common features. Compared to the unforced case, in all three configurations the rollup of the primary vortices apparently starts closer to the flow partition. Hence, at  $x = 10.16$  cm the rollup appears to be far more advanced compared to the unforced case. Earlier rollup implies that the temperature interface is substantially strained allowing for localized mixing to occur further upstream through larger interfacial area. Therefore, all feedback configurations are to enhance mixing relative to the unforced case.

At  $x = 10.16$  cm (figure I.9a),  $pdf(T,y)$  shows some more mixed fluid near  $y = 0$  compared to the unforced case. Apparently this mixing occurs at rolled temperature interfaces. The mean temperature profile exhibits a concave bend which is considerably weaker than the corresponding bend in the unforced profile, presumably because the instantaneous temperature profiles are smoother as a result of enhanced mixing. At  $x = 15.24$  cm,  $pdf(T,y)$  has a definite peak at approximately  $T = 26^\circ \text{C}$  and  $y = -1.5$  cm

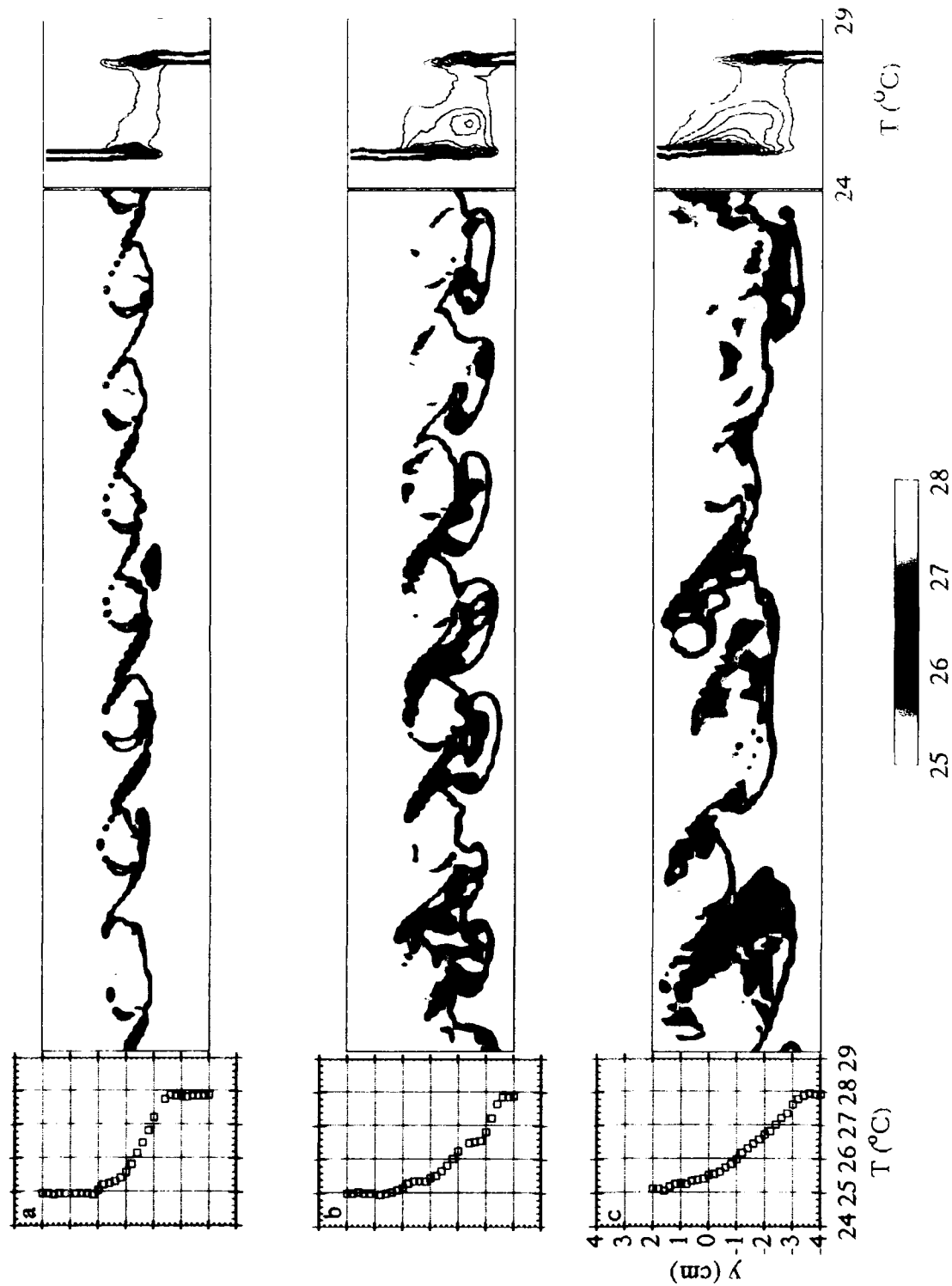


Figure I.9.  $T(y)$ ,  $T(y, t)$ , and  $pdf(T, y)$  for feedback configuration  $C_1$  at  $x =$  : (a) 10.16 cm; (b) 15.24 cm; and (c) 20.32 cm.

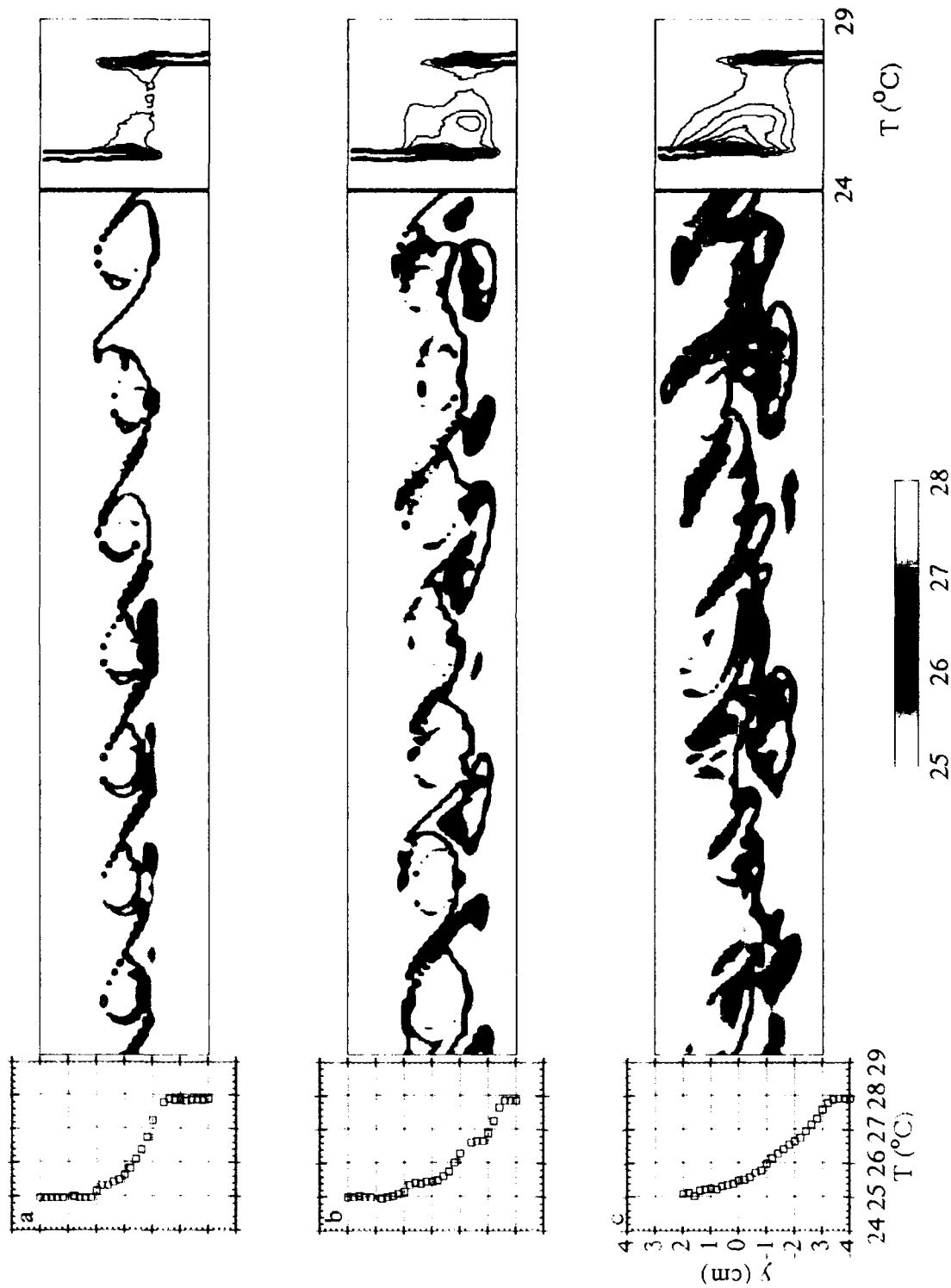


Figure I.10.  $T(y, t)$ ,  $T(y, t)$ , and  $pdf(T, y)$  for feedback configuration  $C_2$  at  $x =$  : (a) 10.16 cm; (b) 15.24 cm; and (c) 20.32 cm.

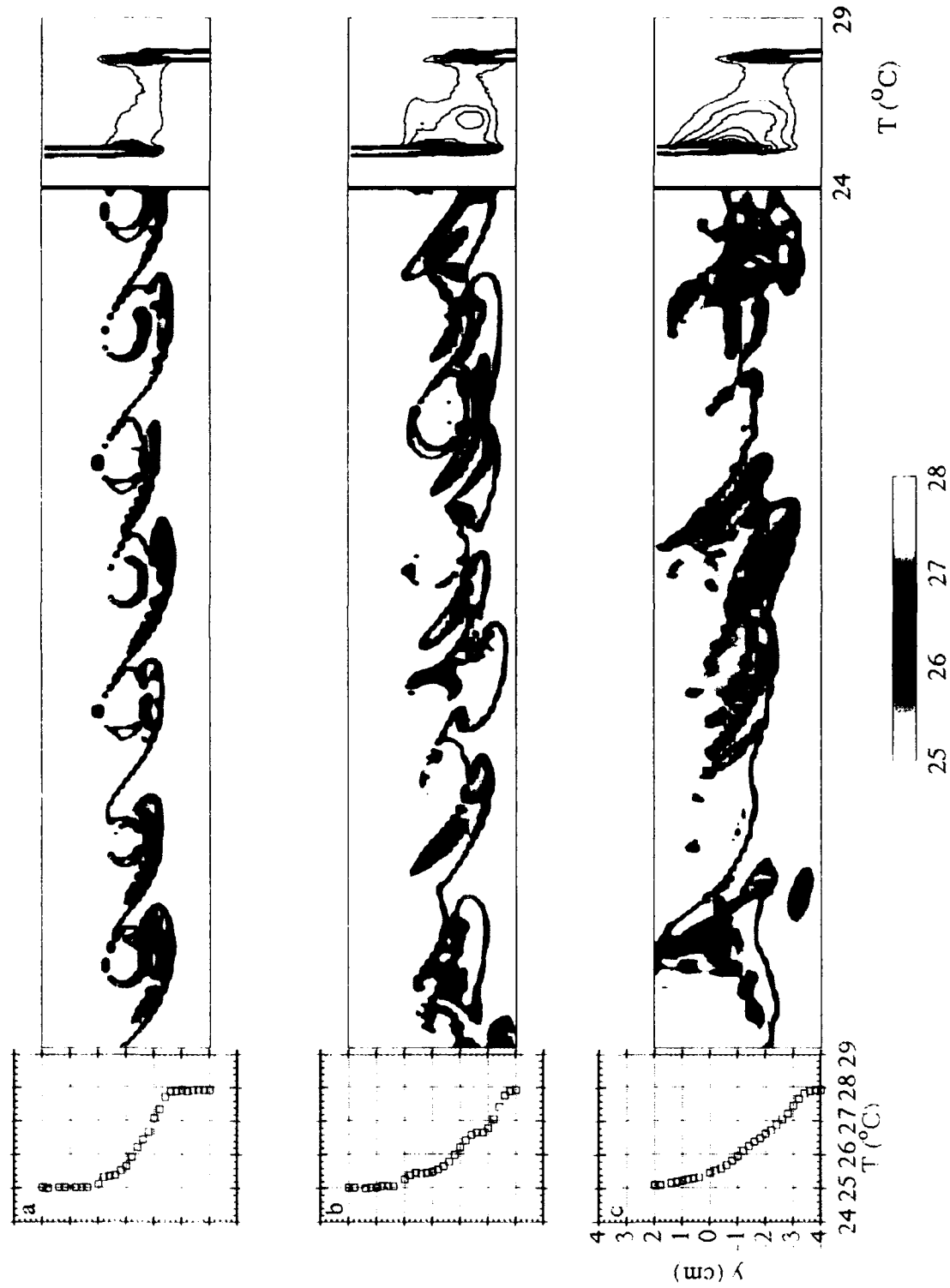


Figure I.11.  $T(y)$ ,  $T(y, t)$ , and  $pdf(T, y)$  for feedback configuration  $C_3$  at  $x =$  : (a) 10.16 cm; (b) 15.24 cm; and (c) 20.32 cm.

corresponding to distortion of  $T(y)$  which is not present in the corresponding unforced profile (figure I.8b). Other than that, however, the two profiles are similar.

The similarity between plots of  $T(y)$  and  $pdf(T,y)$  for the unforced case and configuration  $C_1$  at  $x = 20.32$  cm (figures I.8c and I.9c, respectively) suggest that the effect of the feedback is diminished even though the plots of  $T(y,t)$  are not similar. Comparison  $T(y,t)$  for both cases shows that the main difference is that when the flow is forced with configuration  $C_1$ , the large structures vary more in size and cross-stream position than those in the unforced case. Note that compared to figure I.9b, the peak of  $pdf(T,y)$  is considerably closer to  $T_1$ . This suggests that at this streamwise station entrainment of the low-speed fluid is suppressed, resulting in a decrease of the temperature of the mixed fluid towards the high-speed temperature  $T_1$ .

In strong contrast to configuration  $C_1$ , configuration  $C_2$  (figures I.10a-c) is apparently equivalent to strong forcing at a frequency which is close to  $f_N$ , as may be judged by the minimal variations in the size and passage frequency of the primary vortices throughout the streamwise domain of measurements. We note that at all streamwise locations  $pdf(T,y)$  shows more mixing when the shear layer is forced with configuration  $C_2$  than for the unforced case. Although the flow structure for configuration  $C_2$  is significantly different than that for configuration  $C_1$ , the  $pdf$ s are qualitatively similar.

Configuration  $C_3$  (figure I.11a-c) amplifies a pole at  $.38f_N$ , and the plots of  $T(y,t)$  show that low frequencies near the subharmonic are indeed induced by this mode of feedback. Although at  $x = 10.16$  cm (figure I.11a) these low frequencies are not yet apparent, the width of the layer is increased compared to the unforced case (and configurations  $C_1$  and  $C_2$ ). This increase is apparent from profiles of the mean temperature distribution. The growth in the width of the shear layer is accompanied by the appearance of "tongues" of cold (high-speed fluid) at the layer's low-speed edge which is displaced to  $y \approx -1.5$  cm (compared to  $y \approx -1$  cm for the other feedback configurations). The temperature distribution  $T(y,t)$  at  $x = 15.24$  cm (figure I.11b) is somewhat more irregular in time than the corresponding distribution for configuration  $C_2$ , and cross-sections of the primary vortices appear to be more distorted in the cross-stream direction. These irregularities lead to an increase in the cross-stream spreading of the shear layer, and the appearance of lower frequencies at  $x = 20.32$  cm (figure I.11c). In fact, only three large structures are apparent within the data record, corresponding to a frequency of approximately 2.34 Hz in good agreement with the frequency predicted by the model ( $.38f_N$ , or 2.15 Hz) and the peak in the power spectrum of  $PM$  at  $x = 15.24$  cm (figure I.7).

That the low frequency vortices are well-mixed, suggests that configuration  $C_3$  is useful for mixing enhancement. The region over which mixing occurs, which is defined here as  $\rho df(T,y) > .1 \text{ } ^\circ\text{C}^{-1}$ , is wider at  $x = 15.24 \text{ cm}$  for configuration  $C_3$  (3.43 cm) than for configurations  $C_1$  and  $C_2$  (3.08 cm) and the unforced case (2.74 cm). The increase in shear layer thickness may account for the increase in mixing when configuration  $C_3$  is used.

#### *1.4.5 Variation of mixing with downstream distance*

The streamwise variation of mixedness can be inferred from the integral performance measure  $\mathbf{PM}(x)$ . Figure I.12 shows a plot of  $\mathbf{PM}(x)$  at 11 streamwise stations for the unforced flow and the three feedback configurations. The unforced flow has the lowest value of  $\mathbf{PM}$  at all streamwise stations. As has been mentioned previously, the effect of forcing at all feedback configurations is induce an earlier rollup of the two-dimensional vortices thereby enhancing mixing. The integral performance measure for the unforced shear layer increases almost linearly between  $x = 10 \text{ cm}$  and  $20 \text{ cm}$  where it begins to level off (at  $x = 22.8 \text{ cm}$  the width of the shear layer is approximately equal to the width of the sensor rake).

By contrast, the distributions  $\mathbf{PM}(x)$  for the feedback configurations have segments where  $d\mathbf{PM}/dx \approx 0$ , which is reminiscent of streamwise distributions of the reaction product in a harmonically forced chemically-reacting shear layer (Roberts 1985). Distributions of  $\mathbf{PM}(x)$  for configurations  $C_1$  and  $C_2$  are nearly identical. Hence, even though  $T(y,t)$  appears to be substantially different (figures I.9c and I.10c) for these two cases, the amount of mixed fluid is nearly the same. For these configurations the streamwise domain  $15 \text{ cm} < x < 19 \text{ cm}$  is characterized by a linear growth of  $\mathbf{PM}(x)$ , and  $d\mathbf{PM}/dx$  is the same as for the unforced case ( $0.026 \text{ cm/cm}$ ). However, there are two streamwise domains where  $\mathbf{PM}(x) \approx \text{const.}$  ( $12 \text{ cm} < x < 15 \text{ cm}$ , and  $19 \text{ cm} < x < 21 \text{ cm}$ ) where apparently no mixing occurs ostensibly because no fresh fluid is entrained from the low-speed stream (e.g., figures I.9c and I.10c). A similar diminution in mixing also occurs for configuration  $C_3$  for  $16 \text{ cm} < x < 20 \text{ cm}$ . Hence, most of the mixing for  $C_3$  occurs upstream of  $x = 16 \text{ cm}$  and downstream of  $x = 20 \text{ cm}$ . These plots suggest that different control parameters may be desirable to optimize mixing at a given downstream location. Although configuration  $C_3$  gives the highest values of  $\mathbf{PM}(x)$  at most streamwise stations, it appears that configurations  $C_1$  and  $C_2$  may give higher values of  $\mathbf{PM}(X)$  either far upstream or far downstream. We note that the present feedback gains are not

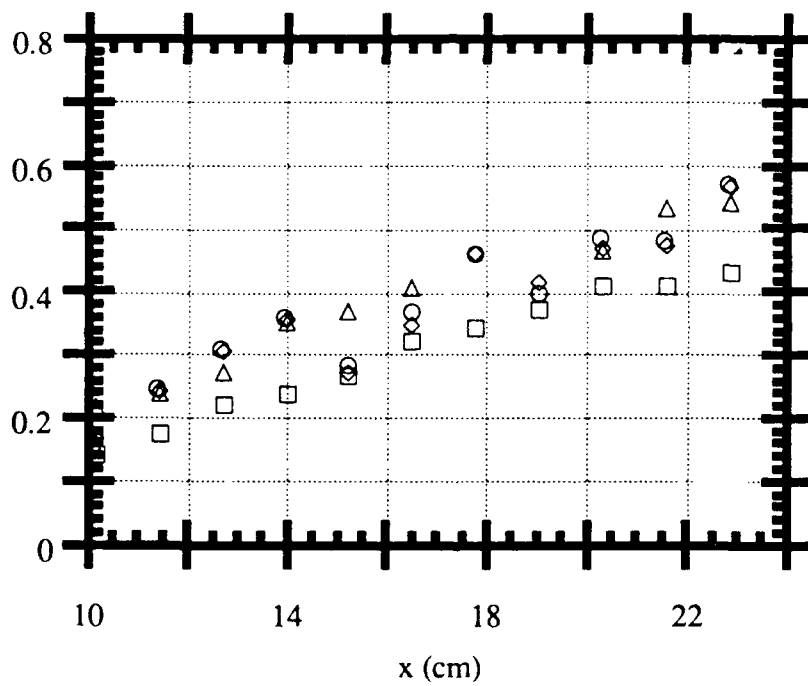


Figure I.12.  $PM(x)$  for the unforced flow ( $\square$ ),  $C_1$  ( $\circ$ ),  $C_2$  ( $\diamond$ ), and  $C_3$  ( $\triangle$ ).



specifically chosen for optimization of mixing. Hence a different feedback configuration may be the more useful from the standpoint of maximizing **PM**.

#### *1.4.6 Effect of small scale motions*

It has been well documented that small-scale fluid motions are necessary for efficient mixing at the molecular level. The control schemes discussed in the previous sections utilize spanwise-uniform excitation to control the motion of the temperature interface between the two streams and thus affect the evolution of the primary vortices. The premise is that this methodology will yield control authority over the (nominally two-dimensional) entrainment and entrainment ratio. It is clear, however, that an important mechanism in the promotion of mixing is small-scale motions induced by the appearance of packets of streamwise counter-rotating vortex pairs in the braids region between the primary vortices. Because these vortices can be effectively triggered by using spanwise-nonuniform excitation (Nygaard and Glezer 1991), feedback configurations  $C_1$ ,  $C_2$ , and  $C_3$  are used in conjunction with spanwise-periodic *time-invariant* excitation applied with the linear array of 32 surface heaters (§1.2.1). The spanwise wavelength chosen for the present investigations is synthesized by four heating elements (approximately 2.66 cm) and the spanwise waveform is essentially a square wave having a duty cycle of 50%.

In figures I.13a-c, (similar to figures I.8 through I.11) the flow is forced open-loop with a time-invariant spanwise periodic (TISP) excitation which is used below as a baseline for comparison with the feedback configurations. In what follows, all measurements are taken at spanwise positions corresponding to the "head" of a streamwise vortex (in the parlance of Nygaard and Glezer). At  $x = 10.16$  cm (figure I.13a), *pdf* ( $T, y$ ) shows a small increase in mixed fluid compared to the unforced case (figure I.8). This is to be expected because at these operating conditions the streamwise vortices are formed further downstream. We note, however, that the concave bend in  $T(y)$  is smoother than in the corresponding profile in figure I.8a, indicating an increase in the width of the mixing region compared to the unforced case. The temperature distribution  $T(y, t)$  shows that the vortical structures are not as regular as in the unforced case, but this may be attributed to the three-dimensional disturbances induced by the heater array. At  $x = 15.24$  cm, the differences between the TISP-forced case and the unforced case are more pronounced. The distribution  $T(y, t)$  in figure I.13b shows more low-speed (i.e., high-temperature) and mixed fluid within the vortical structures than in the unforced case. In both cases, mixing apparently occurs within a band near the outer edges of the primary vortices. In the TISP case, these bands are significantly wider, suggesting an increase in mixing compared to the

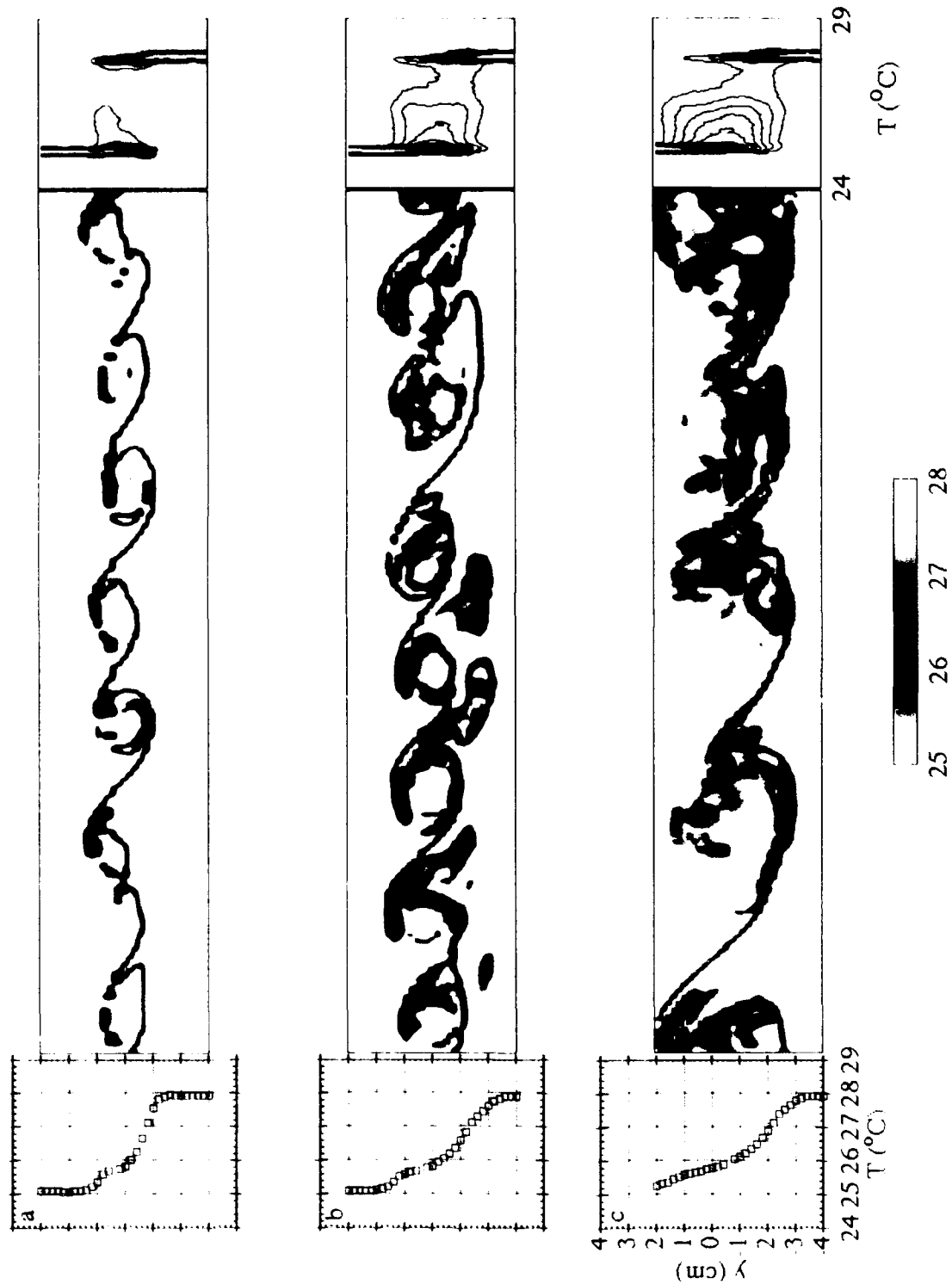


Figure I.13.  $T(y)$ ,  $T(y, t)$ , and  $pdf(T, y)$  for TISP forcing at  $x =$  : (a) 10.16 cm; (b) 15.24 cm; and (c) 20.32 cm.

unforced case. Furthermore, contours of  $pdf(T,y)$  show that the in the forced flow mixing occurs over a wider domain in the cross stream direction

#### *1.4.7 Time-invariant spanwise-periodic excitation with feedback*

The three feedback configurations  $C_1$ ,  $C_2$ , and  $C_3$  (§1.4.1) are used in conjunction with the time-invariant spanwise-periodic excitation described in §1.4.6 (having a spanwise wavelength of 2.66 cm). These configurations are referred to below as the 3D cases C3D<sub>1</sub>, C3D<sub>2</sub>, and C3D<sub>3</sub>, respectively. Plots of spectra of the performance measure (not shown) for these three cases are qualitatively similar to the cases  $C_1$ ,  $C_2$ , and  $C_3$  (referred to below as the 2D cases), although the spectral peaks in the present experiments are not as high. The amount of mixed fluid resulting from the 3D cases is significantly higher than the corresponding 2D cases. Furthermore, there are substantial differences in the amount of mixed fluid between the three 3D cases.

Figure I.14a-c shows the results for configuration C3D<sub>1</sub>. The mean temperature profile  $T(y)$  at  $x = 10.16$  cm (I.14a) has a concave bend while the corresponding profile for case  $C_1$ , has no bend at all. This bend is centered around  $y = 0$  and corresponds to the region where mixing is taking place, as shown in contours of  $pdf.(T,y)$ . The distribution  $T(y,t)$  shows that at this streamwise station the rollup of the shear layer is such that the amount of entrainment from the low-speed side is considerably reduced. This effect is even more pronounced at  $x = 15.24$  cm, where isolated concentrations of partially mixed fluid are essentially suspended in the high-speed side and are connected to the low-speed stream by narrow tongues of low-speed fluid. It is important to note that the interface separating the unmixed low-speed fluid (at  $T = T_2$ ) from fluid having temperatures  $T < T_2$  is relatively flat. This suggests that at these streamwise station there is little entrainment of low-speed fluid into the layer. At  $x = 20.32$  cm, the temperature interface described above is not flat and exhibits low-frequency undulations which suggest that the entrainment of low-speed fluid is resumed. The temperature of the fluid within the primary vortices is lower at  $x = 20.32$  than at  $x = 15.24$  cm. This is consistent with the idea that close to the flow partition fluid is entrained primarily during the rollup of the primary vortices, and very little entrainment takes place between  $x = 15.24$  cm and  $x = 20.32$  cm. Entrainment is resumed when pairing takes place.

The results for configuration C3D<sub>2</sub> are shown in figure I.15. As for configurations  $C_1$  and  $C_2$ , the contours of  $pdf(T,y)$  at  $x = 15.24$  cm show a lower peak compared to configuration C3D<sub>1</sub>. The temperature distributions  $T(y,t)$  in figures I.15a-c show that the

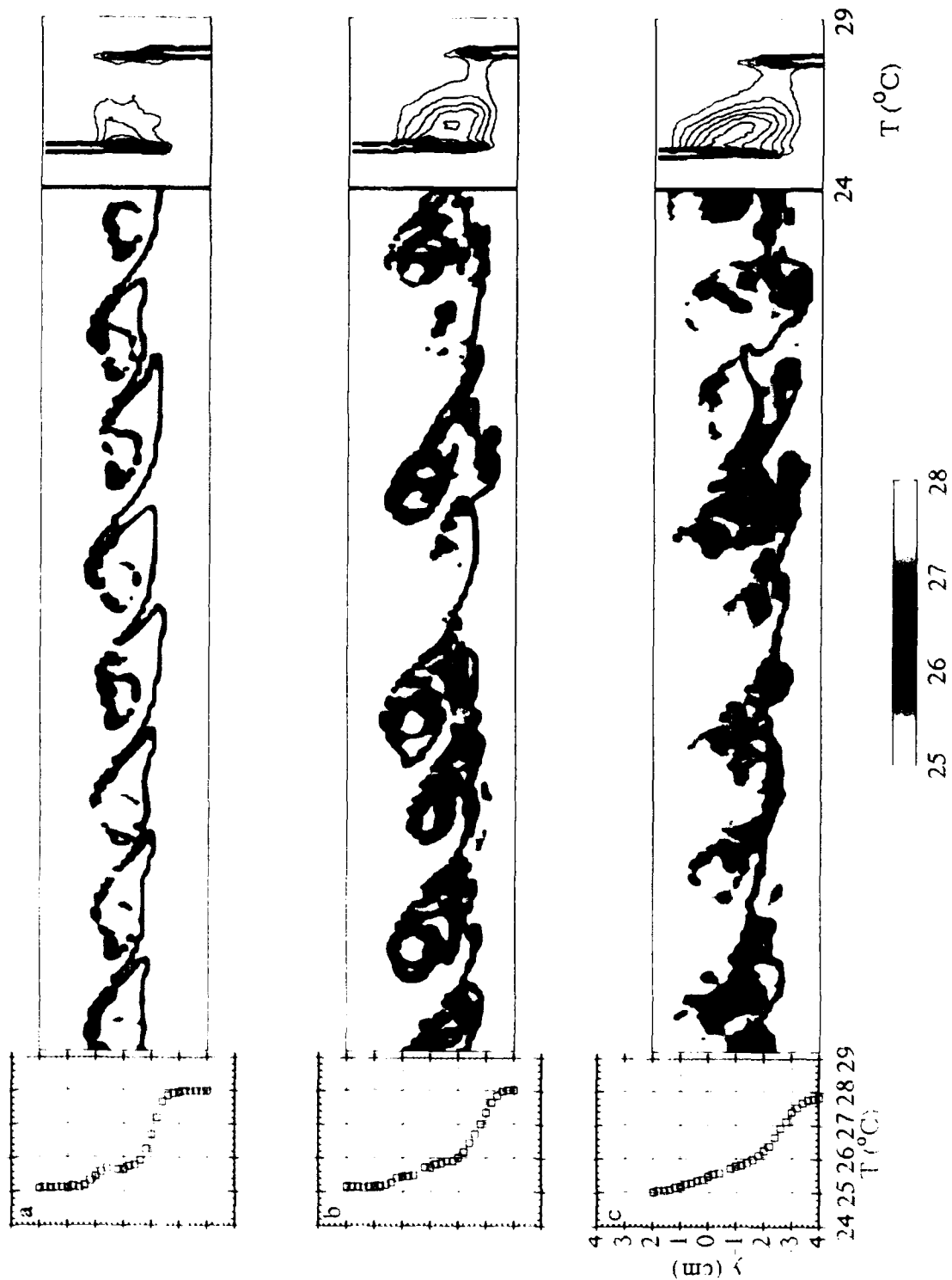


Figure I.14.  $T(y)$ ,  $T(y, t)$ , and  $pdf(T, y)$  for feedback configuration C3D<sub>1</sub> at  $x =$  : (a) 10.16 cm; (b) 15.24 cm; and (c) 20.32 cm.

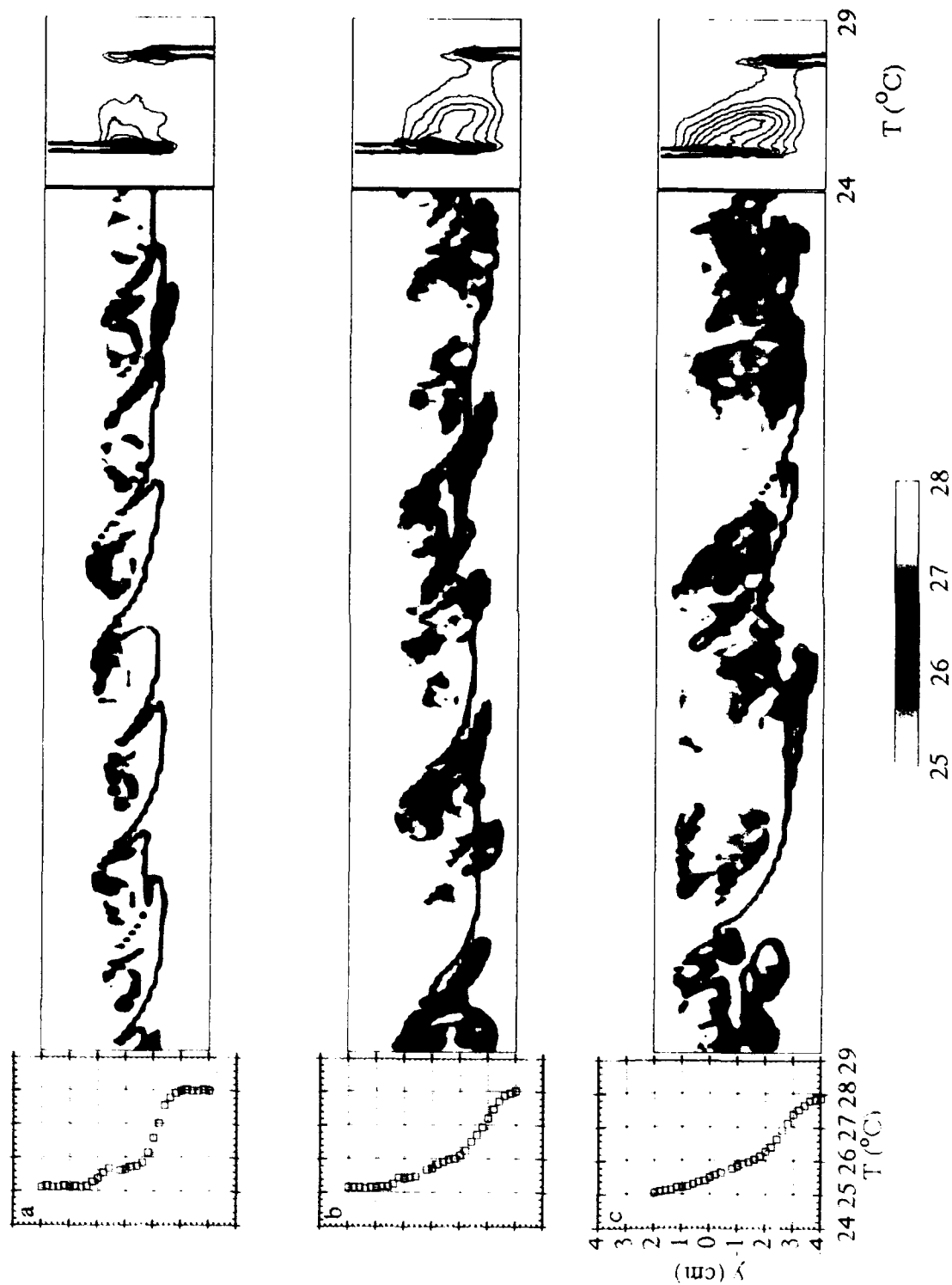


Figure 1.15.  $T(y, t)$ ,  $T(y, t)$ , and  $pdf(T, y)$  for feedback configuration C3D<sub>2</sub> at  $x =$  : (a) 10.16 cm; (b) 15.24 cm; and (c) 20.32 cm.

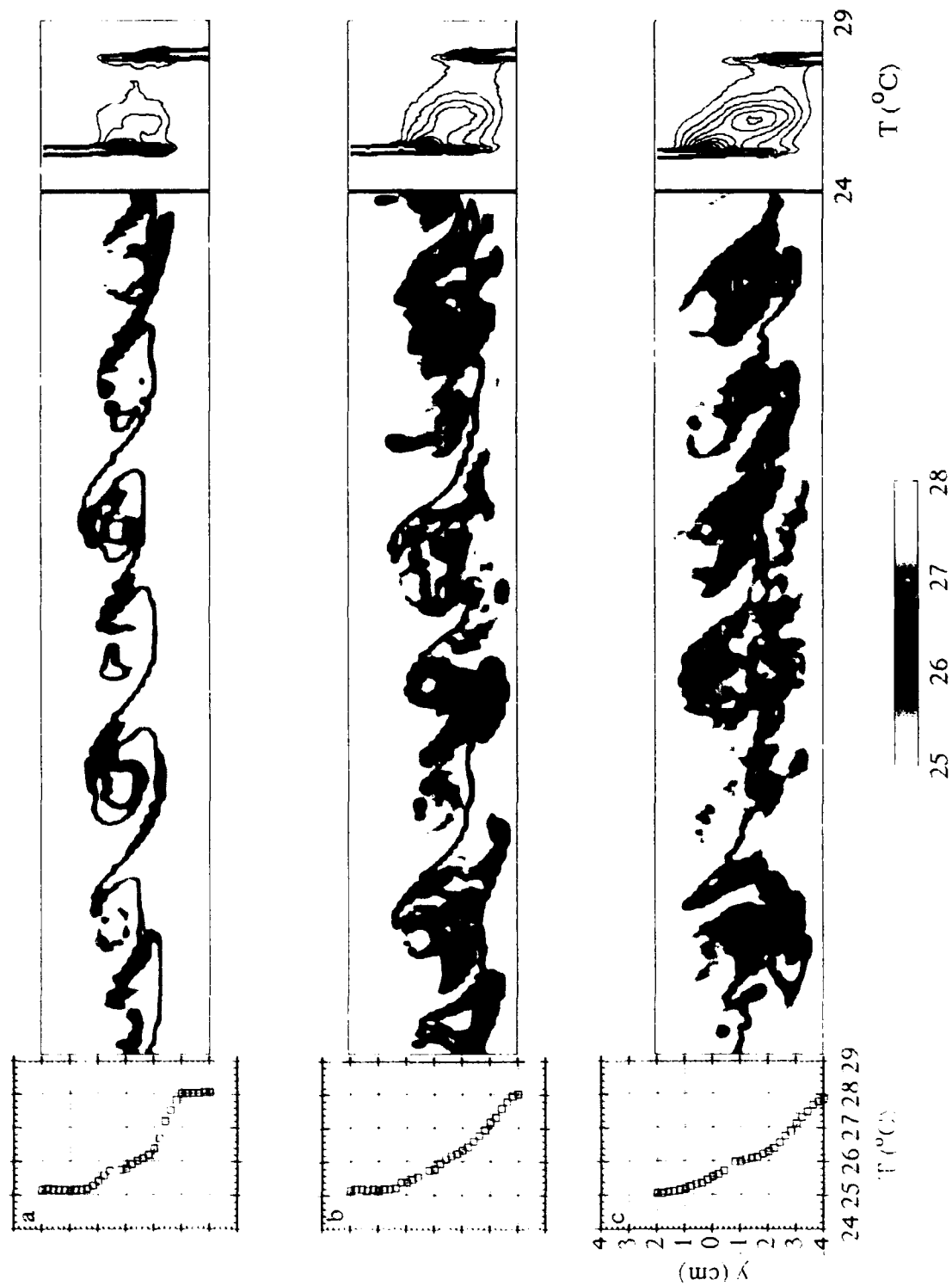


Figure 1.16.  $T(y)$ ,  $T(y, t)$ , and  $pdf(T, y)$  for feedback configuration C3D<sub>3</sub> at  $x =$  : (a) 10.16 cm; (b) 15.24 cm; and (c) 20.32 cm.

dominant frequency through the streamwise domain of measurement is  $f_N$ , although the data at  $x = 20.32$  suggests the emergence of a subharmonic.

The results for configuration C3D3 are shown in figure I.16. The most noticeable feature of  $T(y,t)$  is the absence of low-frequency patches of mixed fluid at  $x = 20.32$  cm compared to configuration C3. That the predominant convection frequency of mixed fluid is  $f_N$  suggests that the efficacy of the feedback in this configuration is diminished compared to C3. We note that recent data (not reported here) shows that when feedback configuration C3D3 is implemented using the linear array of surface heaters, the controller is successful in imposing the desired low frequency on the flow. Nevertheless, the present C3D3 configuration leads to a substantial increase in mixing compared to the other configurations. Contours of  $pdf(T,y)$  at  $x = 20.32$  cm have a sharp peak at  $T = 26^\circ$  C and  $y = -1.65$  cm. A similar peak is not present in corresponding plots for configurations C3D1, and C3D2, and furthermore, the cross-stream domain in which mixing is detected is smaller for these configurations. (Similar effects are observed in configuration C3 compared to configurations C1, and C2.

A plot of  $PM(x)$  is shown in figure I.17 for configurations TISP, C3D1, C3D2, and C3D3. This plot shows the same trends as for the corresponding 2D cases (figure I.12). The TISP case has the least mixing. The importance of spanwise nonuniform excitation to the mixing process is demonstrated by the fact that even the TISP case has a higher values of  $PM$  compared to the "best" 2D case (configuration C3).

#### *1.4.8 Detailed comparison of feedback configurations C3D3 and C3*

In what follows, configurations C3D3 and C3 (which lead to more mixing than the other 3D and 2D configurations ) are compared in more detail. Figures I.18a and I.19a include plots of the mean and instantaneous temperature distributions  $T(y)$ , and  $T(y,t)$ , the temperature probability density function  $pdf(T,y)$ . Figures I.18b and I.19b are contour plots of the (squared) magnitude of the temperature pseudogradient  $G(y,t)$ :

$$G(y,t) = \left( \frac{\partial T}{\partial y} \right)^2 + \left( \frac{1}{U_c} \frac{\partial T}{\partial t} \right)^2$$

where

$$U_c = \frac{U_1 + U_2}{2}.$$

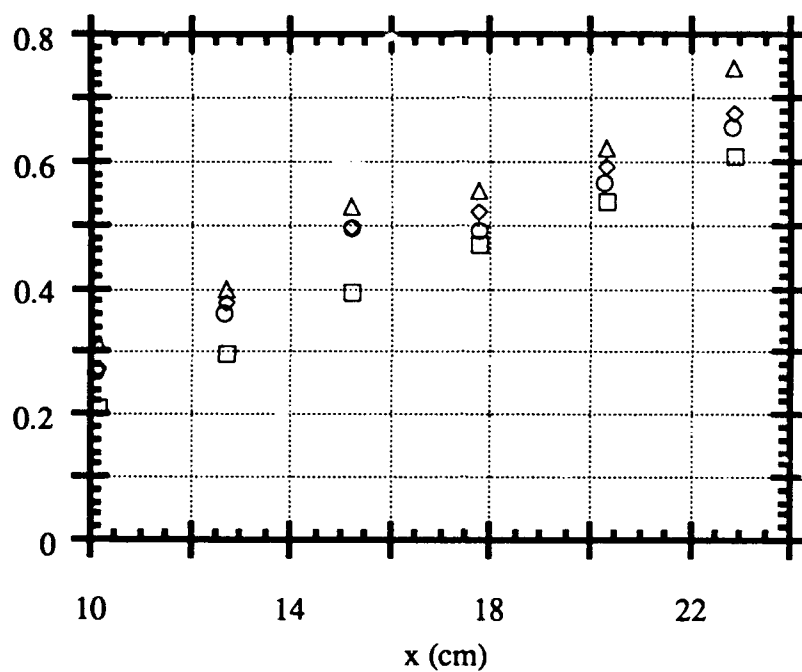


Figure I.17.  $PM(x)$  for TISP(□), C3D<sub>1</sub>(○), C3D<sub>2</sub>(◇), and C3D<sub>3</sub>(Δ).



Contours start at  $25\text{ }^{\circ}\text{C}^2/\text{cm}^2$ , the maximum contour is  $200\text{ }^{\circ}\text{C}^2/\text{cm}^2$  and the contour increment is  $25\text{ }^{\circ}\text{C}^2/\text{cm}^2$ . Figures I.18.c and I.19c are the mean and instantaneous distributions of performance measures  $\text{pm}(y)$  and  $\text{pm}^2(y,t)$ , respectively.

Because mixing of temperature ultimately relies on conduction where the heat flux  $q$  is given by

$$q = -kA\nabla T ,$$

and the magnitude (squared) of the heat flux is proportional to

$$|q|^2 \propto A^2 |\nabla T|^2 .$$

then contours of  $G(y,t)$  show where conduction occurs at temperature interfaces. This is similar to the scalar energy dissipation rate field of Buch and Dahm (1991), which gives the local instantaneous rate of molecular mixing in the flow. If conduction occurs over a large surface area  $A$ , then it may be argued that conditions which are conducive for mixing exist. Figure I.18b shows that for configuration  $C_3$ , contours of  $G(y,t)$  approximately coincide with the outer edges of the primary vortices in  $T(y,t)$ . This suggests that for this configuration, conduction occurs only around edges of the primary vortices, and not in their cores. By contrast, contours of  $G(y,t)$  for configuration  $C3D_3$  suggest that the temperature interface between the two streams is contorted and convoluted in time, and suggest a substantial increase in surface area over which mixing can take place. That local interfaces between hot and cold fluid are smaller (compared to  $C_3$ ) implies that the ratio of surface area to volume is greater for  $C3D_3$ . This is a direct result of the appearance of small scale motions induced by the forced streamwise vortices.

Figures I.18c and I.19c show the effect of configurations  $C_3$  and  $C3D_3$  on mixing. Raster plots of  $\text{pm}(y,t)$  show that for  $C_3$ , small amount of mixing occurs in thin sheet-like structures near the perimeters (in the cross stream plane) of the primary vortices. When the flow is subjected to configuration  $C3D_3$ , (figure I.19c), mixedness is clearly increased and the mixed fluid is more uniformly distributed within the cores of the primary vortices. In fact, almost all the fluid within the shear layer at this streamwise location is mixed. Profiles of the mean performance measure profiles  $\text{pm}(y)$  offer additional evidence that mixing for  $C_3$  occurs near the edges of the cores of the primary vortices whereas for  $C3D_3$  mixing is approximately uniform within the cores. Peaks in  $\text{pm}(y)$  for  $C_3$  occur at the same locations as the concave bends in  $T(y)$ ; while the broad peak in  $\text{pm}(y)$  for  $C3D_3$  results in a smooth  $T(y)$  profile.

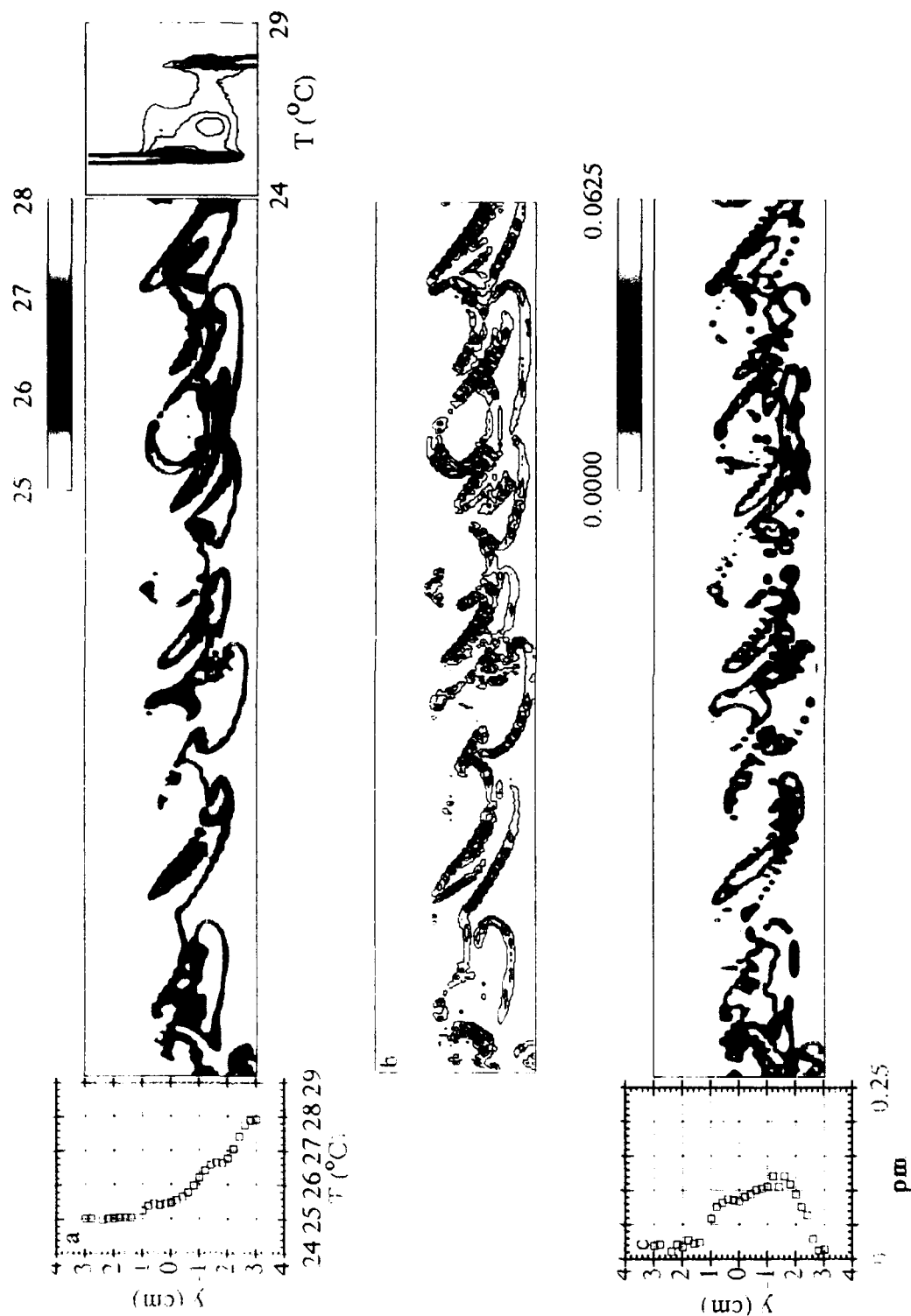


Figure 1.18 (a)  $T(y, t)$  and  $pdf(T, y)$ ; (b)  $G(y, t)$ ; and (c)  $pm(y)$  and  $pm^2(y, t)$  for feedback configuration  $C_3$  at  $x = 15.24$  cm.

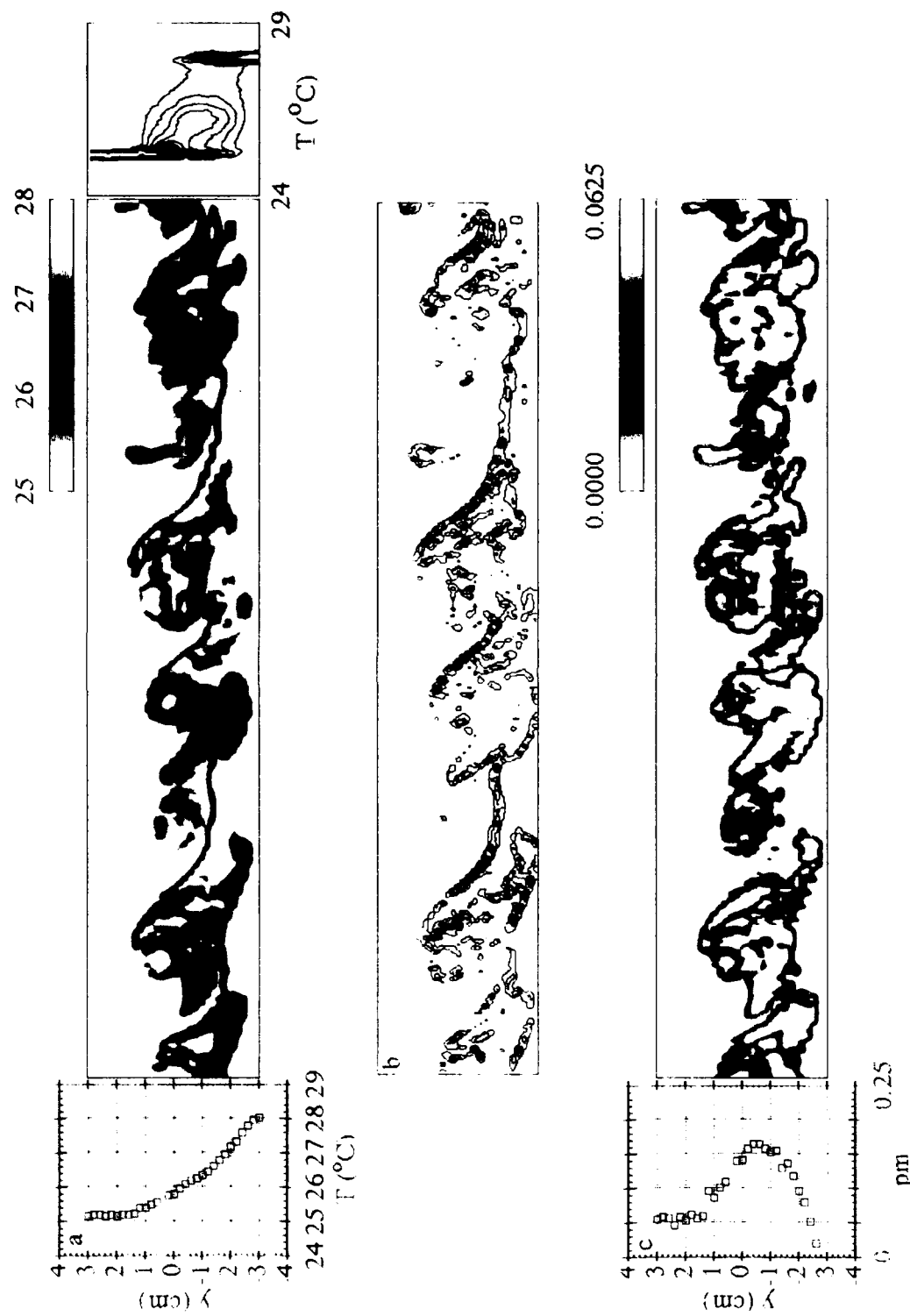


Figure I.19. (a)  $T(y)$ ,  $T(y, t)$ , and  $pdf(T, y)$ ; (b)  $G(y, t)$ ; and (c)  $pm^2(y, t)$  for feedback configuration C3D<sub>3</sub> at  $x = 15.24$  cm.

We note that the shape of the temperature probability density functions for the various configurations (2D and 3D cases) suggest that there is no entrainment of irrotational fluid into the primary vortices by "nibbling". The rationale for this argument is based on the observation that the peak of *pdf* profiles at *y* elevations across the layer is virtually at the same temperature. Clearly, if there is a localized transport of irrotational fluid from either streams into the primary vortices through "nibbling", the peak of the *pdf* at *y* elevations near these boundaries would shift towards the temperature of the free stream. This is not the case in the present experiments and in the experiments of Koochesfahani and Dimotakis (1986). Thus, if it is argued that entrainment occurs by "engulfing" then the performance measure data suggest that at this streamwise station there is no unmixed fluid at either  $T_1$  or  $T_2$ , and hence that entrainment is reduced or inhibited. These arguments are consistent with the present observations and the observations of Roberts.

## **I.5. Open-loop results**

We have undertaken to investigate the effect of open-loop forcing on mixing in the plane shear layer in order to provide baseline data for comparison with the feedback configurations. The open-loop investigations are also of interest because there is a substantial body of work concerning mixing of unforced (Koochesfahani and Dimotakis 1986) and forced (Roberts and Roshko 1985) plane shear layers at high Schmidt numbers, while the present research is concerned with mixing of temperature at a low Prandtl number. In the present experiments the excitation is time harmonic. The excitation waveforms are spanwise-uniform (SU) and spanwise-periodic (SP) having a time-invariant amplitude and a spanwise wavelength of 2.66 cm. Three cases are reported below: SU and SP at  $f = 6$  Hz, and SP at a combination of  $f = 6$  and 3 Hz.

### *I.5.1 Instantaneous and time-averaged data*

The unforced flow is described in detail in §I.4.3. In figures I.20a-c ( $x = 10.16$ , 15.24, and 20.32 cm, respectively) the excitation waveform is SU ( $f = 6$ Hz). Similar to forcing with feedback configurations  $C_1$ ,  $C_2$ , and  $C_3$ , the present excitation configuration leads to mixing enhancement by promoting rollup of the primary vortices closer to the flow partition (figure I.20a) than in the unforced case.(figure I.8a). As a result of the forcing the primary vortices appear to be approximately regular in size and cross-stream position. While the passage frequency of these vortices is almost unchanged at  $x = 15.24$ , and 20.32 cm (figures I.20b and c). It appears that while at  $x = 20.32$  cm, there is some mixed fluid

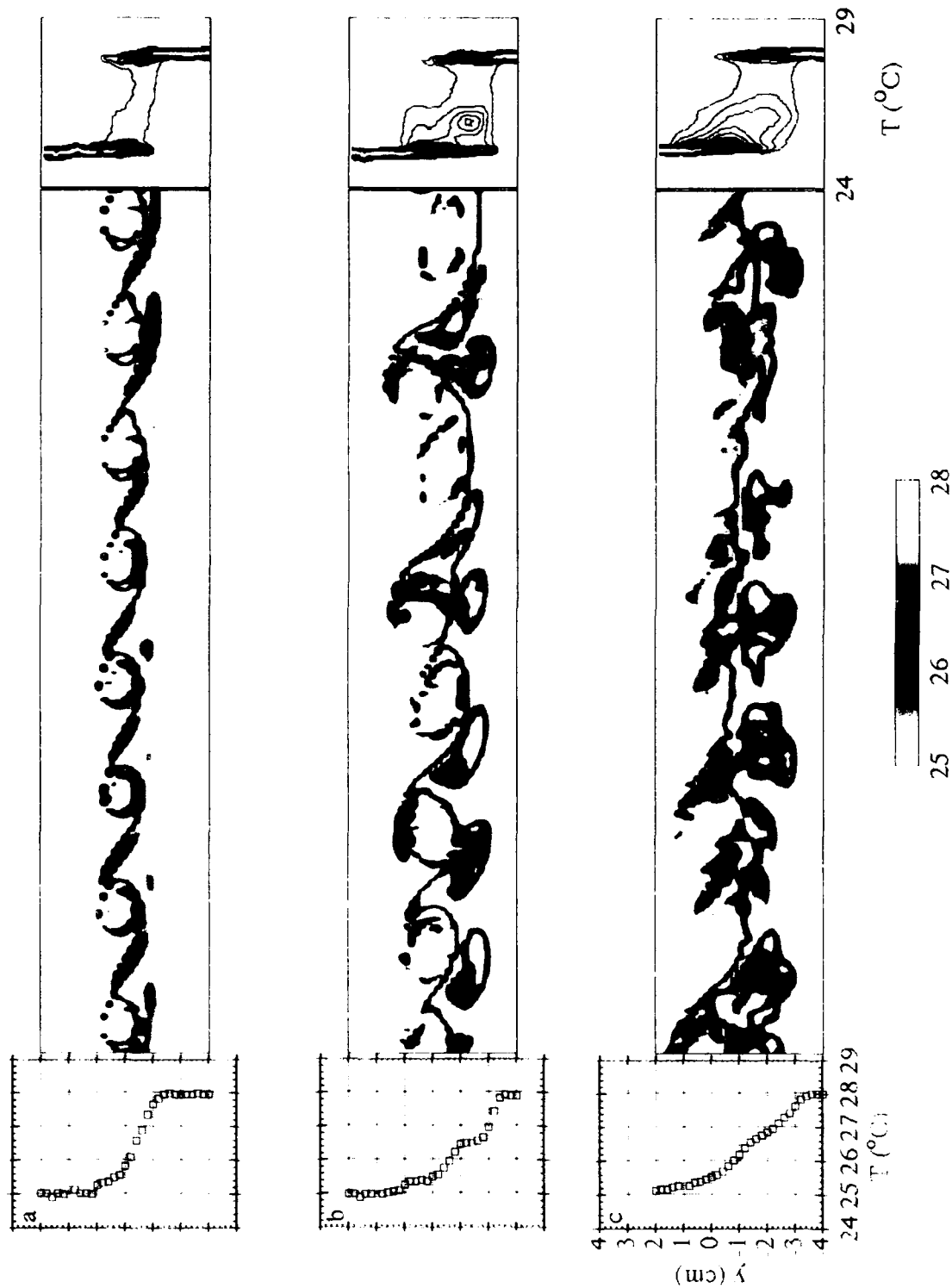


Figure 1.20.  $T(y)$ ,  $T(y, t)$ , and  $pdf(T, y)$  for SU,  $f = 6$  Hz at  $x =$ : (a) 10.16 cm; (b) 15.24 cm; and (c) 20.32 cm.

around the cores of the primary vortices, there are substantial patches of unmixed fluid within the cores. Contours of  $pdf(T,y)$  show that compared to the unforced case, time-harmonic excitation leads to mixing enhancement and broadening of the cross-stream domain in which mixing occurs (figure I.20c). We also note that contours of  $pdf(T,y)$  at  $x = 15.24$  cm show a peak at  $T = 25.9^\circ$  C. Similar peaks are also present in corresponding plots of  $pdf(T,y)$  for the feedback configurations (e.g., I.9b, I.10b and I.11b).

The effect of time harmonic spanwise nonuniform excitation is shown in figure I.21. As is the case for the feedback configurations, the triggering of streamwise vortices leads to the appearance of three-dimensional small-scale flow structures and mixing enhancement within the cores of the primary vortices. Contour plots of  $pdf(T,y)$  indicate a substantial increase in mixing compared to the spanwise-uniform case. Furthermore, the temperature peak at  $T = 26.1^\circ$  C which appears at  $x = 15.24$  cm is still present at  $x = 20.32$  cm, suggesting a change in the entrainment ratio compared to the SU case.

An increase in the width of the shear layer  $\delta$  can lead to an increase in the amount of mixed fluid within the layer. When the shear layer is simultaneously forced at a fundamental frequency ( $f = 6$  Hz) and its subharmonic ( $f = 3$  Hz), controlled pairing of the primary vortices is induced. The pairing process is accompanied by a concomitant increase in entrainment and  $\delta$ . Figure I.22 shows the effect of controlled pairing on the mixing in the presence of streamwise vortices. The temperature distribution  $T(y,t)$  shows that the primary vortices are beginning to pair at  $x = 10.16$  cm (figure I.22a) and the process continues through  $x = 15.24$  cm (figure I.22b) and is almost complete at  $x = 20.32$  cm (figure I.22c) where the passage frequency of the vortical structures is approximately 3 Hz. However, in contrast to forcing configuration SP  $f = 6$  Hz, where the fluid within the layer is almost entirely mixed in configuration SP  $f = 3, 6$  Hz there are large patches of unmixed fluid within the layer. Although it appears that at this streamwise station fluid is entrained more effectively when  $f = 3, 6$  Hz, not all the entrained fluid is mixed. Nonetheless, the contour map of  $pdf(y,T)$  at  $x = 20.32$  cm exhibit a peak at  $26.1^\circ$  C which is broader in the cross stream direction than the peak of the case  $f = 6$  Hz.

A plot of  $PM(x)$  is shown in figure I.23 for the forcing configurations discussed above. The unforced case has the lowest value of performance measure. Forcing program SU at  $f = 6$  Hz leads to an average increase of 25% at each streamwise station. The configuration SP at  $f = 6$  Hz, clearly leads to an additional increase in  $PM(x)$ , however, there is a streamwise domain ( $15 \text{ cm} < x < 19 \text{ cm}$ ) where  $dPM/dx$  decreases before it returns to its upstream value for  $x > 19$  cm. The configuration SP at  $f = 3, 6$  Hz leads to slightly less mixing than SP  $f = 6$  Hz ostensibly because not all of the entrained fluid is mixed. Although the feedback configurations discussed above were not selected to

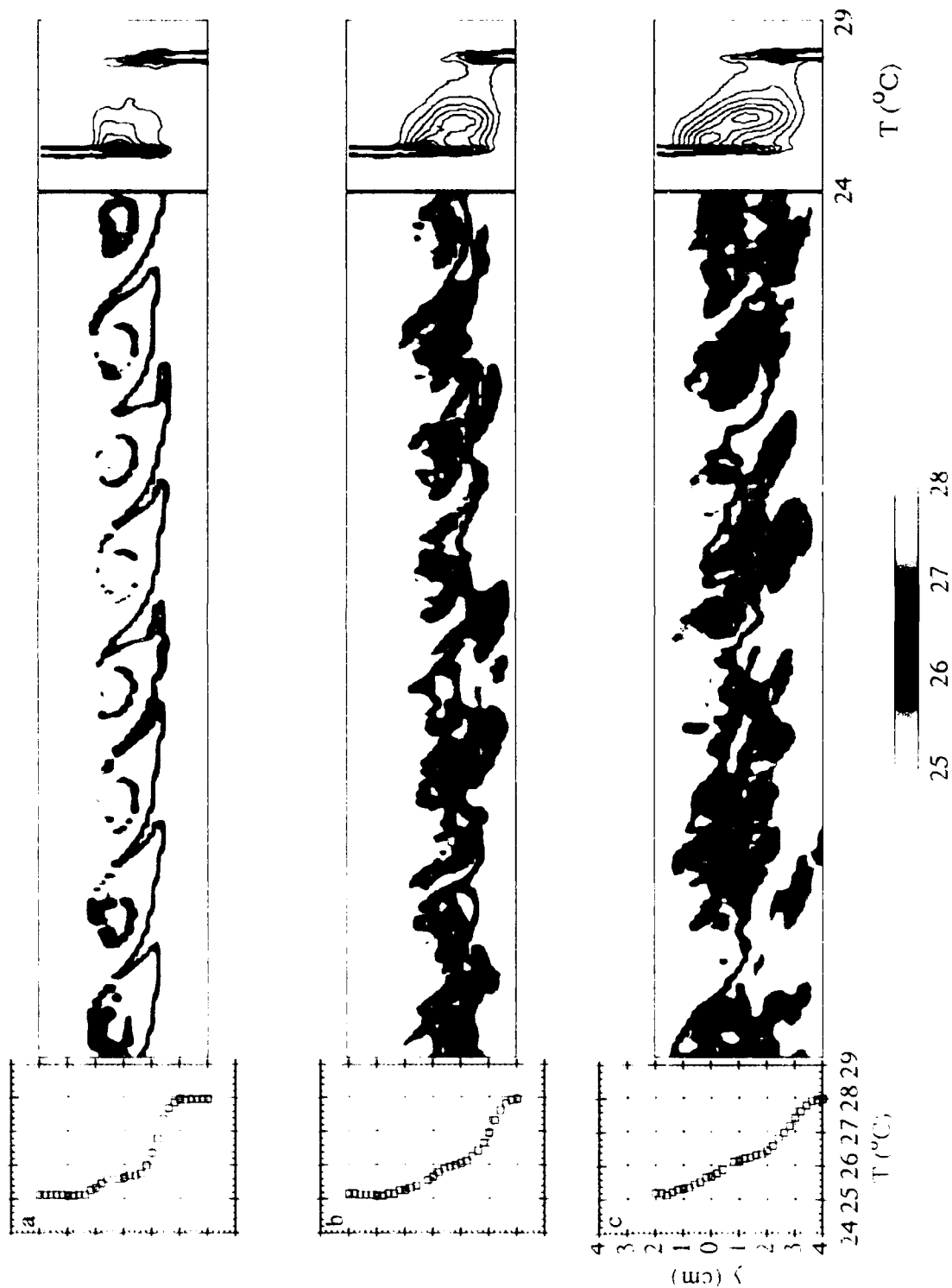


Figure 1.21.  $T(y, t)$ ,  $T(y, t)$ , and  $pdf(T, y)$  for SP,  $f = 6$  Hz at  $x =$ : (a) 10.16 cm; (b) 15.24 cm; and (c) 20.32 cm.

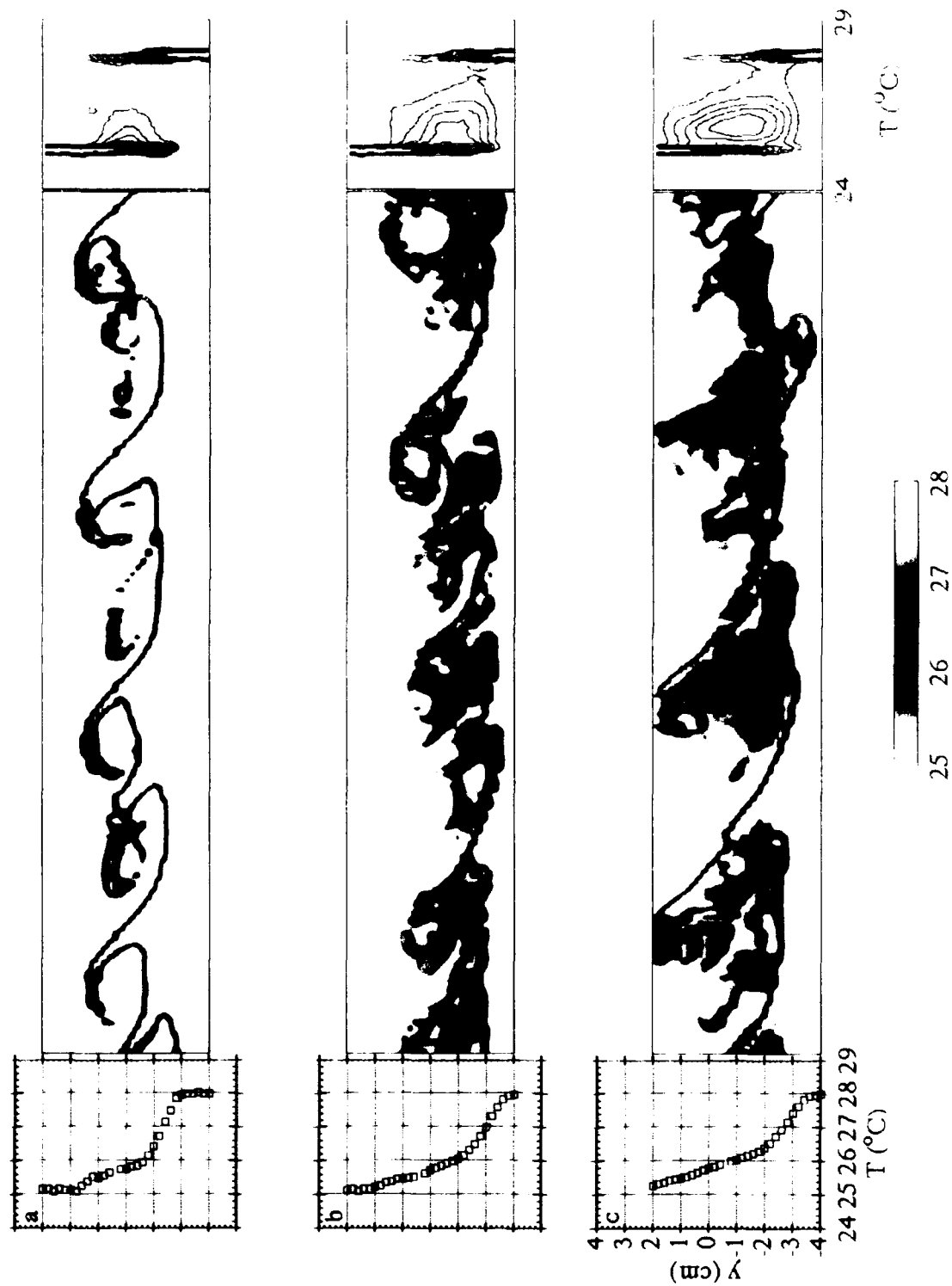


Figure I.22.  $T(y)$ ,  $T(y, t)$ , and  $pdf(T, y)$  for SP,  $f = 3$  Hz, 6 Hz at  $x =$  : (a) 10.16 cm; (b) 15.24 cm; and (c) 20.32 cm.



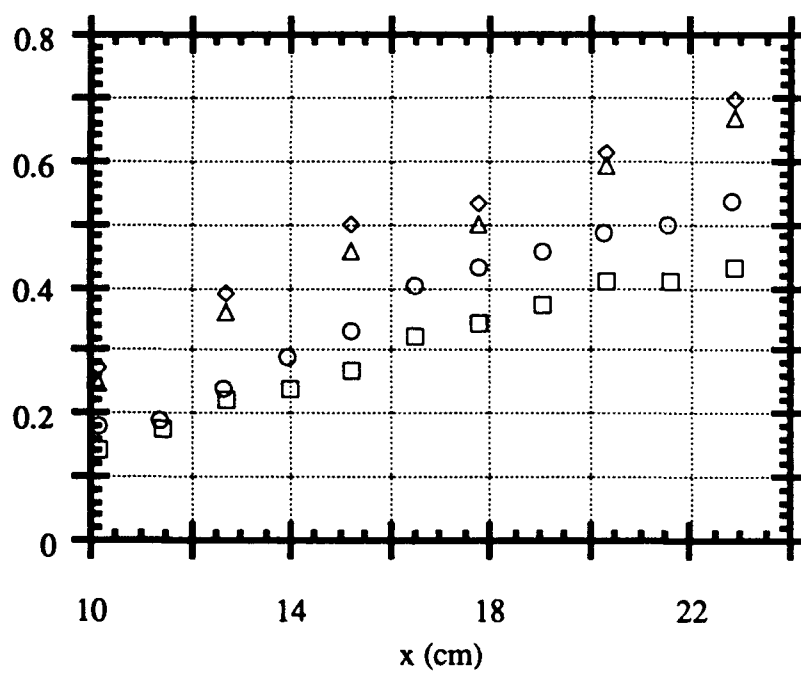


Figure I.23.  $PM(x)$  for unforced ( $\square$ ), SU,  $f = 6$  Hz ( $\circ$ ), SP,  $f = 6$  Hz ( $\diamond$ ), and SP,  $f = 3, 6$  Hz ( $\triangle$ ).

optimize mixing, we note that open-loop configuration SP  $f = 6$  Hz which leads to the largest levels of  $PM(x)$  has approximately the same effect on mixing as feedback configurations C3D<sub>1</sub> and C3D<sub>2</sub> (cf figure I.23 and figure I.17). Feedback configuration C3D<sub>3</sub> produces somewhat more mixed fluid than is attainable with any of the open-loop forcing configurations that are studied.

### *1.5.2 Phase averaged mixing*

Given the intermittent nature of the two-dimensional free shear layer, it is clear that mixing in this flow varies significantly with time. The present results demonstrate that most of the mixing occurs within the primary vortices. Because time harmonic forcing results in a streamwise domain within which the flow is phase locked to the forcing frequency, it is possible to utilize phase-locked measurements to obtain phase averaged mixing information which can be directly related to phase averaged temperature measurements and hence to topological features of the vortical structures. In what follows, we compare forcing configurations SU and SP at  $f = 6$  Hz. We note that in contrast to previous sections the input signal to all surface heaters in the present section is time harmonic (it was found that this method of excitation yields improved mixing)

Composites of four pairs (a-d) of raster plots of (phase averaged)  $\langle T(x,y,t) \rangle$  and  $\langle pm^2(x,y,t) \rangle$  for  $t/T_f = .0625, .3125, .5625$ , and  $.8125$ , respectively ( $T_f$  is the forcing period) are shown in figures I.24a-d and I.25a-d (forcing configurations SU and SP, respectively). We emphasize that the measurements for the SP configuration are taken at a spanwise station corresponding to the head of an ensuing streamwise vortex (Nygaard and Glezer). Each of the phase averaged plots is synthesized from phase-locked temperature data taken at 17 equally-spaced streamwise stations ( $5.08 \text{ cm} < x < 15.24 \text{ cm}$ ). The most prominent feature in figures I.24 and I.25 is that when the shear layer is forced with configuration SP its cross stream width is approximately 40% greater (at spanwise stations corresponding to the head of the streamwise vortex) than when it is forced with configuration SU.

In the SU configuration, mixing (as measured by the performance measure) first occurs in narrow bands near the perimeter of the primary vortices. The mixing in these regions appears to be connected primarily with stretching of temperature interfaces (figure I.24a-c). As the rollup progresses, two larger (red) concentrations (or patches) of mixed fluid appear near the high-and low-speed edges of the primary vortex. We believe that the flow undergoes mixing transition when these patches spread towards the centers of the primary vortices ( $x > 13 \text{ cm}$ ) as can be observed on the right hand (downstream) edge of

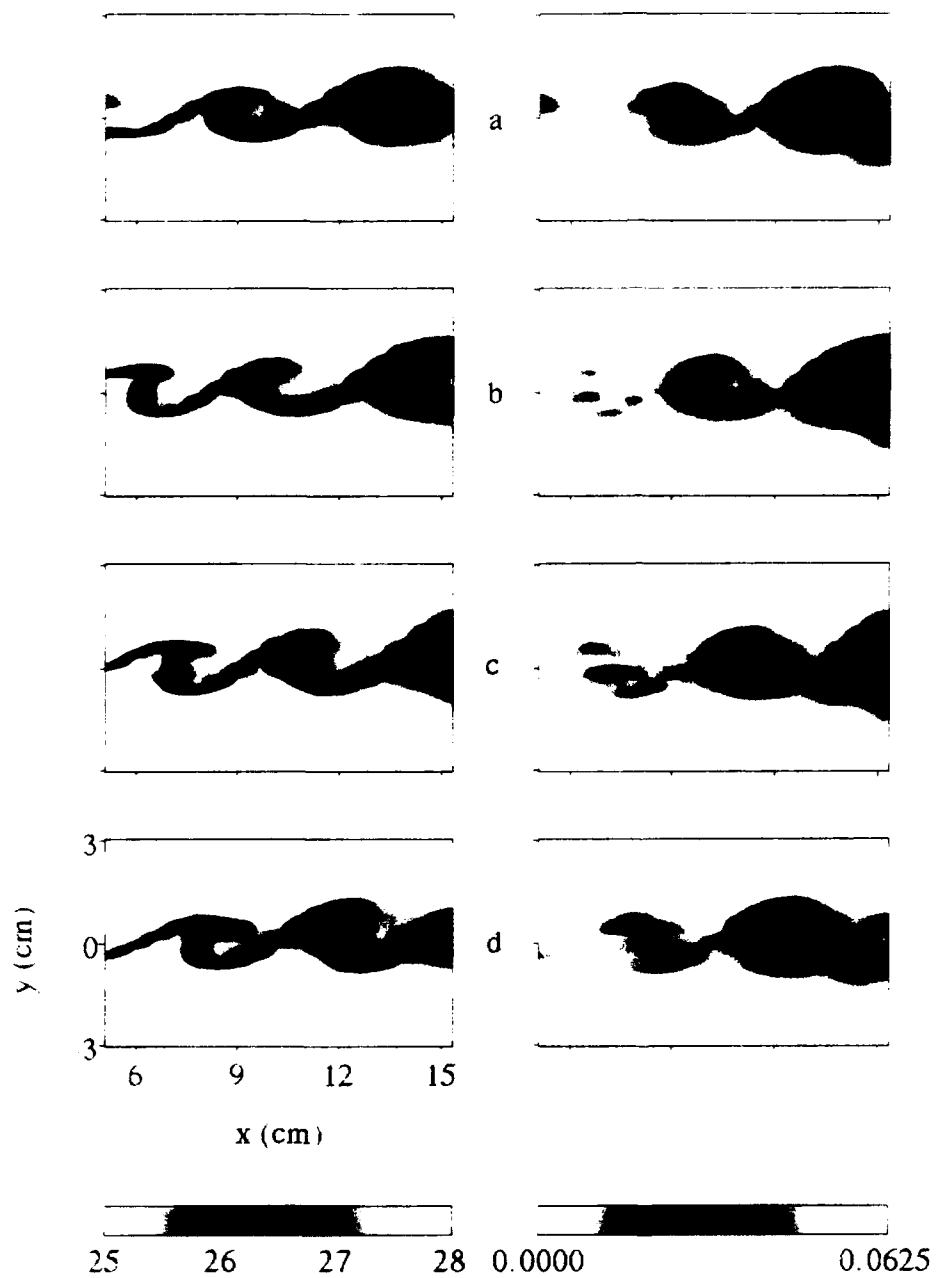


Figure I.24.  $\langle T(x,y,t) \rangle$  and  $\langle pm^2(x,y,t) \rangle$  for SU,  $f = 6$  Hz at times  $t/T_f =$  : (a) 0.0625; (b) 0.3125; (c) 0.5625; and (d) 0.8125.

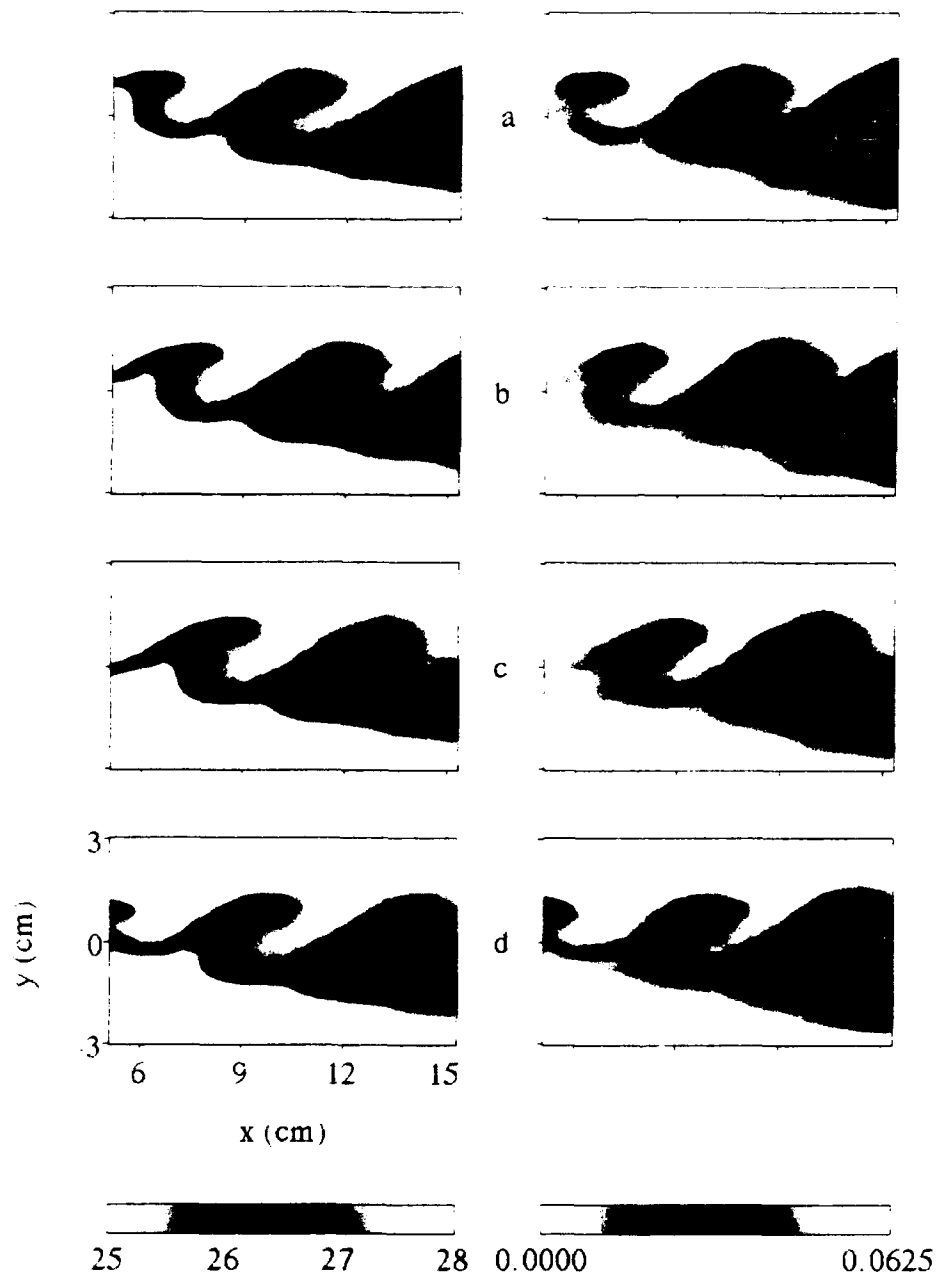


Figure I.25.  $\langle T(x,y,t) \rangle$  and  $\langle \mathbf{p} \mathbf{m}^2(x,y,t) \rangle$  for SP,  $f = 6 \text{ Hz}$  at times  $t/T_f =$  : (a) 0.0625; (b) 0.3125; (c) 0.5625; and (d) 0.8125.

the performance measure plots. This spreading of mixing within the cores of the primary vortices is presumably the result of (unforced) three-dimensional motions. As was shown by Nygaard and Glezer, the streamwise vortices reside on the high- and low-speed edges of the primary vortices, where the induced small scale motions first appear. The small scale motions then propagate towards the centers of the primary vortices and lead to mixing transition. When the flow is subjected to forcing configuration SP (figure I.25a-d), mixing occurs more rapidly. The performance measure plots show a concentration of mixed fluid near the high-speed side which is where the head of the streamwise vortex first forms. This concentration corresponds to fluid at temperature which is closer to that of the cold stream. The cross-stream domain of mixing increases substantially within a short streamwise distance ( $x \approx 10$  cm), and the mixed temperature is closer to the mean temperature indicating the presence of low-speed fluid.

The probability density function of temperature can be calculated for configurations the SU and SP as a function of phase at a given streamwise station. Figures I.26a-d and I.27a-d show  $\langle pdf(T, y, t) \rangle$  at  $x = 15.24$  cm for  $t/T_f = .0625, .3125, .5625$ , and  $.8125$ , respectively. Raster plots of two cycles of the phase-averaged temperature  $\langle T(y, t) \rangle$  are shown for reference. Times corresponding to contour plots of  $\langle pdf(T, y, t) \rangle$  are indicated by a dark line at the center of each frame of  $\langle T(y, t) \rangle$ . For the SU configuration, the mixing is clearly confined to a narrow region within the primary vortex (e.g., compare  $t/T_f = .5625$  to  $t/T_f = .0625$ ). In the SP configuration the effect of the head of the streamwise vortex is visible in figure I.27a. Another important feature is the amount of mixing in figure I.27d which corresponds to the braids region between primary vortices. This is mixing which is presumably induced by the legs of the streamwise vortex.

## I.6 Variation of PM with $\underline{k}$

We have recently begun to study the dependence of **PM** on the feedback gain  $\underline{k}$ . In what follows, we discuss a preliminary result concerning the variation of mixing when the control input is spanwise-uniform. In particular we consider the case  $\mathbf{PM} = \mathbf{PM}(r, \theta)$  where  $r = |\underline{k}| = (k_1^2 + k_2^2)^{1/2}$  and  $\theta = \arctan(k_2/k_1)$  (figure 28a). For the case discussed below  $r = 1$ , and we note that the limitation on the magnitude of  $r$  is the safety limit of the surface film heaters. In figure 28b we show  $\mathbf{PM}(r = 1, \theta)$  measured at  $x = 15.24$  cm; also plotted for comparison are the levels of **PM** for the unforced case and for the case of spanwise-uniform time-harmonic excitation. *The most prominent feature of this plot is that depending on  $\theta$ , **PM** varies from a minimum slightly higher than SU at  $f = 6$  Hz (30% above the unforced level) to a maximum that is almost 50% above the unforced level.* This

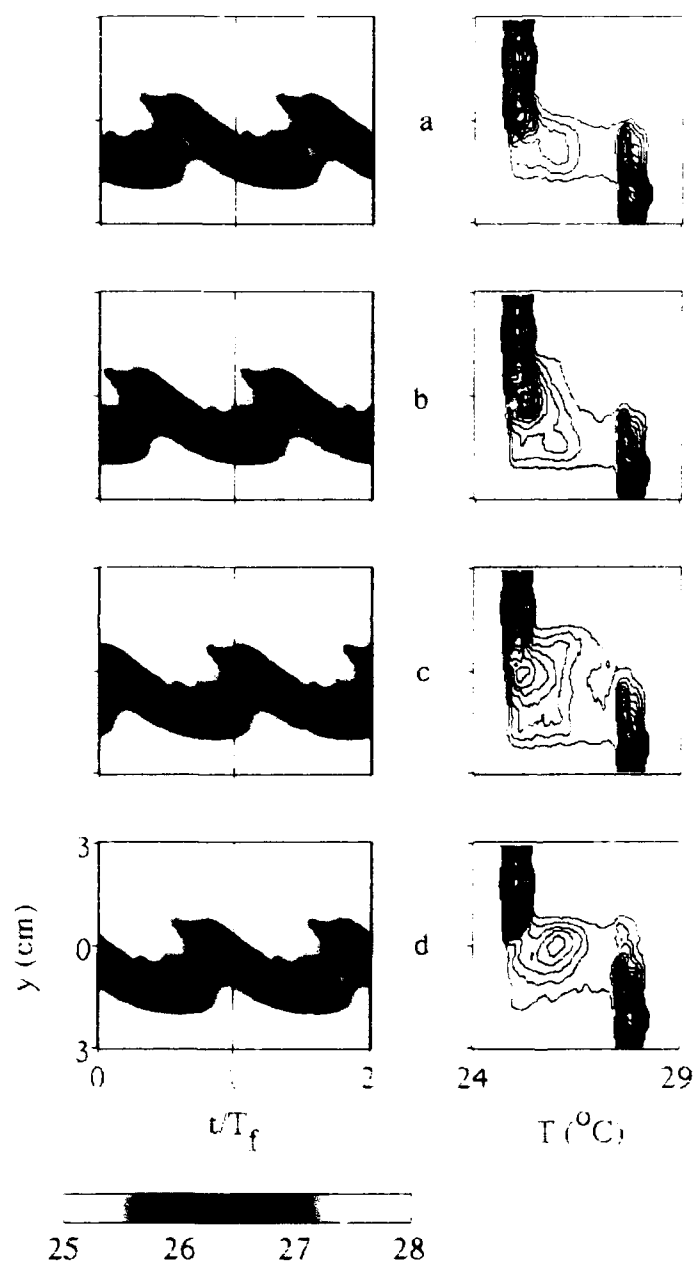
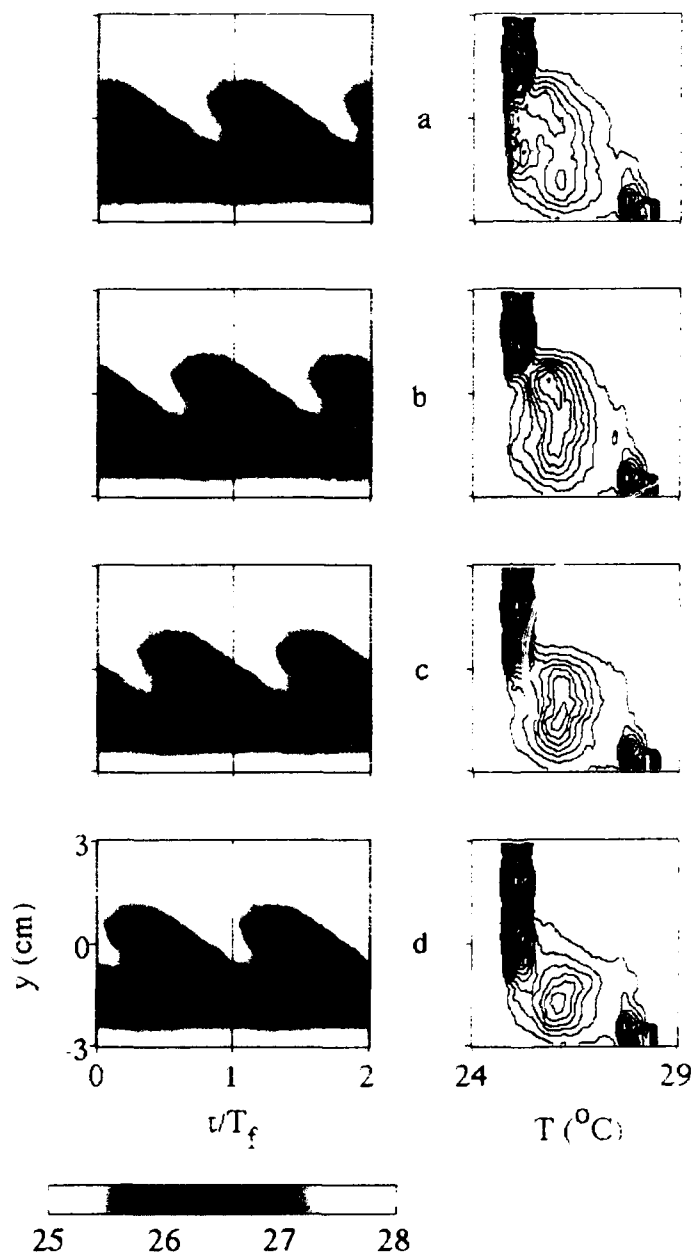


Figure I.26.  $\langle T(y,t) \rangle$  and  $\langle pdf(T,y,t) \rangle$  at  $x = 15.24$  cm for  $SU$ ,  $f = 6$  Hz at times  $t/T_f =$  : (a) .0625; (b) .3125; (c) .5625; and (d) .8125.



**Figure I.27.**  $\langle T(y,t) \rangle$  and  $\langle pdf(T,y,t) \rangle$  at  $x = 15.24$  cm for SP,  $f = 6$  Hz at times  $t/T_f =$  : (a) .0625; (b) .3125; (c) .5625; and (d) .8125.

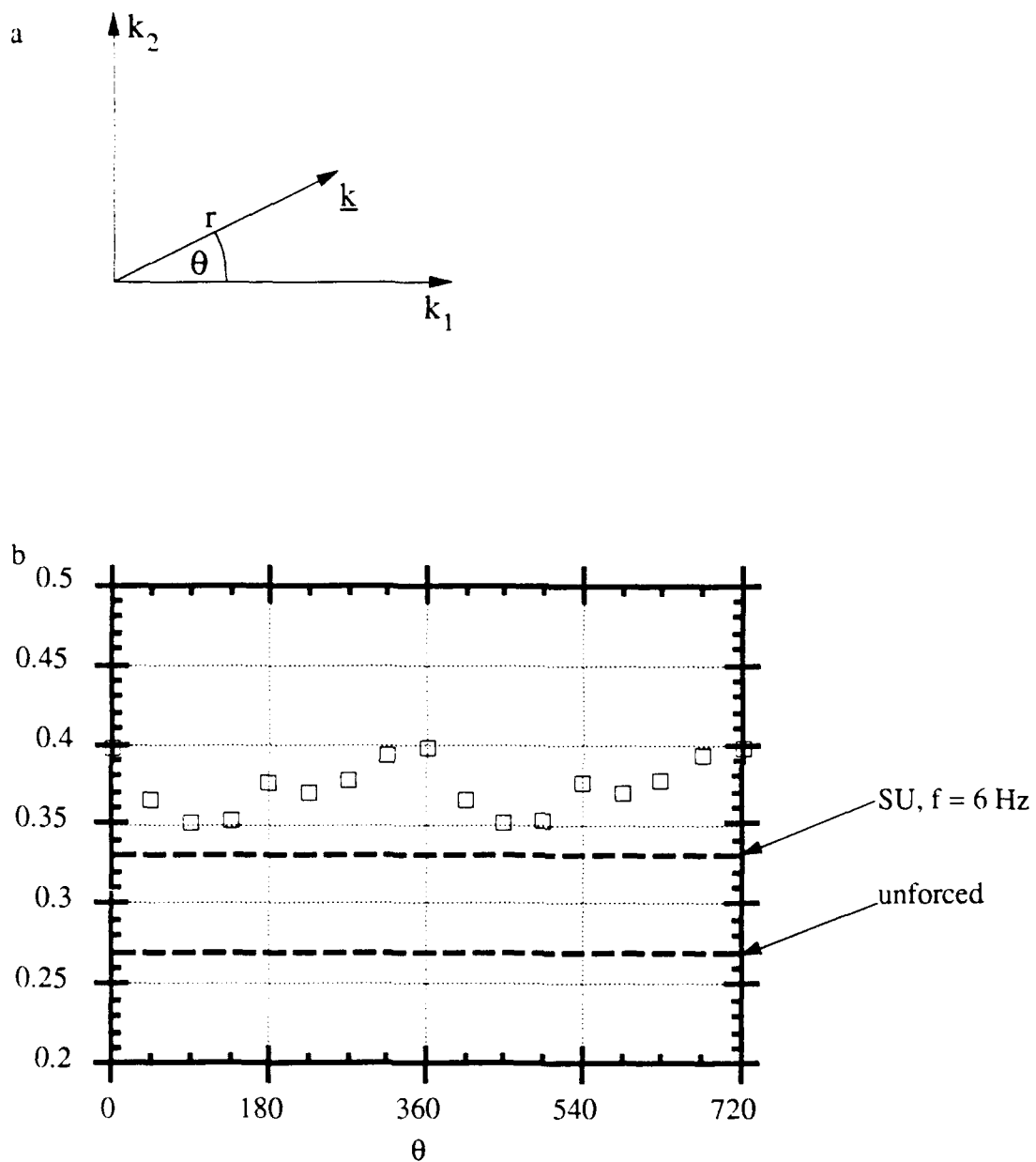


Figure 28. Dependence of **PM** on the angle of the gain vector  $\underline{k}$ : (a) geometry; and (b) **PM**( $\theta$ ), with **PM** for the unforced case and SU,  $f = 6$  Hz shown for comparison.



suggests that  $\theta$  (and  $r$ ) can be varied adaptively to optimize mixing at a given streamwise station. This and other features of the present controller will be investigated during the last year of the present grant.

## **I.7. Summary and outline of future research**

The present work is concerned with the development and implementation of feedback control systems for the enhancement and regulation of mixing in a plane shear layer. Our work focuses on a plane shear layer in which, far upstream of the flow partition, the high- and low-speed streams have uniform, steady temperatures differing by 3° C. Downstream of the flow partition, we sense and control the temperature distribution. Because we study mixing of a passive scalar in a nonreacting flow, we are able to conduct this experiment in a closed-return water facility.

Any feedback control system is comprised of three elements in addition to the plant: actuators, sensors, and a controller. We have chosen as actuators surface film heater flush-mounted on the high-speed side of the flow partition. The heaters are arranged in an array consisting of four spanwise-uniform and elements upstream of a 32-element spanwise row. The spanwise-uniform heaters provide the control authority for influencing the nominally two-dimensional rollup and entrainment in the shear layer. The 32-element spanwise nonuniform array provides the capability to introduce a high degree of three-dimensionality into the flow.

The sensors consist of a rake of 31 equally-spaced cold wire thermometers (for measuring the temperature distribution at various streamwise stations, and thus ascertaining the amount of mixed fluid) and an optical positions sensor (for measuring the location of the temperature interface of the two streams upstream of the first rollup of the primary vortices). All sensors are sampled virtually simultaneously by the laboratory computer.

A controller was developed in which the interface between the two streams of the plane mixing layer upstream of the first rollup of the primary vortices is modelled as a second-order system. By proper selection of the feedback gains, the poles of this system and the spectral response of the flow can be altered. The preliminary results presented above suggest that the feedback gains can be adjusted to beneficially enhance mixing. Three benchmark feedback configurations were studied. Although none of these configurations was specifically selected for mixing optimization, one configuration yielded mixing levels which were higher than attainable with open-loop time-harmonic excitation. The addition of spanwise nonuniform excitation led to the formation of small scale motions and to further improvement of mixing.

The following activities will be undertaken during the last year of the present grant:

- The dependence of the integral performance measure **PM** on the feedback gains  $\underline{k}$  with an optimized delay time  $\Delta$  will be mapped at a number of streamwise stations.
- The feedback gains  $\underline{k}$  will be adaptively modified in real time to optimize **PM** at a given streamwise station.
- Three-dimensional control inputs will be effected by spanwise-nonuniform distributions of the delay time  $\Delta(z)$  and the gain  $\underline{k}(z)$  to optimize **PM** at a given streamwise station.
- The temperature field  $T(y,z,t)$  will be measured at a number of streamwise stations for several spanwise-uniform and -nonuniform open-loop forcing configurations. Phase-averaged mixing will be mapped within the measurement domain with particular emphasis on the role of the streamwise vortices in the mixing process.

## Part II: MANIPULATION OF FREE SHEAR FLOWS USING PIEZOELECTRIC ACTUATORS

### II.1. Introduction

Suitable actuators having fast dynamic response and preferably low power consumption are the foundation of any scheme for the manipulation and control of flow instabilities. Most frequently, actuators have had mechanically moving parts, such as vibrating ribbons, movable flaps, or loudspeakers. Schubauer & Skramstad (1947) used a vibrating ribbon to excite Tollmein-Schlichting (T-S) waves across the span of a flat plate boundary layer. Oster & Wygnanski (1982) excited two-dimensional instability modes in a plane mixing layer using a small oscillating spanwise flap mounted at the trailing edge of the flow partition. Crow & Champagne (1971) studied the axisymmetric mode  $m = 0$  of a round jet using a plenum-mounted loudspeaker. A circular array of loudspeakers (Strange & Crighton 1983) and electromagnetic elements (Betzig 1981) placed around the perimeter of the jet nozzle have been used to excite azimuthal instability modes.

The shortcomings of the mechanical actuators described above have led to the development of two-dimensional mosaics of individually controlled surface-mounted heating elements (e.g., Liepmann, Brown & Nosenchuck 1982). Surface heaters typically have a high frequency response with no moving parts, can be easily mounted on nonplanar flow boundaries with relatively small intrusion to the flow, and can be used to output complex spatial/temporal excitation waveforms. Piezoelectric actuators have many of the attributes of surface heaters but require significantly less power. These actuators have been successfully employed in a number of experiments. Wehrmann (1967b) implemented a feedback controller in a flat plate boundary layer by using wall-mounted piezoelectric actuators to suppress naturally occurring T-S waves. Wehrmann (1965, 1967a) and Berger (1967) studied the wake of a piezoelectric cylinder having an oblong cross section. Time-harmonic forcing was obtained by either slight deformation of the cylinder's cross section (Wehrmann) or by spanwise-symmetric vertical bending of the cylinder along its axis (Berger). A feedback controller was used to synchronize vortex shedding to the excitation frequency. The authors also reported that vortex shedding could be suppressed at some Reynolds numbers.

The use of piezoelectric actuators for flow manipulation apparently has been limited because of the diminution in their response outside of a narrow frequency band around their resonance frequency. The present manuscript describes a new technique which

overcomes this difficulty and allows for effective manipulation of turbulent shear flows over a broad frequency range.

The utility of this technique has been demonstrated in a square air jet. A noncircular geometry was chosen because of its importance to technological applications in combustion (e.g., Gutmark, Schadow, Parr, Hanson-Parr & Wilson 1989b). The interest in noncircular jets for mixing and combustion applications stems from the fact that these jets typically entrain more ambient fluid than round jets having the same exit area and linear momentum flux [e.g., elliptic jets (Ho & Gutmark 1987) and square jets (Quinn & Militzer 1988)]. Furthermore, the presence of sharp corners in the nozzles of reacting jets leads to the appearance of azimuthal concentrations of small-scale motions within the ensuing vortical structures, with considerable enhancement of mixing and reaction of the chemical species (Gutmark et al. 1989b). Similar to plane mixing layers (Nygaard & Glezer 1991), these small-scale motions may be associated with the appearance of secondary streamwise vortices owing to azimuthal variations in the curvature of the primary (vortex ring-like) structures induced by the nozzle geometry.

In the present Progress Report we describe the excitation of an air jet emanating from a square conduit using four individually controlled piezoelectric actuators placed along the sides of the square exit. A description of the air jet facility in which the research was conducted is given in the next section. The excitation technique, the experimental results, and concluding remarks are presented in §II.3, II.4, and II.5, respectively.

## II.2. Experimental apparatus and procedure

### *II.2.1. The air jet facility*

The air jet facility is shown in figure II.1. The jet is driven by an axial blower (325 cfm) powered by a DC motor. Jet velocities up to 8 m/sec can be realized. The blower is equipped with heating and cooling units (not shown), which allow for temperature control of the air jet. The blower is connected to a primary plenum equipped with a loudspeaker for excitation of axial instability modes in the jet column. The main part of the jet facility is constructed from several sections of Plexiglass tube, each 15.24 cm in diameter. The first two sections downstream of the plenum are fitted with screens, honeycomb, and foam material to eliminate swirl and reduce velocity fluctuations. The jet emanates from a 3.81-cm (1.5")-square aluminum conduit 57 cm long. The equivalent diameter (defined as the diameter of a round pipe having the same cross-sectional area) of the conduit is  $D_e = 4.34$  cm. The conduit is centrally mounted on the downstream endplate of the Plexiglass tube

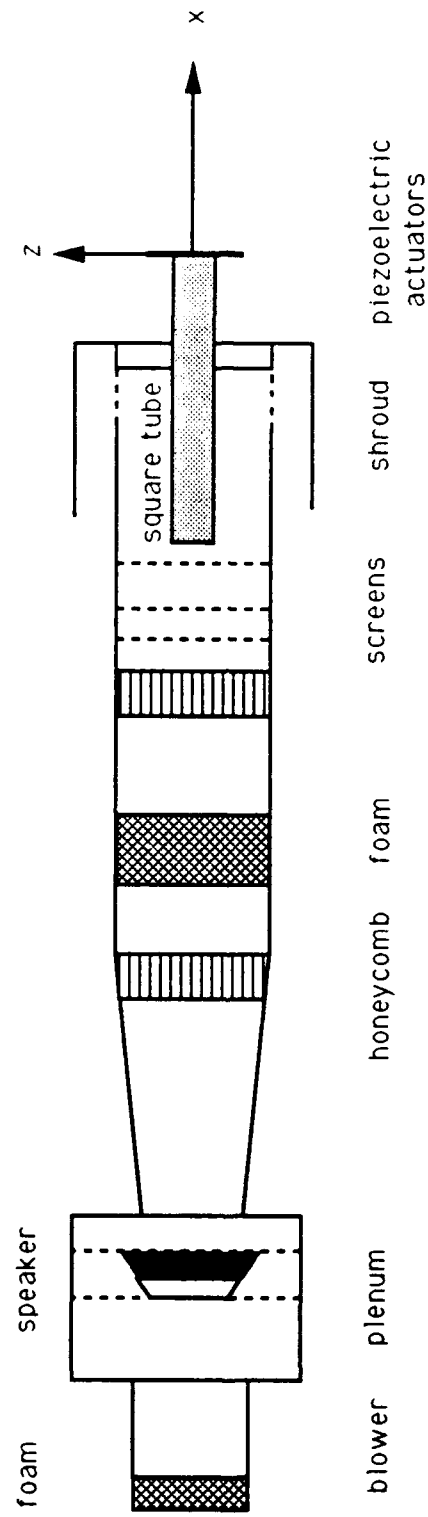


Figure II.1. The air jet facility.

and protrudes 35 cm in the upstream direction. The outer surfaces of the conduit are beveled near its upstream end. No contraction is used, and an azimuthally uniform gap along the perimeter of the front endplate is adjusted until the velocity distribution across the Plexiglass tube upstream of the inlet of the square conduit is approximately uniform. This geometry helps to minimize secondary flow at the inlet and along the corners of the square conduit.

The streamwise velocity component is measured with a single hot-wire probe mounted on a computer-controlled three-axis traversing mechanism. When the jet is forced, the measurements are taken phase-locked to the excitation signal. The measurements reported in the present manuscript are taken on a 16 by 16 square grid in the  $y$ - $z$  plane at four streamwise positions, corresponding to  $x/D_e = 1, 2, 3$ , and 4. The spacing between adjacent grid points increases linearly with downstream distance to compensate for the spreading of the jet, and the width of the grid,  $w_{y-z}(x)$ , increases from 4.85 cm at  $x/D_e = 1$  to 6.8 cm at  $x/D_e = 4$ . The lowest velocity of the unforced jet around the outer edges of the grid is approximately  $0.1 U_e$  ( $U_e$  is the jet centerline velocity at  $x = 0$ ). A Masscomp laboratory computer system is dedicated to experiment control and data acquisition. A double-pass Schlieren system is used to visualize the flow when the jet fluid is heated  $11^\circ\text{C}$  above the ambient temperature. The Schlieren view is in the  $x$ - $z$  plane and consists of a 15.2-cm-diameter circle centered at  $x/D_e = 1.75$  and  $z = 0$ .

### *II.2.2. Experimental conditions*

In the present experiments, the time-averaged jet centerline velocity at  $x = 0$  is  $U_e = 4$  m/sec, the Reynolds number based on  $D_e$  and  $U_e$  is 11,000, and  $\hat{u}'_l/U_e = 0.012$  at the center of the jet exit, where  $u'_l(x)$  is the time-averaged rms velocity fluctuations. We note that in the present manuscript time series of turbulent fluctuations of the streamwise velocity component  $\hat{u}'_l(x, t)$  are calculated from instantaneous velocity records (Glezer, Katz & Wygnanski 1989). This technique uses a digital high-pass filter and is extremely effective in discriminating between small-scale streamwise motions and spurious contributions from low-frequency variations of the flow relative to its mean. Profiles of  $U(x)$  and  $\hat{u}'_l$  measured at  $x = 1.08$  cm ( $x/D_e = 0.25$ ) are shown in figures II.2a and b, respectively. These profiles are measured along  $z = 0$  and along  $z = y$  (hereinafter referred to as the wall bisector and the corner bisector of the square conduit, respectively). The symmetry of these profiles with respect to the jet centerline ( $x$  axis) is indicative of the symmetry of corresponding profiles of the flow within the square conduit.

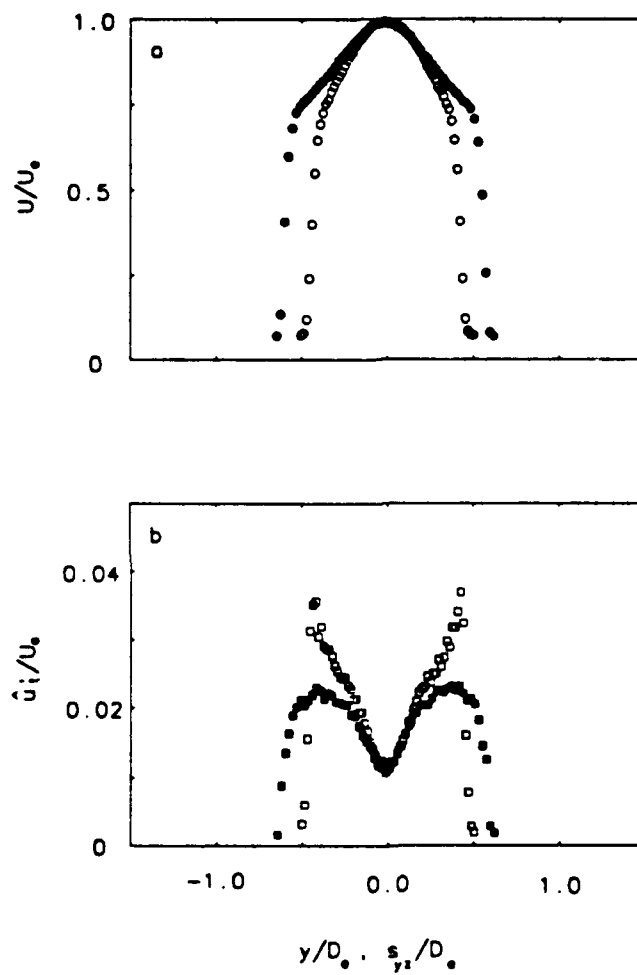


Figure II.2. Profiles of  $U/U_e$  (a) and  $u'/U_e$  (b) measured at  $x/D_e = 0.25$  along  $z = 0$  [ $\circ$  and  $\square$ ] and  $z = y$  [ $\bullet$  and  $\blacksquare$ ].

Figures II.3(a-d) show pairs of contour plots of  $U/U_e$  and  $\hat{u}'/U_e$  (contour increments are 0.05 and 0.005, respectively) in the y-z planes at  $x/D_e = 1, 2, 3$ , and 4. The dashed lines denote the transverse extent of the jet exit (3.81 cm square). These contour plots demonstrate that the jet largely retains its initial squareness within the streamwise domain of the present measurements. Furthermore, the distributions of rms velocity fluctuations suggest that, at least for the unforced square jet, the nozzle corners (or secondary corner flow within the square duct) do not contribute to localized azimuthal enhancement of small-scale motion. Similar results were also reported by Gutmark et al. (1985) for a jet emanating from a square duct at a much higher Reynolds number ( $Re = 63000$ ).

### *II.2.3. Piezoelectric Actuators*

The jet is forced using four piezoelectric actuators placed along the sides of the square exit (figure II.4). Each actuator is a composite of a thin (0.013 cm) stainless steel blade 3.81 cm wide and 3 cm long that is partially sandwiched along its width between two rectangular overlapping plates of piezoelectric ceramic (each measuring 3.8 cm x 1.9 cm x 0.018 cm). The composite end of each actuator is rigidly fixed along its width so that approximately 80% of its length is cantilevered. When an electric field is applied across the two outer electrodes of the actuator (and normal to the axis of polarization), the actuator bends about its fixed end. The magnitude and direction of the displacement of the free end depends on the magnitude and polarity of the applied voltage. The direction of tip displacement reverses with the polarity of the applied voltage. The largest tip displacement is achieved when the actuator is driven with a time-harmonic voltage at a resonant frequency,  $\nu_f$ , which depends primarily on the resonance characteristics of the piezoelectric plates and their cantilevered length, the thickness and length of the stainless steel blade, and the rigidity of the actuator mounting.

In the present experiments, four piezoelectric actuators are placed along the sides of the square exit in the plane  $x/D_e = 0.11$  so that the tip of each blade is aligned with the respective inner surface of the square conduit. The actuators have virtually no effect on the flow when they are not in use. The resonant frequencies of the actuators are not identical and vary within  $500 \pm 20$  Hz. The motion of the actuators (maximum peak-to-peak displacement of approximately 1 mm at resonance) is parallel to the jet axis.



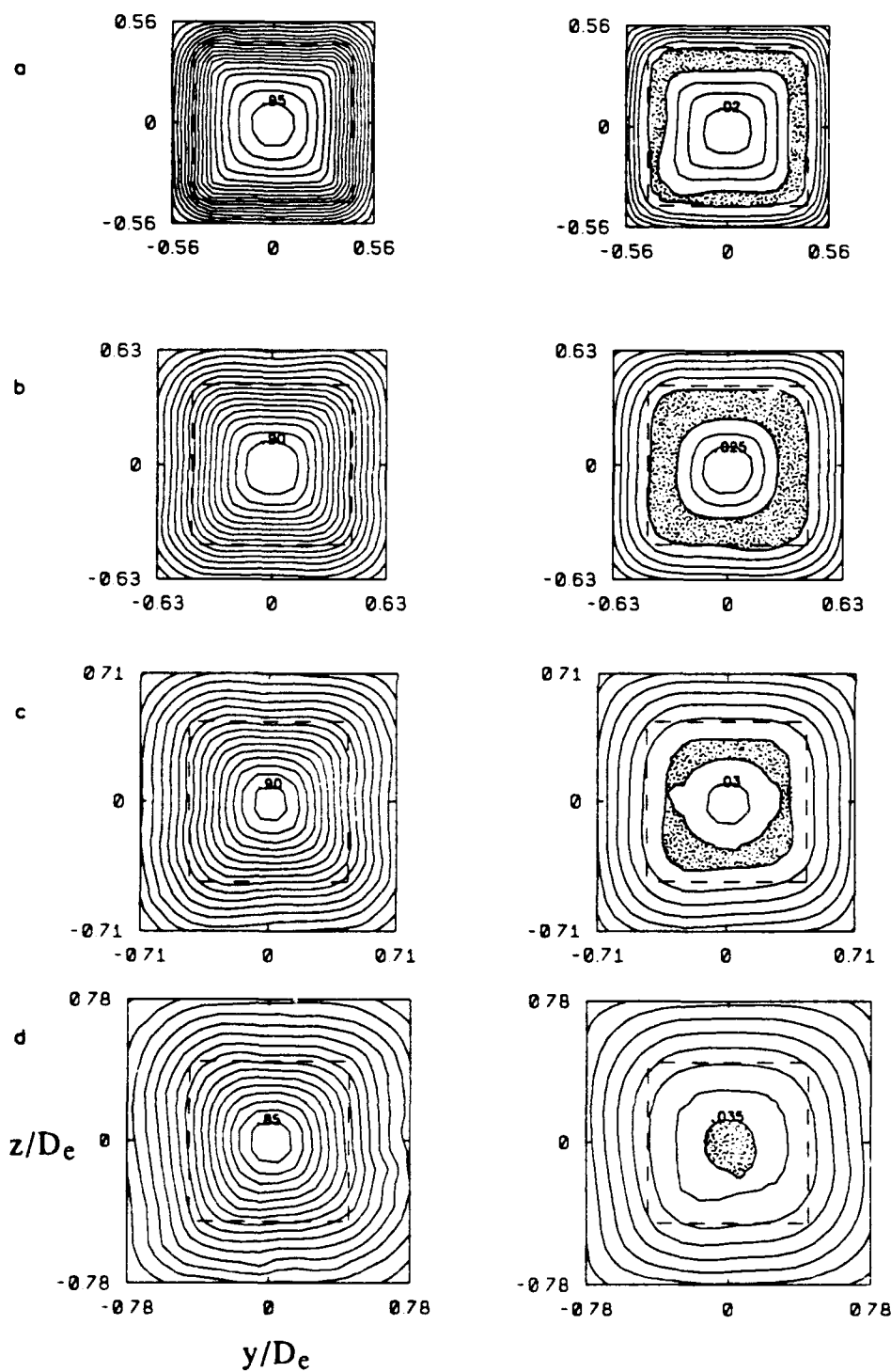


Figure II.3. Contour plots of  $U(y,z)/U_e$  [left] and  $\hat{u}'_t(y,z)/U_e$  [right] measured at  $x/D_e = 1$  (a),  $2$  (b),  $3$  (c) and  $4$  (d). Contour increments for  $U/U_e$  and  $\hat{u}'_t/U_e$  are  $0.05$  and  $0.005$ , respectively; maximum contour levels,  $c_{max}$ , are labeled. Regions where  $\hat{u}'_t/U_e > c_{max}$  are shaded. The dashed lines denote the extent of the jet exit.

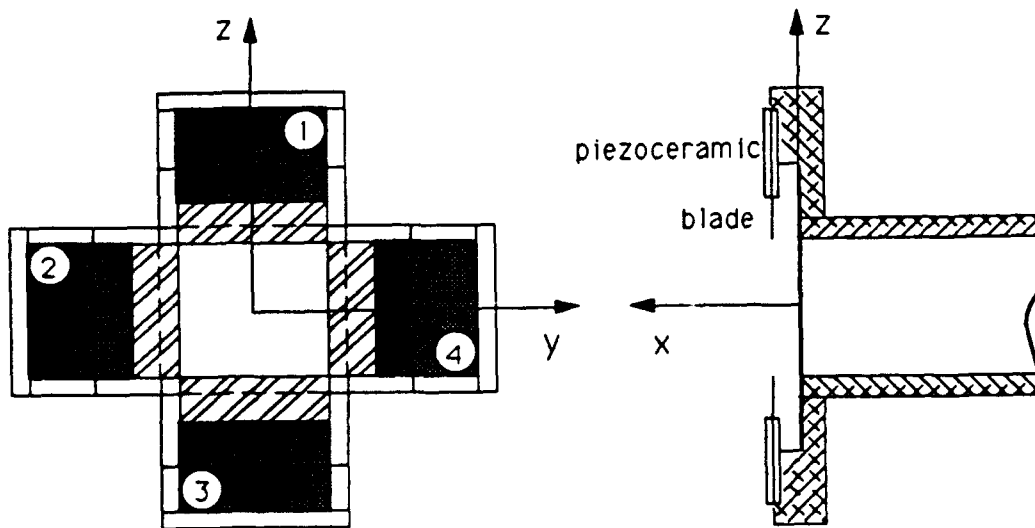


Figure II.4. Schematic diagram showing placement of actuators.

### II.3. Amplitude-modulated excitation

The limited utility of piezoelectric actuators outside a narrow frequency band around their resonance frequency can be overcome by implementing a new excitation technique in which the actuators are resonantly driven with a time-harmonic carrier wave train that is *amplitude modulated* with the desired excitation waveform. The resonant frequency of the piezoelectric actuators is selected to be well above the frequency band to which the flow is normally receptive. The premise is that, provided velocity perturbations induced by the actuators are large enough, the excitation waveform is effectively demodulated by exploiting flow nonlinearities. Because the flow is not receptive to excitation at the carrier frequency and its higher harmonics, these disturbances are attenuated downstream of the actuators while the modulating wave train is effectively amplified by the flow.

In the present experiments excitation is effected by the motion of the free ends of cantilevered actuators (§II.2) that induce streamwise velocity perturbations,  $u_{\text{pert}}(x, t)$ , in (nominally plane) segments of the jet shear layer. Excitation is effected by resonantly driving each actuator with a carrier waveform,  $e^i(t) = 1, 2, 3, 4$ , which is amplitude modulated with a time-harmonic wave train,  $e_m^i(t)$ :

$$e_i(t) = e_m^i(t) A_r^i \sin(\omega_r^i t)$$

where

$$e_m^i(t) = [1 + \epsilon_i \sin(\omega_f^i t + \Phi_i)],$$

$A_r^i$  is the amplitude of the carrier signal,  $\epsilon_i$  is the degree of modulation ( $0 \leq \epsilon_i \leq 1$ ),  $\nu_f^i = \omega_f^i/2\pi$  is the modulating frequency (which is also the desired excitation frequency),  $\nu_r^i = \omega_r^i/2\pi$  is the carrier frequency (or the resonance frequency of the actuator), and  $\Phi_i$  is the phase of  $e_m^i(t)$  relative to a time-harmonic reference wave train at the modulating frequency. Each actuator is driven by a dedicated AM signal generator, and the modulating waveforms are generated by the laboratory computer via a D/A interface. We note that the actuators can also be driven with anharmonic modulating waveforms.

Since at resonance the streamwise displacement of the free end of the actuators (relative to the rest position) is proportional to  $e_i(t)$ , it follows that for  $\omega_f^i \ll \omega_r^i$ , the amplitude of the perturbation velocity at the free end of each actuator,  $u_p^i$ , is proportional to  $A_r^i \omega_r^i$ . Thus, substantial velocity perturbations can be achieved even if  $A_r^i$  is small but  $\omega_r^i$  is large. (The maximum amplitude of the perturbation velocity in the present experiments is

estimated to be 3 m/sec.) While the spectral components of  $u_p^i$  are limited to  $v_f^i$  and its two sidebands  $v_f^i \pm v_f^i$ , a quadratic nonlinearity in the flow can lead to spectral components at  $v_f^i$ ,  $2v_f^i$ ,  $2v_f^i$ ,  $2v_f^i \pm v_f^i$ , and  $2v_f^i \pm 2v_f^i$ . Because the flow is not receptive to excitation at  $v_f^i$  and its higher harmonics, these frequencies should be rapidly attenuated with downstream distance.

Figures II.5(a-d) show power spectra,  $S(v)$ , obtained from hot-wire measurement of streamwise velocity in the jet shear layer at  $y = 0$ ,  $z = 1.91$  cm (the elevation of the free end of actuator 1), at two streamwise stations  $x/D_e = 0.23$  (figures II.5a-c) and  $x/D_e = 1$  (figure II.5d). A power spectrum of the unforced jet is shown in figure II.5a for reference, and in figures II.5(b-d) the flow is forced with actuator 1. When  $\epsilon_1 = 0$ , the jet shear layer is forced at the carrier (resonance) frequency  $v_f^1 = 510$  Hz (figure II.5b), which is prominent in this otherwise featureless spectrum. While the power spectra in figures II.5a and b are similar at low frequencies, there is a small increase in spectral content above 70 Hz in figure II.5b, which indicates an increase in small-scale motions. The most striking feature in figure II.5c ( $v_f = 16$  Hz) is the presence of spectral components at the modulating frequency and its first harmonic, in addition to spectral components at the carrier frequency and its two sidebands (510 Hz, and  $510 \pm 16$  Hz, respectively). This power spectrum shows that the excitation waveform is, in fact, demodulated by the flow. (Power spectra of the excitation input measured by a microphone on the centerline of the square conduit at  $x/D_e = 0.11$  with no flow show only peaks at the carrier frequency and its two sidebands and contain no measurable power at the modulating frequency and its higher harmonics.) At  $x/D_e = 1$  (figure II.5d), the spectral components at the carrier frequency and its sidebands are absent, and the amplitude of the spectral component at 16 Hz is somewhat higher, which may be indicative of spatial amplification.

Schlieren photographs of the forced jet in the  $x$ - $z$  plane are shown in figures II.6(a-g). Each Schlieren view includes the exit plane of the jet (the flow is from left to right) and extends through  $x/D_e = 3.5$ . In order to demonstrate the effect of the actuators, the jet exit velocity is reduced to 2.75 m/sec ( $Re_{D_e} = 7700$ ). The unforced jet is shown for reference in figure II.6a, and it is noted that the jet shear layer becomes unstable at  $x/D_e > 1.75$ . The jet is separately forced using pairs of opposite actuators (1,3 in figures II.6b, d, and f; 2,4 in figures II.6c, e, and g) having identical time-harmonic modulating waveforms ( $v_f = 12$  Hz). During the excitation period,  $T_f$ , the flow is illuminated by a strobe, which is triggered at a phase delay relative to the zero crossings of the modulating waveform. The effect of excitation with pairs of opposite actuators is photographed at the same phase delay (figures II.5b-c, 8d-e, and 8f-g). Each pair of photographs can be thought of as phase-locked views in the  $x$ - $z$  and  $y$ - $z$  planes. Figures II.6(b-c), 8(d-e), and 8(f-g) are taken at  $t$

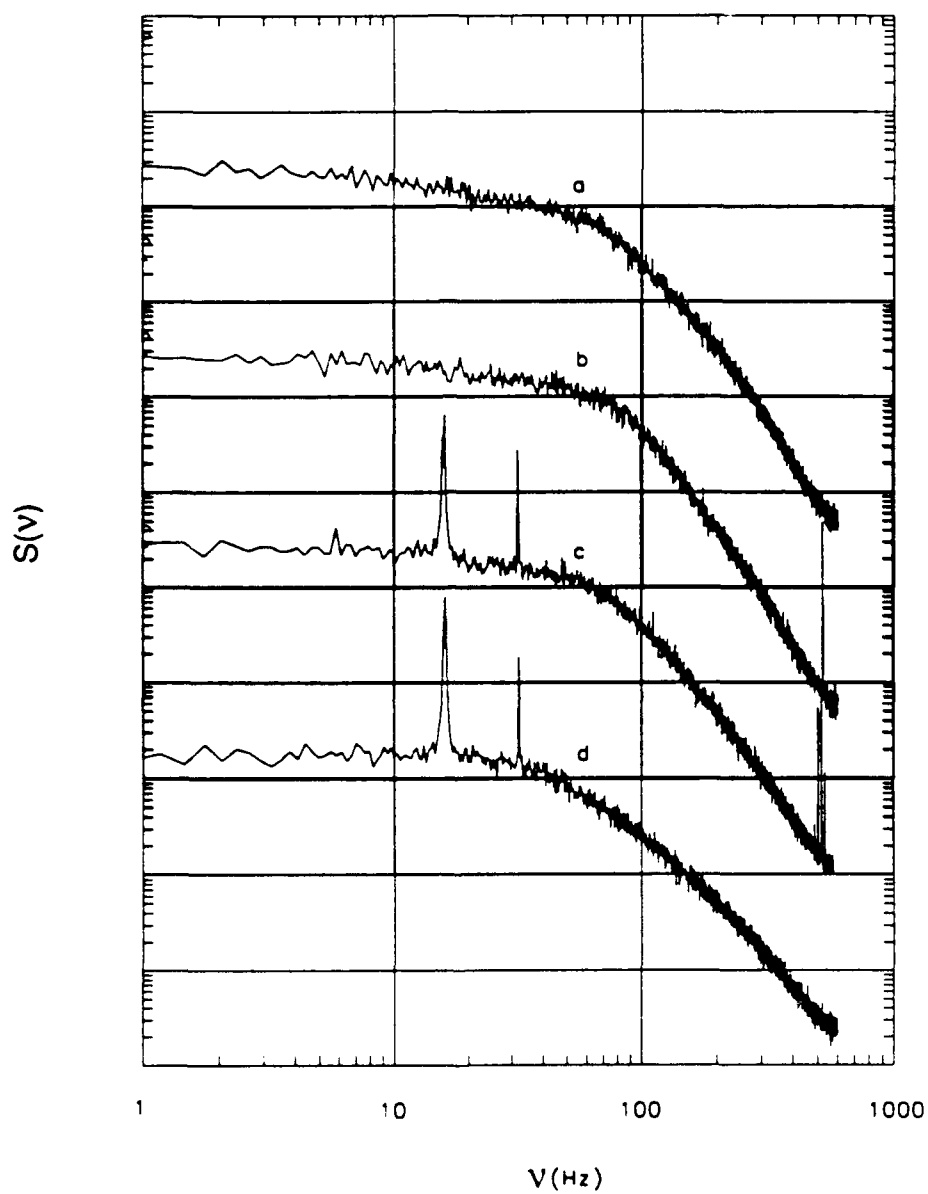


Figure II.5. Power spectra  $S(v)$  of the streamwise velocity at  $y = 0$ ,  $z = 1.91$  cm, and  $x/D_e$  0.23: (a) unforced; (b) forced using actuator 1 with unmodulated carrier [ $v_f^1 = 510$  Hz]; (c) as for (b) with amplitude modulation [ $v_f^1 = 16$ Hz]; (d) as for (c) at  $x/D_e = 4$ .

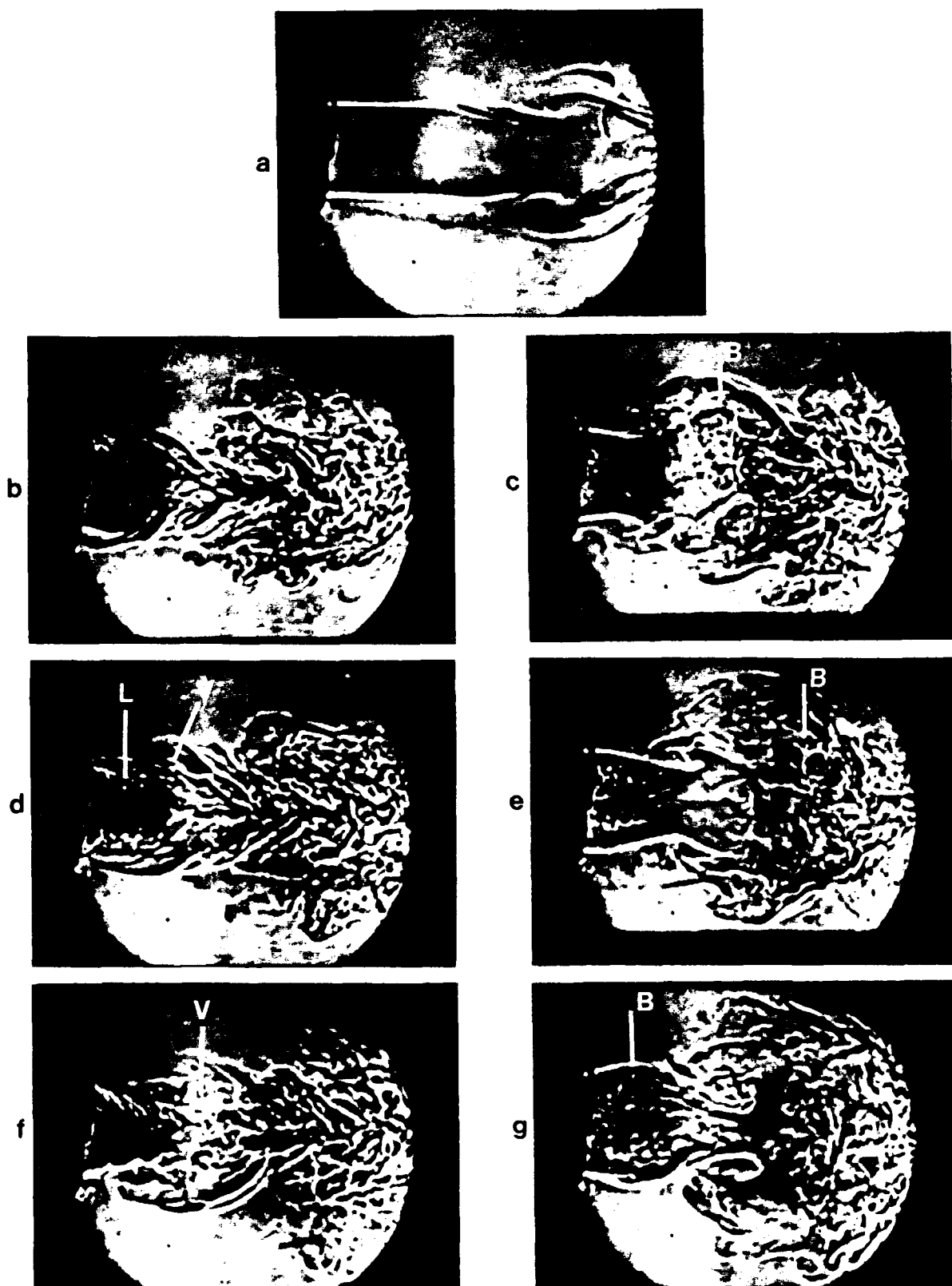


Figure II.6. Schlieren photographs in the x-z plane of the square jet [ $0 \leq x/D_e \leq 3.5$ ] unforced (a) and forced with amplitude-modulated carriers at  $\nu_f = 12$  Hz (b-g). The jet is forced separately with actuators 1,3 (b, d, f) and actuators 2,4 (c, e, g) and photographed at three time intervals during the excitation period:  $\tau = 0.03$  (b-c),  $0.25$  (d-e), and  $0.47$  (f-g).

= 0.03, 0.25, and 0.47, respectively ( $\tau = t/T_f$ , and  $\tau = 0.25$  roughly corresponds to the peak amplitude of the modulated carrier waveform).

A striking feature of figure II.6d is the formation of rows of locally two-dimensional line vortices (marked L in figure II.6d) with their axes parallel to the tips of actuators 1 and 3 (i.e., in the plane of figure II.6e). These vortices are formed at the carrier (resonance) frequency  $\nu_r$ , and their nominal cross-sectional dimension scales with the actuator displacement. Farther downstream from the nozzle, these vortices appear to roll into larger vortices (marked V in figures II.6d-e) at the modulating frequency  $\nu_f$ . The formation of these vortical structures, which apparently results from temporal modification of azimuthal vorticity in the jet shear layer by the actuators, suggests itself as the nonlinear mechanism necessary for the demodulation of the excitation wave train. For a given jet exit velocity, the rollup of vortices at the carrier frequency stops when the amplitude of the (modulated) excitation signal is below a given threshold (e.g., figure II.6b). Hence, it appears that if the velocity perturbations induced by the tips of the actuators are high enough, the high-frequency rollup within the jet shear layer may be the result of a localized (inviscid) inflectional instability.

Another important consequence of the excitation is the substantial broadening of the jet in the x-y view (figures II.6c, e, and f). This broadening is apparently the result of a marked increase in the cross-stream spreading rates of the forced segments of the jet shear layer as seen in the x-z plane (figures II.6d-e). (It should be emphasized that since only the jet fluid is heated, much of the outer flow is not visualized.) Significant changes in the cross-stream spreading rate of forced plane mixing layers has been observed by a number of investigators. In particular, Champagne, Pao & Wygnanski (1976) reported that the cross-stream spreading of a one-stream plane mixing layer increases when its upstream boundary layer is tripped with a spanwise wire. In a related experiment, Oster, Wygnanski & Fiedler (1977) noted that their trip wire did not produce a fully developed turbulent boundary layer but, in fact, induced measurable quasi-sinusoidal oscillations in the ensuing one-stream shear layer. Presumably the perturbations effected by the trip wire induced a premature rollup of the vortex sheet downstream of the flow partition, similar to the effect of the actuators in the present experiments. The coalescence of the high-frequency vortices into larger vortical structures when the excitation waveform is amplitude modulated may be similar to the formation of spanwise vortices in a plane shear layer that is excited at a much lower frequency than its "natural" rollup frequency.

Figure II.6f shows the substantial narrowing of the jet's core downstream of the exit plane when the excitation amplitude begins to drop below the level necessary for the formation of the line vortices. As a result of the appearance of these vortices, the jet

"bulges" in the x-y plane (marked B in figure II.6g). The "bulge" continues to spread as it is advected in the streamwise direction and, when  $\tau = 0.03$  in the next excitation cycle, it is located at  $x/D_e = 1.65$  (marked B in figure II.6c). Note the location and width of the "bulge" in figure II.6e during the rollup of the line vortices near the jet exit plane when  $\tau = 0.25$  (figure II.6e).

## II.4. Modification of the square jet

As discussed in §II.2 and II.3, excitation of the square jet is accomplished by amplitude modulation of the signals resonantly driving each of four piezoelectric actuators placed around the jet exit. In what follows the modulating waveforms are time harmonic and have the same frequency,  $\nu_f^i = 16$  Hz. The phase  $\Phi_i$  of each of the modulating waveforms is varied relative to a time-harmonic reference signal,  $e_{ref}(t)$  (having the same frequency), to produce four excitation programs: a)  $\Phi_i = 0$  ( $i = 1, 2, 3, 4$ ); b)  $\Phi_1 = \Phi_2 = 0$ ,  $\Phi_3 = \Phi_4 = \pi$ ; c)  $\Phi_1 = \Phi_3 = 0$ ,  $\Phi_2 = \Phi_4 = 0$ ; and d)  $\Phi_i = (i - 1)\pi/2$  ( $i = 1, 2, 3, 4$ ). We note that the phase relationships between the modulating waveforms for programs a, b, c, and d correspond (to lowest order) to azimuthal modes  $m = 0, \pm 1$ , and  $\pm 2$  and spinning mode  $m = -1$  of an axisymmetric jet. These programs will be hereinafter referred to as  $P_0$ ,  $P_{\pm 1}$ ,  $P_{\pm 2}$ , and  $P_{-1}$ , respectively.

### II.4.1. Distortion of the mean flow

The azimuthal distortion of the forced flow as a result of the excitation programs outlined above is shown in y-z contour plots of normalized mean streamwise velocity at  $x/D_e = 4$  (figures II.7a-f). Figure II.7a (unforced jet, also figure 3d) is included for reference. In figure II.7b, the jet is forced with unmodulated carrier signals (i.e.,  $\epsilon_i = 0$ ) each at the resonance frequency of the respective actuator. As noted in §II.3, although the carrier frequencies are present in velocity spectra measured near the actuators (cf. figure II.5b), the excitation amplitudes of the unmodulated input signals are chosen so that the mean flow is not distorted within the domain of measurements considered here. This excitation level is below the level necessary for rollup of the azimuthal line vortices within the jet shear layer. We note for reference below that excitation with unmodulated carrier signals of higher amplitudes can result in a distorted mean flow having essentially a featureless spectrum.

Excitation with  $P_0$  (figure II.7c) results in a mean flow that resembles a round jet (unforced square jets normally become round much farther downstream). In figure II.7d,



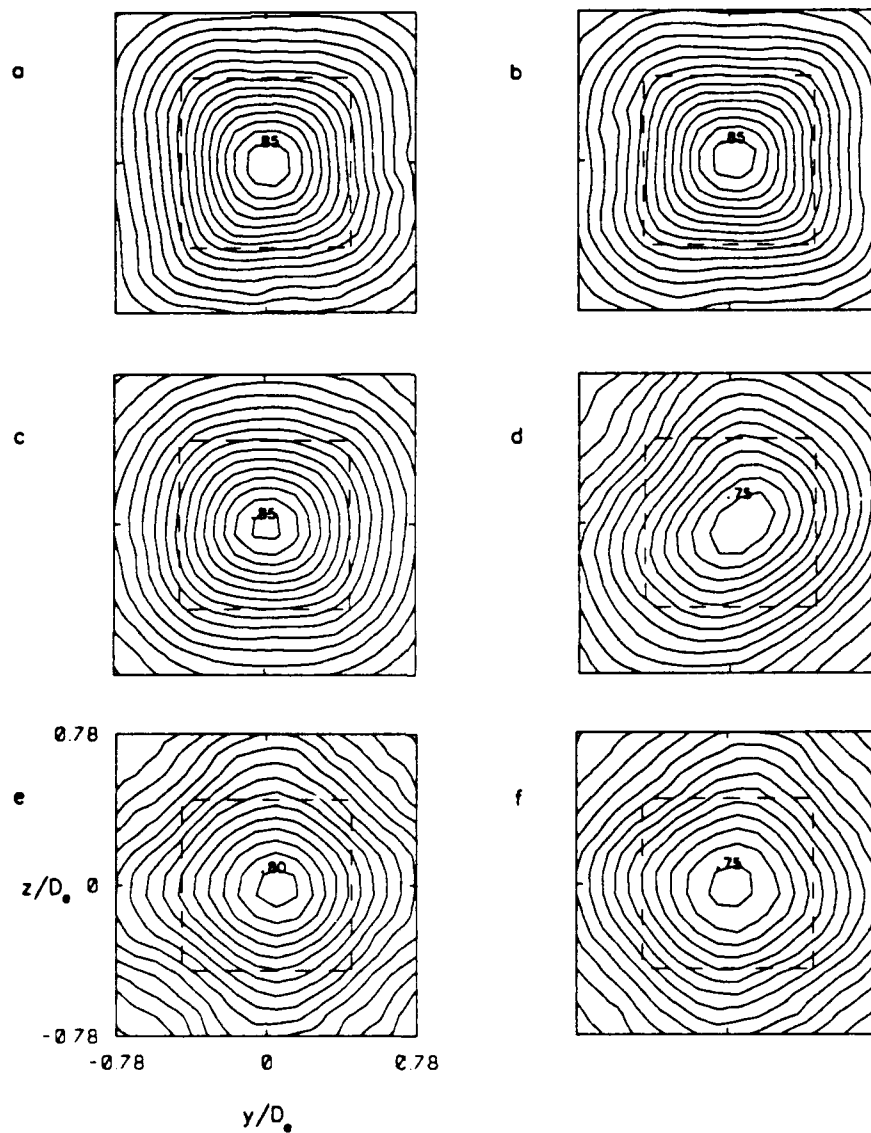


Figure II.7. Contours of  $U(y,z)/U_c$  measured at  $x/D_c = 4$ : (a) unforced; (b) forced with unmodulated carriers; (c) forced with  $P_0$ ; (d) forced with  $P_{\pm 1}$ ; (e) forced with  $P_{\pm 2}$ . Contour increments are 0.05, and the maximum contour levels are labelled.

the jet is forced with  $P_{\pm 1}$ . The jet's cross section becomes almost oval and is stretched along the corner bisector, which is the line of symmetry of the forcing. When the square jet is forced with  $P_{\pm 2}$ , its cross section has an approximate fourfold symmetry, where the  $y$  and  $z$  axes are the axes of symmetry (figure II.7e). The jet's cross section is almost equally stretched along each of these axes. Although it appears that when the jet is forced with  $P_{\pm 2}$  the distortion of the mean flow is approximately equivalent to a  $90^\circ$  rotation of the original square jet, measurements at  $x/D_e = 1, 2$ , and  $3$  do not show such rotation. In fact, the radial stretching of the mean cross section of the forced jet is the result of azimuthally nonuniform spreading of the jet shear layer. Finally, the result of forcing with  $P_{-1}$  is similar to a combination of forcing with  $P_0$  and  $P_{\pm 2}$  (figure II.7e). The jet appears to be rounded, as with  $P_0$ , yet there is some stretching, as with  $P_{\pm 2}$ .

We note in passing that interaction between two oppositely spinning modes having the same wave number and frequency in a round jet can lead to a triad resonance that distorts the mean flow with azimuthal periodicity of twice the mode number. For example, excitation of modes  $\pm 1$  results in  $\cos(2\phi)$  distortion (where  $\phi$  is the azimuthal coordinate) of the normally circular mean velocity contours and, similarly, excitation of modes  $\pm 2$  results in a  $\cos(4\phi)$  distortion of the mean velocity contours (Long & Petersen 1991).

The distortion of the jet due to excitation with carrier waveforms having azimuthally nonuniform amplitudes is shown in figures II.8a and b. Similar to figures II.7(a-f), figures II.8a and b are  $y$ - $z$  contour plots of the mean streamwise velocity at  $x/D_e = 4$ . In figure II.8a, the excitation waveforms are unmodulated, with the amplitudes of actuators 1 and 3 being twice the amplitudes of actuators 2 and 4 (i.e.,  $A_1 = A_3 = 2A_2 = 2A_4$ ). At this excitation level, the jet is highly distorted, with an apparent aspect ratio slightly in excess of two. We note that the excitation amplitudes of actuators 1 and 3 are above the threshold at which line vortices roll up at the carrier frequency within the forced azimuthal segments of the jet shear layer (cf. figure II.6d). Because the excitation leads to an increase in the cross-stream spreading of the jet shear layer, the jet cross section distorts and becomes rectangular compared to the cross section of the unforced jet in figure II.7a. The centerline velocity of the forced jet is  $0.75U_c$  compared to  $0.85U_c$  in the unforced jet.

Schlieren visualization suggests that in the absence of low-frequency modulation of the excitation waveforms, the line vortices in the forced azimuthal segments of the jet shear layer rapidly coalesce and lose their identity. In fact, spectra of the streamwise velocity measured on the jet centerline at  $x/D_e = 1$  (not shown) are essentially featureless. Hence, by driving the actuators with carrier signals of different amplitudes, the azimuthally nonuniform spreading of the jet shear layer can be exploited to provide a distorted mean base flow to which various low-frequency disturbances can be added by appropriate

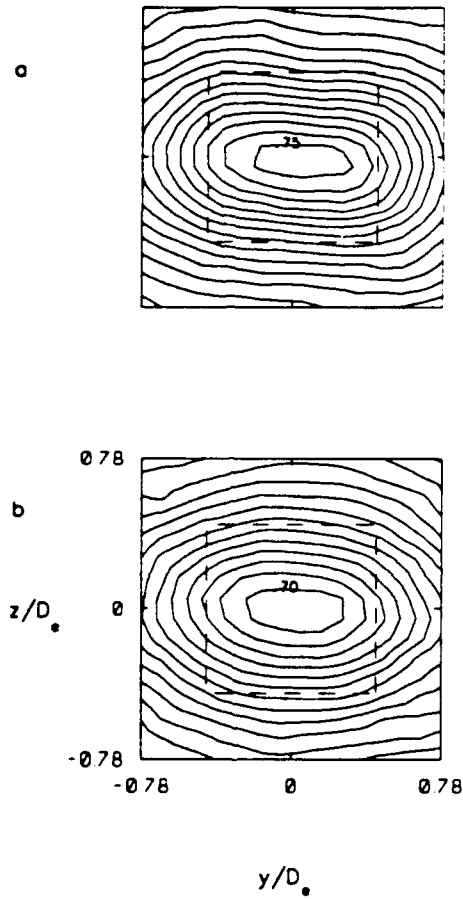


Figure II.8. As in figure II.7 except that  $A_r^1 = A_r^2 = 2A_r^3 = 2A_r^4$ : (a) unmodulated; (b) amplitude modulated with  $P_0$ .

amplitude modulation and phase selection of the modulating waveforms. In figure II.8b, the carrier waveforms of the actuators are amplitude modulated with  $P_0$  and the cross section of the jet becomes oval. This capability further suggests that proper selection of input waveforms can be used to tailor the mean velocity profile so as to provide favorable conditions for the introduction and propagation of desirable low-frequency disturbances.

#### *II.4.2. Phase-averaged flow structure*

The most prominent feature of noncircular jets is that the variation of their radial spreading in the streamwise direction is azimuthally nonuniform. In fact, the radial spreading of the jet is larger in azimuthal positions, where the curvature of the jet boundary has a local minimum. (The jet boundary may be defined by contours of time-averaged streamwise velocity in  $y$ - $z$  planes along the jet axis.) These azimuthal variations in jet spreading can be accompanied by significant variations in radial entrainment of ambient fluid, as was demonstrated by Ho & Gutmark (1987) in an elliptic jet having an aspect ratio of 2:1. Because the streamwise spreading rate of a noncircular jet is larger where the azimuthal curvature of its boundary is smaller, the  $y$ - $z$  cross section of the jet distorts with downstream distance. In the case of an elliptic jet, the major and minor axes of the jet's cross section are interchanged several times with downstream distance (Ho & Gutmark) because the streamwise spreading rate of the jet is larger in the plane of the minor axis.

Previous investigations of noncircular jets have mostly emphasized time-averaged measurements, and the dynamical evolution of the flow in question has been inferred from flow visualization. In what follows we discuss the phase-averaged flow structure with particular attention to the excitation program  $P_{\pm 2}$ .

In figures II.9(a-d) we show four pairs of  $y$ - $z$  contour plots of the phase-averaged streamwise velocity,  $\langle u(y, z, t) \rangle / U_c$ , and rms velocity fluctuations,  $\langle u'_t(y, z, t) \rangle / U_c$ , for  $P_{\pm 2}$ ; measured at  $x/D_c = 2$  at four equal time intervals during the modulation period. These times are referred to below as  $\tau_1$ ,  $\tau_2$ ,  $\tau_3$ , and  $\tau_4$  ( $\tau = t/T_f$ ) and are chosen so that  $\tau_1$  corresponds to zero crossings of the reference signal,  $e_{ref}(t)$ , where  $de_{ref}(t)/dt > 0$  and  $\tau_i = \tau_1 + (i - 1)/4$  ( $i = 2, 3$ , and  $4$ ). When the flow is forced with  $P_{\pm 2}$ , the contour maps change substantially during the excitation period. At  $\tau = \tau_2$  and  $\tau_4$  (figures II.9b and d, respectively), the jet cross section is essentially rectangular, with an aspect ratio in excess of 2. The major axis of this rectangle is clearly aligned with the  $z$  and  $y$  axes at  $\tau_2$  and  $\tau_4$ , respectively. Thus, the major and minor axes of the cross section of the forced jet are interchanged during each cycle of the modulating wave train. Recall that for  $P_{\pm 2}$  the maxima,  $e_{max}$ , of the modulating waveforms of each pair of opposite actuators occur at the

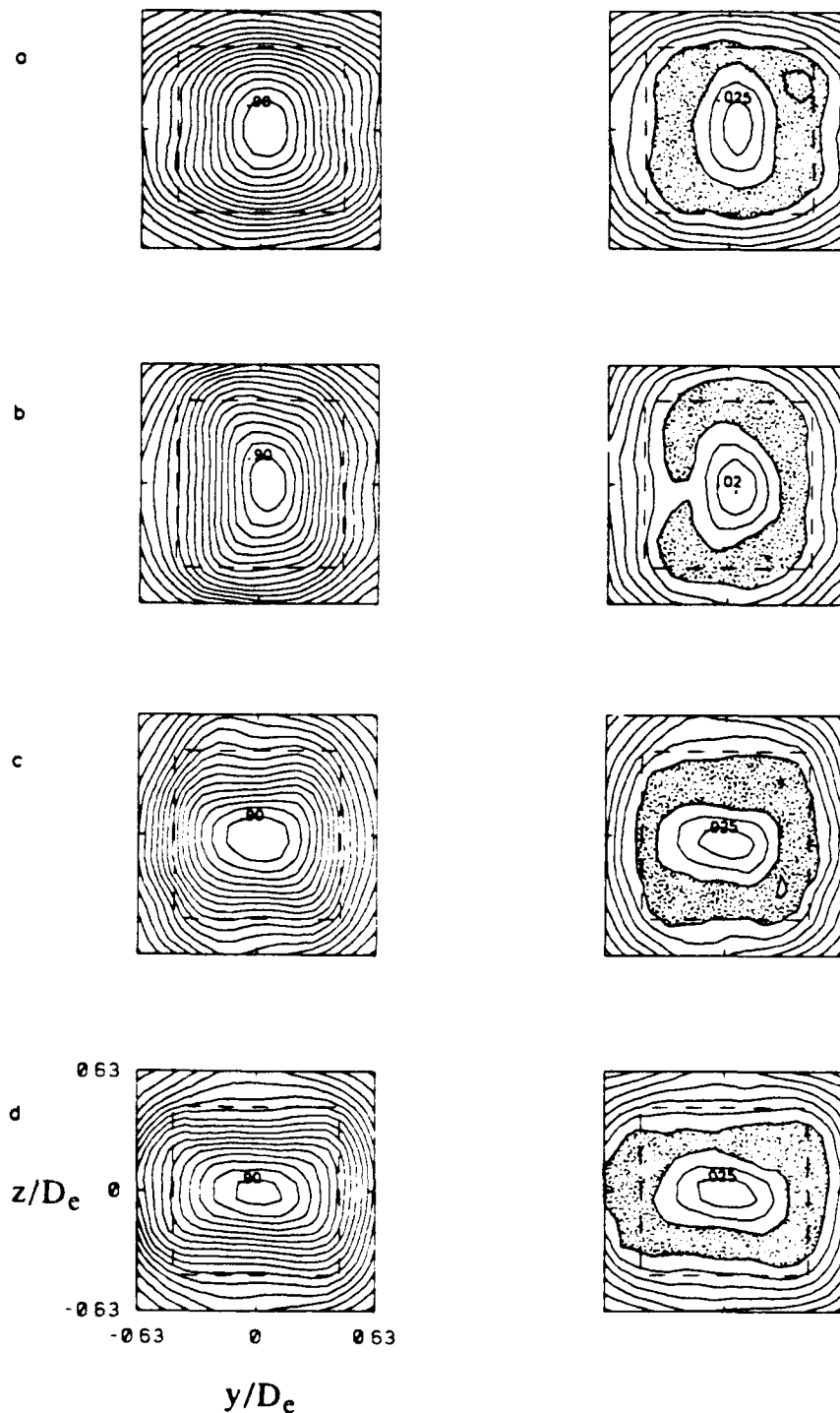


Figure II.9. Contours of  $\langle u(y,z) \rangle / U_e$  [left] and  $\langle u'_t(y,z) \rangle / U_e$  [right] measured at  $x/D_e = 2$ . The jet is forced with  $P$  and the contour maps are plotted at four equal time intervals during the modulating period: (a)  $\tau_1$ ; (b)  $\tau_2$ ; (c)  $\tau_3$ ; (d)  $\tau_4$ . Contour increments for  $\langle u \rangle / U_e$  and  $\langle u'_t \rangle / U_e$  are 0.05 and 0.005, respectively; maximum contour levels,  $c_{\max}$  are labeled. Regions where  $\langle u'_t \rangle / U_e > c_{\max}$  are shaded.

same time as the minima,  $e_{\min}$ , of the modulating waveforms of the other pair. The maximum of the (modulated) excitation input of each pair of opposite actuators is above the threshold at which rollup of the line vortices occurs within the forced azimuthal segments of the jet shear layer. The rollup leads to an increase in the cross-stream spreading of the forced segments and a rectangular distortion of the jet cross section (cf. figure II.9b). Note that  $\tau_2$  corresponds to  $e_m^2 = e_m^4 = e_{\max}$ , while  $\tau_4$  corresponds to  $e_m^1 = e_m^3 = e_{\max}$ .

A noteworthy feature of figures II.9a and c is the variation in aspect ratio of contours of  $\langle u \rangle / U_c$  and  $\langle u' \rangle / U_c$ . For example, at  $\tau = \tau_1$  (figure II.9a), velocity contours with levels  $\langle u \rangle / U_c > 0.5$  are nominally rectangular, with their major axes roughly aligned with the  $z$  axis, while velocity contours with levels  $\langle u \rangle / U_c < 0.5$  are nominally rectangular, with their major axes roughly aligned with the  $y$  axis. The contour  $\langle u \rangle = 0.5$  is approximately square in figures II.9a and c. This indicates that when  $\tau$  first exceeds  $\tau_2$  or  $\tau_4$ , the changes in aspect ratio of the velocity contours begin near the centerline of the jet and then propagate towards its outer edges so that when  $\tau = \tau_2 + 1/2$  or  $\tau_4 + 1/2$ , the axis switching is completed. The axis switching of the jet for  $P_{\pm 2}$  is also shown in an isometric plot of the surface  $\langle u \rangle / U_c = 0.625$  in the  $y$ - $z$ - $t$  coordinates at  $x/D_c = 2$  during three periods of the modulation waveform (figure II.10). (The  $\tau$  coordinate begins at  $\tau = \tau_1$ , and  $\tau_1$ ,  $\tau_2$ ,  $\tau_3$ , and  $\tau_4$  are marked for reference.) As will be shown below, these changes in aspect ratio are apparently connected with the advection of distorted elliptic vortical structures past the measurement station.

Phase-averaged concentrations of rms velocity fluctuations are used to capture the three-dimensional features of vortical structures in the square jet. The utility of this scheme was demonstrated in a transitional plane shear layer by Nygaard & Glezer (1991), who computed  $u'_1(\mathbf{x}, t)$  relative to time series of the instantaneous streamwise velocity. Although concentrations of  $\langle u'_1(\mathbf{x}, t) \rangle$  are not the same as vorticity concentrations, they appear to effectively capture three-dimensional features of streamwise vortices in the (spanwise-forced) plane shear layer.

In figures II.11a and b, we show the surfaces  $\langle u' \rangle / U_c = 0.037$  in the  $y$ - $z$ - $t$  coordinates at  $x/D_c = 2$  for  $P_0$  and  $P_{\pm 2}$ , respectively, during three periods of the modulating waveform (cf. figure II.10). When the flow is excited with  $P_0$  (figure II.11a), the vortical structures appear to be an organized train of square vortex rings that are advected past the measurement station at the modulating frequency. When the flow is excited with  $P_{\pm 2}$  (figure II.11b), the phase-averaged vortical structures are considerably more complex and resemble a train of distorted elliptic vortex rings, as illustrated in figure II.11c. We note that the passage frequency of these vortices is *twice* the modulating

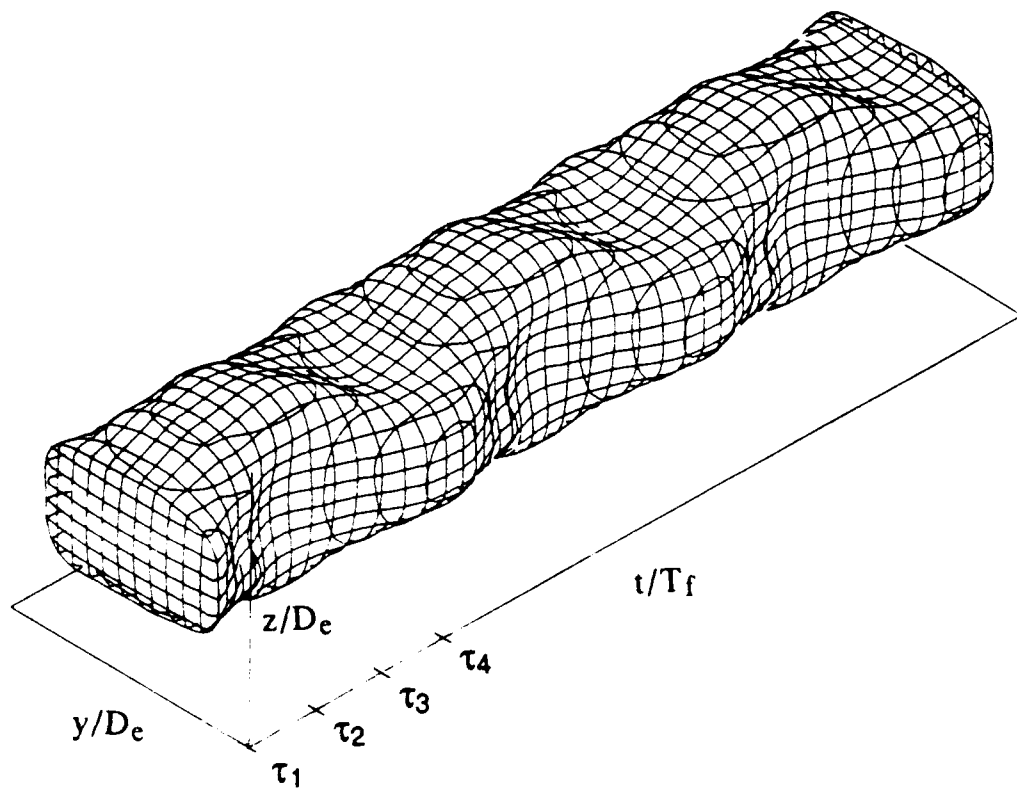


Figure II.10. The surface  $\langle u(y,z,t) \rangle / U_e = 0.625$  at  $x/D_e = 2$  during three periods of the modulating waveform of  $P_{\pm 2}$  [the  $\tau$  coordinate begins at  $\tau = \tau_1$ , and  $\tau_1$ ,  $\tau_2$ ,  $\tau_3$  and  $\tau_4$  are marked for reference].

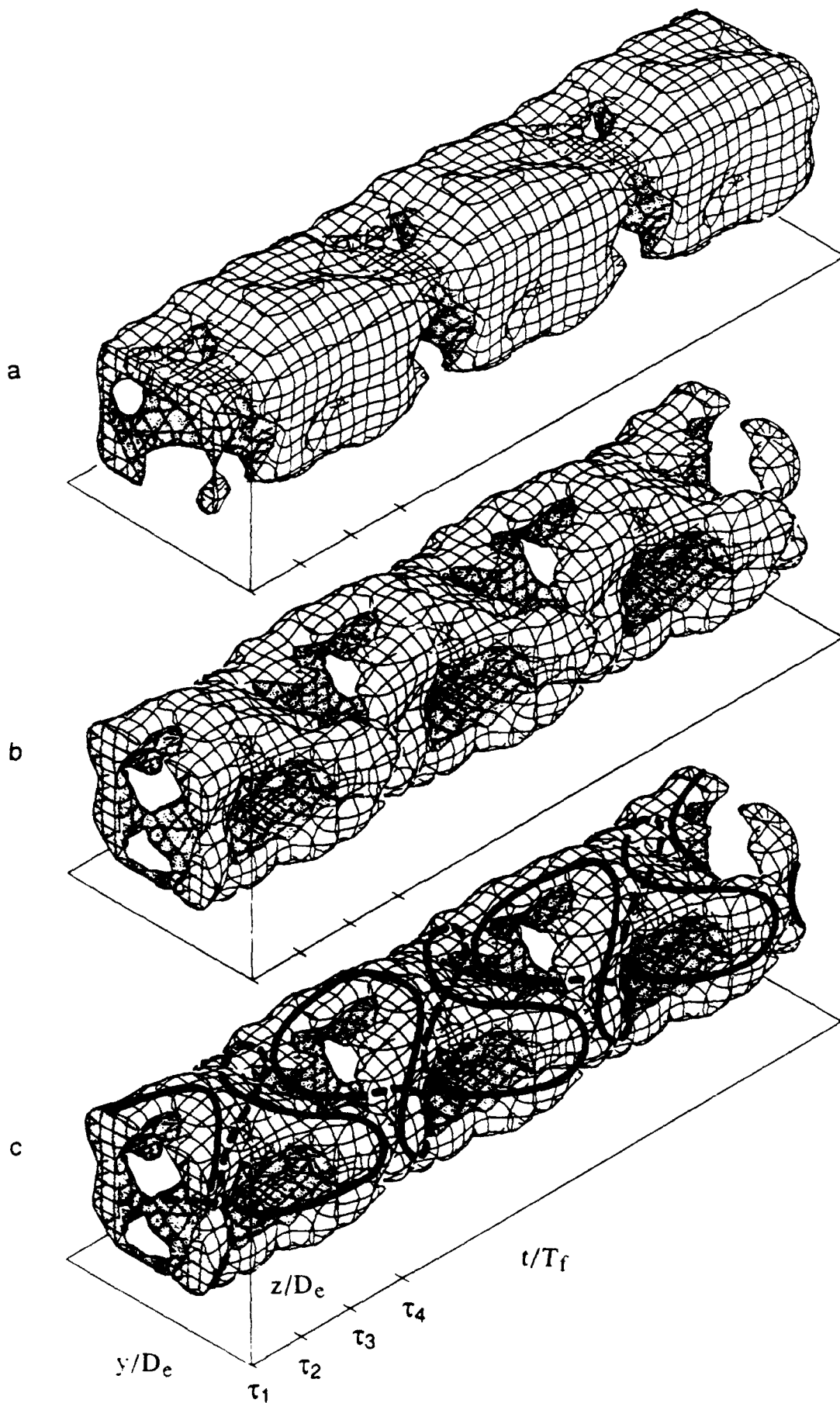


Figure II.11. The surfaces  $\langle u'_t(y,z,t) \rangle / U_c = 0.037$  at  $x/D_e = 2$  during three periods of the modulating waveforms of programs  $P_0$  (a) and  $P_{+2}$  (b). A train of distorted elliptic vortex rings corresponding to (b) is illustrated in (c).



frequency, and that each pair of adjacent vortices are symmetrically distorted in time about the  $y$ - $z$  planes at  $\tau_2 + n/2$  (or  $\tau_4 + n/2$ ), where  $n$  is an integer.

In connection with the appearance of a train of distorted elliptic vortex rings in the forced square jet, we note that isolated noncircular vortex rings undergo self-induced and roughly time-periodic core deformations as they are advected away from the vortex generators (e.g., Kambe & Takao 1971). In particular, elliptic vortex rings undergo core deformations that lead to time-periodic "switching" of their major and minor axes (Dhanak & Bernardinis 1981). Moreover, the dynamics of elliptic vortical structures has been connected with the streamwise evolution and spatial axes switching of elliptic jets (Ho & Gutmark 1987, Hussain & Husain 1989). The flow visualization photographs of Ho and Gutmark show that near the nozzle of an elliptic jet (aspect ratio 2:1) and upstream of the first axis switching, consecutive elliptic vortices are similarly distorted as they are advected downstream. In photographs taken in planes of the major and minor axis of the elliptic nozzle, these distortions appear as upstream and downstream bends, respectively, about the jet centerline. As argued by Hussain and Husain, these distortions lead to streamwise stretching and compressing of the mean  $y$ - $z$  cross sections of the jet along the minor and major axes of the nozzle, respectively. Axis switching begins when the minor and major axes of the jet are approximately equal in length.

Hussain & Husain (1989) assert that azimuthal variations in momentum thickness of the shear layer of an elliptic jet lead to azimuthally nonuniform rollup of elliptic vortices. The rollup appears to progress azimuthally before the cores of these vortices begin to deform. Hence, we conjecture that when the jet is forced with  $P_{\pm 2}$ , rollup of two opposite segments of the jet shear layer is alternately initiated by a corresponding pair of opposite actuators (1, 3 and 2, 4) every  $T_f$  and begins to progress azimuthally. Figures II.6d and f suggest that the rollup of the two forced and opposite segments of the jet shear layer results in vortices having larger cross sections which scale with the width of the jet. The proximity of these vortices apparently forces some of the jet fluid between them to move away from the centerline and parallel to their axes, thus leading to the formation of an almost elliptic vortex ring, the major axis of which is parallel to the tips of the active actuators. Because the two opposite pairs of actuators are activated alternately, the major axes of consecutive elliptical vortices are alternately aligned with either the  $y$  or  $z$  axes. This is consistent with the vortical structures observed at  $x/D_e = 2$ , as shown in figures II.11b and c.

Finally, the effect of excitation programs  $P_0$ ,  $P_{\pm 1}$ ,  $P_{\pm 2}$ , and  $P_{-1}$  on the jet column (at  $x/D_e = 4$ ) may be inferred from surface plots of  $\langle u(y, z, t) \rangle = 2.5$  m/sec (figures II.12a-d). (The plotting routine does not allow for independent scaling of the three

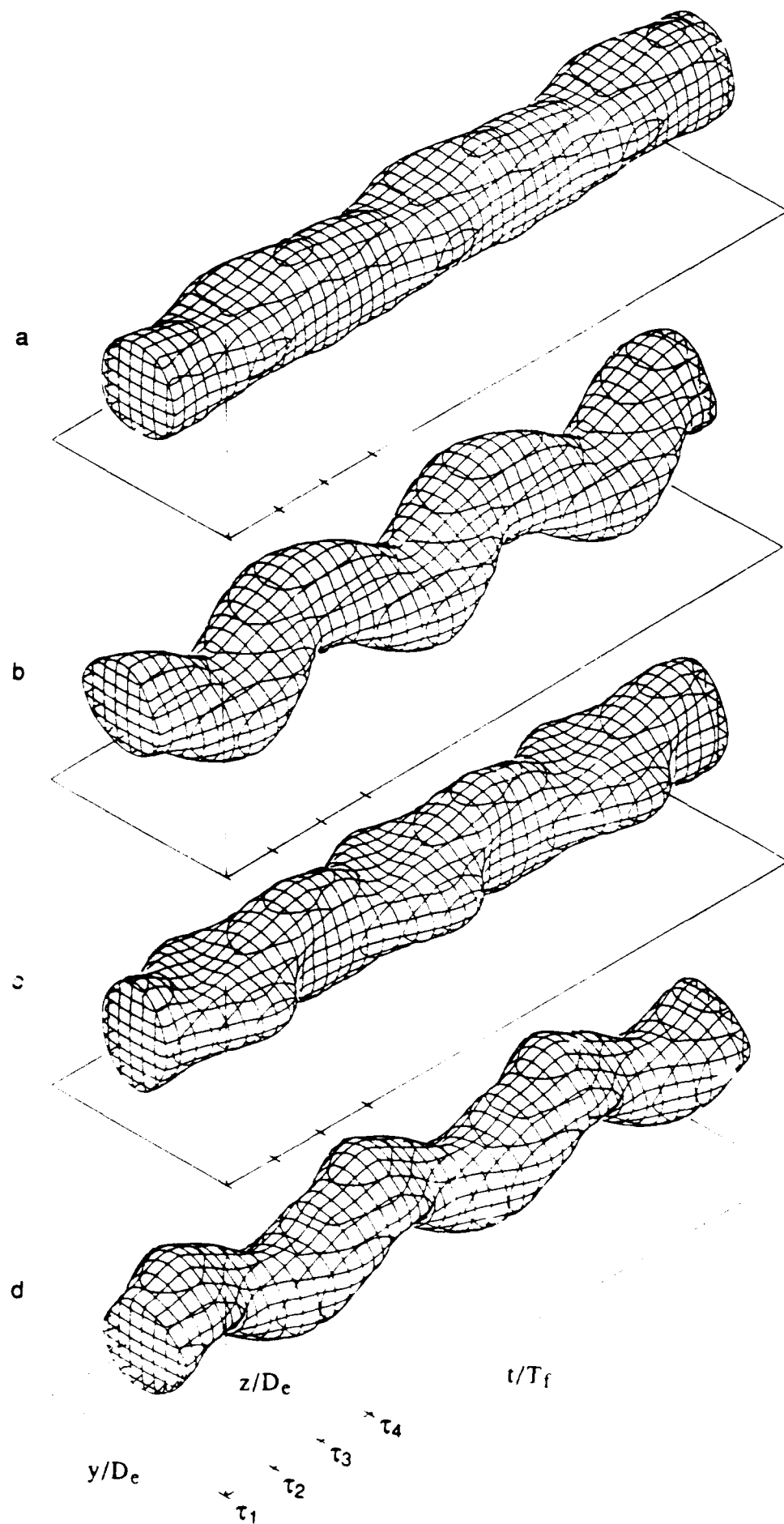


Figure II.12. The surfaces  $\langle u(y,z,t) \rangle / U_e = 0.625$  at  $x/D = 4$ : (a)  $P_0$ ; (b)  $P_{\pm 1}$ ; (c)  $P_{\pm 2}$ ; (d)  $P_{-1}$ .

coordinates, hence the scaling in the  $y$ - $z$  plane of figure II.12 is different from the scaling in figures II.10 and II.11.) As discussed in connection with figure II.7c, figure II.12a shows that forcing with  $P_0$  results in a jet cross section that is virtually circular during most of the excitation period. When the jet is forced with  $P_0$  (figure II.12b), its center (as may be determined by the maximum streamwise velocity) oscillates harmonically (at the excitation frequency) along the line of symmetry of the forcing, which is also a corner bisector of the square conduit. The amplitude of oscillation is  $0.16D_c$  relative to the nozzle centerline. As in figure II.10, when the jet is forced with  $P_{\pm 2}$  (figure II.12c), its cross section becomes elliptical, with an aspect ratio that varies time harmonically between 0.5 and 2. When the jet is forced with  $P_{-1}$  (figure II.12d), its cross section is almost circular and its center spins helically with time. The direction of the spin corresponds to instability mode -1 of a round jet.

## II.5. Summary and outline of future research

The utility of piezoelectric actuators for the modification of free shear flows has been demonstrated in a square air jet. Velocity perturbations are introduced into the jet shear layer by the motion of the free ends of planar cantilevered actuators driven at their resonance frequency. At low excitation levels, the flow is typically not receptive to excitation at the resonance frequency and its higher harmonics, and the induced velocity perturbations are rapidly attenuated. Although the amplitude of the actuator displacement is less than a millimeter, the magnitude of the induced velocity perturbation is proportional to the product of the actuator displacement and its frequency. Hence, if the resonance frequency is high enough, the induced velocity perturbation can be quite large and lead to the rollup of line vortices with axes parallel to the actuator tip within forced azimuthal segments of the jet shear layer. These vortices are formed at the resonance frequency of the actuator, and their cross-sectional dimension scales with the actuator's displacement.

Farther downstream from the actuators, the line vortices coalesce and rapidly lose their identity, rendering velocity spectra of the forced flow virtually featureless. Nevertheless, the formation of these vortices is accompanied by a substantial increase in the cross-stream spreading of the forced segments of the jet shear layer. Hence, excitation at the resonance frequency with azimuthally nonuniform amplitude distribution can result in a substantially distorted mean flow having a featureless velocity spectrum. This capability suggests that proper selection of input waveforms can be used to tailor the mean velocity profile so as to provide favorable conditions for the introduction and propagation of desirable low-frequency disturbances.

Because the line vortices appear only when the induced velocity perturbations exceed a given threshold, amplitude modulation of the excitation waveform results in their rapid coalescence into larger vortical lumps at the modulating frequency. This means that by resonantly driving the actuators with a time-harmonic carrier wave train that is amplitude modulated with the desired excitation input, the excitation waveform can be effectively demodulated by the flow. As a result, the flow is primarily affected by the modulating wave train, while velocity perturbations at the resonance frequency and its higher harmonics are attenuated. Thus, the excitation waveform is tailored to the flow, providing a much more flexible approach than matching the resonance frequency of the actuators to the receptivity of the flow.

The substantial increase in the spreading of forced azimuthal segments of the jet shear layer in the absence of low-frequency modulation suggests itself as a mechanism by which various azimuthal instability modes of the jet column can be effectively excited. This attribute may be particularly useful when the shear layer of the unforced jet is extremely thin, as is the case for high-speed jets where, for a given Strouhal number, there can be a substantial mismatch between unstable frequencies of the jet column and of the jet shear layer.

**The following activities will be undertaken in the last year of the present grant:**

- A high aspect ratio rectangular air jet will be forced using piezoelectric actuators with particular emphasis on jet vectoring.
- Streamwise and cross-stream velocity distributions will be measured simultaneously using x-wire anemometry. The spanwise vorticity field will be reconstructed phase locked to the modulating waveforms.
- The flow will be visualized using a double-pass Schlieren system, and photographed using a high-speed video camera.

## References

- Berger, E. 1967 Suppression of vortex shedding and turbulence behind oscillating cylinders. *Phys. Fluids Suppl.*, S191-S193.
- Betzig, R. E. 1981 Experiments on the linear and non-linear evolution of the double helical instability in jets. AIAA Paper 81-0415. *AIAA 19th Aerospace Sciences Meeting, January 12-15, St. Louis, Missouri.*
- Buch, K.A. & Dahm, W.J.A. 1991 Fine scale structure of conserved scalar mixing in turbulent shear flows:  $Sc \gg 1$ ,  $Sc \approx 1$  and implications for reacting flows. *Report No. 026779-5, The University of Michigan.*
- Champagne, F. H., Pao, Y. H. & Wygnanski, I. J. 1976 On the two-dimensional mixing region. *J. Fluid Mech.* **74**, 209-250.
- Crow, S. C. & Champagne, F. H. 1971 Orderly structure in jet turbulence. *J. Fluid Mech.* **48**, 547-591.
- Dahm, W.J.A., Southerland, K.B., & Buch, K.A. 1991 Direct, high resolution, four-dimensional measurements of the fine scale structure of  $Sc \gg 1$  molecular mixing in turbulent flows. *Phys. Fluids A* **3** (5), 1115-1127.
- Dhanak, M. R. & Bernardinis, B. 1981 The evolution of an elliptic vortex ring. *J. Fluid Mech.* **109**, 189-216.
- Dimotakis, P.E. 1986 Two-Dimensional Shear-Layer Entrainment. *AIAA J.* **24**, 1791-1796.
- Dimotakis, P.E. 1989 Turbulent Free Shear Layer Mixing. AIAA Paper 89-0262. *AIAA 27th Aerospace Sciences Meeting, January 9-12, 1989, Reno, Nevada.*
- DuPlessis, M. P., Wang, R. L. & Kahawita, R. 1974 Investigation of the near-region of a square jet. *J. Fluids Eng.* **96**, 246-251.
- Gessner, F. B., Po, J. K. & Emery, A. F. 1977 Measurements of developing turbulent flow in a square duct. In *Proceedings of Symposium on Turbulent Shear Flows, Pennsylvania State Univ., April 18-20, 1977*, pp. 119-136. Pennsylvania State Univ.
- Glezer, A., Katz, Y. & Wygnanski, I. 1989 On the breakdown of the wave packet trailing a turbulent spot in a laminar boundary layer. *J. Fluid Mech.* **198**, 1-26.
- Gutmark, E., Schadow, K. C., Parr, D. M., Harris, C. K. & Wilson, K. J. 1985 The mean and turbulent structure of noncircular jets. AIAA Paper 85-0543. *Flow Control Conference, March 12-14, Boulder, Colorado.*
- Gutmark, E., Parr, T. P., Hanson-Parr, D. M. & Schadow, K. C. 1989a Azimuthal structure of an annular diffusion flame. *Combustion and Flame* **75**, 229-240.

- Gutmark, E., Schadow, K. C., Parr, T. P., Hanson-Parr, D. M. & Wilson, K. J. 1989b Noncircular jets in combustion systems. *Exp. in Fluids* **7**, 248-258.
- Ho, C.-M. & Gutmark, E. 1987 Vortex induction and mass entrainment in a small-aspect-ratio elliptic jet. *J. Fluid Mech.* **179**, 383-405.
- Ho, C.-M. & Huerre, P. 1984 Perturbed free shear layers. *Ann. Rev. Fluid Mech.* **16**, 365-424.
- Hussain, F. & Husain, H. S. 1989 Characteristics of unexcited and excited jets. *J. Fluid Mech.* **208**, 257-320.
- Kambe, T. & Takao, T. 1971 Motion of distorted vortex rings. *J. Phys. Soc. Japan* **31**, 591-599.
- Koochesfahani, M.M., Catherasoo, C.J., Dimotakis, P.E., Gharib, M., & Lang, D.B. 1979 Two-Point LDV Measurements in a Plane Mixing Layer. *AIAA J.* **17**, 1347-1351.
- Koochesfahani, M.M. & Dimotakis, P.E. 1986 Mixing and chemical reactions in a turbulent liquid mixing layer. *J. Fluid Mech.* **170**, 83-112.
- Koochesfahani, M.M. & MacKinnon, C.G. 1991 Influence of forcing on the composition of mixed fluid in a two-stream shear layer. *Phys. Fluids A* **3** (5), 1135-1142.
- Lee, M. & Reynolds, W. C. 1985 Bifurcating and blooming jets. *Report TF-22*. Stanford University.
- Liepmann, H. W. & Nosenchuck, D. M. 1982 Active control of laminar-turbulent transition. *J. Fluid Mech.* **118**, 201-204.
- Liepmann, H. W., Brown, G. L. & Nosenchuck, D. M. 1982 Control of laminar instability waves using a new technique. *J. Fluid Mech.* **118**, 187-200.
- Long, T. A. & Petersen, R. A. 1991 Controlled interactions in a forced axisymmetric jet: part 1: the distortion of the mean flow. *J. Fluid Mech.* (in press).
- Melling, A. & Whitelaw, J. H. 1976 Turbulent flow in a rectangular duct. *J. Fluid Mech.* **78**, 289-315.
- Nygaard, K. J. & Glezer, A. 1991 Evolution of streamwise vortices and generation of small-scale motion in a plane shear layer. *J. Fluid Mech.* **231**, 257-301.
- Nosenchuck, D.M. 1982 Passive and Active Control of Boundary Layer Transition. *Ph.D. Thesis, California Institute of Technology*.
- Oster, D. & Wygnanski, I. 1982 The forced mixing layer between parallel streams. *J. Fluid Mech.* **123**, 91-130.
- Oster, D., Wygnanski, I. & Fiedler, H. 1977 Some preliminary observations on the effect of initial conditions on the structure of the two-dimensional turbulent mixing layer. In *Turbulence in Internal Flows* (ed. S. N. B. Murthy), pp. 67-87. Hemisphere.

- Petersen, R. A., Samet, M. M. & Long, T. A. 1988 Excitation of azimuthal modes in an axisymmetric jet. *IUTAM Symposium on Turbulence Management and Relaminarization, Bangalore, India* (eds. H. W. Liepmann and R. Narasima), pp. 435-443. Springer Verlag.
- Quinn, W. R. & Militzer, J. 1988 Experimental and numerical study of a turbulent free square jet. *Phys. Fluids* **31**, 1017-1025.
- Reisenthel, P. 1988 Hybrid instability in an axisymmetric jet with enhanced feedback. Ph.D. dissertation, Illinois Institute of Technology, Chicago.
- Roberts, F.A. 1985 Effects of a Periodic Disturbance on Structure and Mixing in Turbulent Shear Layers and Wakes. *Ph.D. Thesis, California Institute of Technology*.
- Roberts, F. A. & Roshko, A. 1985 Effects of periodic forcing on mixing in turbulent shear layers and wakes. *AIAA Shear Flow Control Conference, March 12-14, Boulder, Colorado*.
- Roshko, A. 1981 The plane mixing layer: flow visualization results and three-dimensional effects. In *The Role of Coherent Structures in Modelling Turbulence and Mixing* (ed. J. Jimenez). Lecture Notes in Physics, vol. 136, pp.208-217. Springer.
- Schubauer, G. B. and Skramstad, H. K. 1947 Laminar boundary layer oscillations and stability of laminar flow. *J. Aero. Sci.* **14**, 68-78.
- Sforza, P. M., Steiger, M. H. & Trentacoste, N. 1966 Studies on three-dimensional viscous jets. *AIAA J.* **4**, 800-806.
- Strange, P. J. R. & Crighton, D. G. 1983 Spinning modes in axisymmetric jets: part 1. *J. Fluid Mech.* **134**, 231-245.
- Tennekes, H. & Lumley, J.L. 1972 **A First Course in Turbulence**. The MIT Press.
- Trentacoste, N. & Sforza, P. M. 1967 Further experimental results for three-dimensional free jets. *AIAA J.* **5**, 885-891.
- Tsuchiya, Y., Horikoshi, C. & Sato, T. 1986 On the spread of rectangular jets. *Exp. in Fluids* **4**, 197-204.
- Wehrmann, O. H. 1965 Reduction of velocity fluctuations in a Karman vortex street by a vibrating cylinder. *Phys. Fluids* **8**, 760-761.
- Wehrmann, O. H. 1967a The influence of vibrations on the flow field behind a cylinder. *Document D1-82-0619*. Boeing Scientific Research Laboratories.
- Wehrmann, O. H. 1967b Self-adjusting feedback loop for mechanical systems to influence flow in transition: part I. *Document D1-82-0632*. Boeing Scientific Research Laboratories